

PHOTOCATALYTIC WATER SPLITTING

by

YENTING KUO

B.A., National Central University, Taiwan, 2000

M.S., National Central University, Taiwan, 2002

AN ABSTRACT OF A DISSERTATION

submitted in partial fulfillment of the requirements for the degree

DOCTOR OF PHILOSOPHY

Department of Chemistry
College of Arts and Science

KANSAS STATE UNIVERSITY
Manhattan, Kansas

2011

Abstract

New photocatalytic materials Ti-In oxy(nitride) and nanosized Ru-loaded strontium titanate doped with Rh (Ru/SrTiO₃:Rh) have been synthesized. The textural and surface characteristic properties were studied by nitrogen BET analysis, diffuse reflectance UV-vis spectroscopy, X-ray photoelectron spectroscopy, transmission electron microscopy, scanning electron microscopy and powder XRD. The photocatalytic properties were enhanced by the binary metal oxides of titanium dioxide and indium oxide. The XRD patterns confirmed the oxygen exchange between two metal oxides during the synthesis. Moreover, the presence of titanium dioxide can help the stabilization of InN during hot NH_{3(g)} treatment. On the other hand, the particle sizes of aerogel prepared Ru/SrTiO₃:Rh varied from 12 to 25 nm depended on different Rh doping. A mixture of ethanol and toluene was found to be the best binary solvent for supercritical drying, which yielded a SrTiO₃ sample with a surface area of 130 m²/g and an average crystallite size of 6 nm.

Enhanced photocatalytic hydrogen production under UV-vis light irradiation was achieved by ammonolysis of intimately mixed titanium dioxide and indium oxide at high temperatures. Gas chromatography monitored steadily the formation of hydrogen when sacrificial (methanol or ethanol) were present. XRD patterns confirmed that the photocatalysts maintain crystalline integrity before and after water splitting experiments. Moreover, the presence of InN may be crucial for the increase of hydrogen production activities.

These Ru/SrTiO₃:Rh photocatalysts have been studied for photocatalytic hydrogen production under visible light. The band gap of the bulk SrTiO₃ (3.2 eV) does not allow response to visible light. However, after doping with rhodium and loaded with ruthenium, the modified strontium titanates can utilize light above 400 nm due to the formation of valence band or

electron donor levels inside of the band gap. Moreover, the surface areas of these photocatalysts are much larger than conventional solid-state synthesized samples (1-2 m²/g), which yielded more Ru loading and reaction sites. The areogel and hydrothermal synthesized samples required basic (alkaline) conditions for hydrogen generation facilitation compared with acidic conditions for conventional solid-state samples.

PHOTOCATALYTIC WATER SPLITTING

by

YENTING KUO

B.A., National Central University, Taiwan, 2000

M.S., National Central University, Taiwan, 2002

A DISSERTATION

submitted in partial fulfillment of the requirements for the degree

DOCTOR OF PHILOSOPHY

Department of Chemistry
College of Arts and Science

KANSAS STATE UNIVERSITY
Manhattan, Kansas

2011

Approved by:

Major Professor
Kenneth J. Klabunde

Copyright

YENTING KUO

2011

Abstract

New photocatalytic materials Ti-In oxy(nitride) and nanosized Ru-loaded strontium titanate doped with Rh (Ru/SrTiO₃:Rh) have been synthesized. The textural and surface characteristic properties were studied by nitrogen BET analysis, diffuse reflectance UV-vis spectroscopy, X-ray photoelectron spectroscopy, transmission electron microscopy, scanning electron microscopy and powder XRD. The photocatalytic properties were enhanced by the binary metal oxides of titanium dioxide and indium oxide. The XRD patterns confirmed the oxygen exchange between two metal oxides during the synthesis. Moreover, the presence of titanium dioxide can help the stabilization of InN during hot NH_{3(g)} treatment. On the other hand, the particle sizes of aerogel prepared Ru/SrTiO₃:Rh varied from 12 to 25 nm depended on different Rh doping. A mixture of ethanol and toluene was found to be the best binary solvent for supercritical drying, which yielded a SrTiO₃ sample with a surface area of 130 m²/g and an average crystallite size of 6 nm.

Enhanced photocatalytic hydrogen production under UV-vis light irradiation was achieved by ammonolysis of intimately mixed titanium dioxide and indium oxide at high temperatures. Gas chromatography monitored steadily the formation of hydrogen when sacrificial (methanol or ethanol) were present. XRD patterns confirmed that the photocatalysts maintain crystalline integrity before and after water splitting experiments. Moreover, the presence of InN may be crucial for the increase of hydrogen production activities.

These Ru/SrTiO₃:Rh photocatalysts have been studied for photocatalytic hydrogen production under visible light. The band gap of the bulk SrTiO₃ (3.2 eV) does not allow response to visible light. However, after doping with rhodium and loaded with ruthenium, the modified strontium titanates can utilize light above 400 nm due to the formation of valence band or

electron donor levels inside of the band gap. Moreover, the surface areas of these photocatalysts are much larger than conventional solid-state synthesized samples (1-2 m²/g), which yielded more Ru loading and reaction sites. The areogel and hydrothermal synthesized samples required basic (alkaline) conditions for hydrogen generation facilitation compared with acidic conditions for conventional solid-state samples.

Table of Contents

List of Figures	xii
List of Tables	xviii
List of Equations	xix
Acknowledgements	xxi
Dedication	xxii
Preface	xxiii
Chapter 1 - Introduction	1
References	5
Chapter 2 - Basis of photocatalytic water splitting	6
References	11
Chapter 3 - Titanium-Indium Oxynitrides for Water Splitting. Photocatalysis vs. Light Induced Catalyst Oxidation by Water	13
3.1 Introduction	13
3.2 Experimental	14
3.2.1 Preparation of Ti-In nitride composites	14
3.2.2 Hydrogen Production	15
3.2.3 Characterization of Composites	16
3.3 Results and Discussion	16
3.3.1 Crystal Structure	16
3.3.2 Elemental composition of the TiInO_xY_z composites	23

3.3.3 UV-Vis Diffuse Reflectance spectra.....	25
3.3.4 X-ray Photoelectron Spectroscopy	27
3.3.5 Scanning Electron Microscopy	32
Brunauer, Emmett, Teller (BET) surface area	33
3.4 Conclusions.....	36
References.....	38
Chapter 4 - Hydrogen from ethanol solution under UV-visible light. Photocatalysts produced by Nitriding Titanium nitride and Indium oxide Intimate mixtures to Form Ti-In nitride composites	
4.1 Introduction.....	41
4.2 Experimental Section	42
4.2.1 Preparation of TiN/InN composites	42
4.2.2 Characterization of Catalysts	43
4.2.3 Photocatalytic Reactions	43
4.3 Results and Discussion	44
4.3.1 Dependence of Photocatalytic Activity on Ammonolysis time	44
4.3.2 Crystal Structure	48
4.3.3 UV-Visible Diffuse Reflectance Spectra	52
4.3.4 SEM Observations	54
4.3.5 X-ray Photoelectron Spectra	55
4.4 Conclusions.....	58
References.....	60
Chapter 5 - Synthesis and characterization of strontium titanate	63

5.1 Literature review on strontium titanate.....	63
5.2 Nanomaterials	66
5.3 Synthesis of titanates	67
5.3.1 Introduction.....	67
5.3.2 Solid-state synthesis.....	68
5.3.3 Gas phase synthesis.....	69
5.3.4 Aerosol technique	72
5.3.5 Sol-gel technique	74
5.3.6 Aerogel technique	76
5.4 Temperature treatment.....	77
5.4.1 Heat treatment.....	79
5.5 Modification of titanates by doping.....	82
References.....	87
 Chapter 6 - Water Splitting under Visible Light using Aerogel Prepared Strontium Titanate	
(SrTiO ₃) Nanomaterials Doped with Ruthenium and Rhodium Metals	91
6.1 Introduction.....	92
6.2 Materials and methods	93
6.3 Results and discussion	96
6.3.1 Strontium titanate calcination at different temperatures	96
6.3.2 H ₂ generation of strontium titanate at different pHs.....	99
6.3.3 Dependence of H ₂ evolution activity of aerogel Ru/SrTiO ₃ :Rh on different calcination temperatures	100

6.3.4 Dependence of H ₂ evolution activity of aerogel Ru/SrTiO ₃ :Rh on different Rh doping amounts	103
6.3.5 Dependence of H ₂ evolution activity of aerogel Ru/SrTiO ₃ :Rh upon the different co-catalyst Ru amounts	105
6.3.6 Mechanism	108
6.4 Conclusions	111
References	113

List of Figures

Figure 1.1 Conversion of solar energy to hydrogen energy by using powdered photocatalysts. ...	2
Figure 1.2 Comparison between photosynthesis of green plants and photocatalytic water splitting reaction. ⁵	4
Figure 1.3 Water splitting by electrochemical photolysis using TiO ₂ as photoelectrode. ⁹	4
Figure 2.1 Main processes in photocatalytic water splitting.....	7
Figure 2.2 Principle of water splitting using semiconductor photocatalysts.	8
Figure 2.3 Relationship between band structure of semiconductor and redox potentials of water splitting. ¹³	9
Figure 2.4 Mechanism of overall water splitting using the Z-scheme photocatalysis system driven by electron transfer photocatalysts.	9
3.1 Experimental setup for nitridation of TiO ₂ /In ₂ O ₃ mixture.....	14
3.2 Experimental setup for hydrogen production measurement.	15
3.3 Powder XRD patterns obtained by nitriding a mixture of TiO ₂ and In ₂ O ₃ at different ammonolysis temperatures (c) 700 °C (d) 750 °C (e) 800 °C (f) 850 °C for 20 hours under a 250 mL/ min flow rate of NH ₃ . (a) TiO ₂ anatase (b) In ₂ O ₃ (g) TiN.	19
3.4 Dependence of UV-vis hydrogen production activity of nitrided mixture of TiO ₂ and In ₂ O ₃ at different ammonolysis temperatures (a) 700 °C (b) 750 °C (c) 800 °C (d) 850 °C for 20 hours under a 250 mL/ min flow rate of NH ₃ . Catalyst (0.3g), an aqueous slurry mixed with 0.13 g sulfuric acid (pH : ~2.6); light source, high-pressure mercury lamp (450 W); inner irradiation-type reaction vessel; reaction temperature was controlled between 20 to 25 °C.	20

3.5 Long term dependence of visible light hydrogen production activity of nitrated mixture of TiO₂ and In₂O₃ (750 °C ammonolysis temperatures for 18 hours under a 250 mL/ min flow rate of NH₃). Catalyst (0.3g), an aqueous solution mixed with 0.13 g sulfuric acid (pH : ~2.6); light source, high-pressure mercury lamp (450 W) with 2M NaNO₂ solution as light filter. Inner irradiation-type reaction vessel. Reaction temperature was controlled between 20 to 25 °C. 21

3.6 Dependence of UV-vis light hydrogen production activity of a nitrated mixture of TiO₂ and In₂O₃ at 700 °C ammonolysis temperatures for 20 hours under a 250 mL/ min flow rate of NH₃. Catalyst (0.3g), an 20 % ethanol aqueous solution; light source, high-pressure mercury lamp (450 W). Inner irradiation-type reaction vessel. Reaction temperature was controlled between 20 to 25 °C. 22

3.7 Long term dependence of visible light hydrogen production activity of nitrated mixture of TiO₂ and In₂O₃ (700 °C ammonolysis temperatures for 20 hours under a 250 mL/ min flow rate of NH₃). Catalyst (0.4 g), an 10 % methanol aqueous solution; light source, high-pressure mercury lamp (450 W) with 2M NaNO₂ solution as light filter. Inner irradiation-type reaction vessel. Reaction temperature was controlled between 20 to 25 °C. 23

3.8 Powder XRD patterns of (a) before (b) after hydrogen production from water under UV-vis light obtained by nitrating a mixture of TiO₂ and In₂O₃ at 850 °C for 20 hours under a 250 mL/min flow rate of NH₃. 25

3.9 UV-Vis diffuse reflectance spectra of samples obtained by nitrating a mixture of TiO₂ and In₂O₃ at different ammonolysis temperatures (a) 700 °C (b) 750 °C (c) 800 °C (d) 850 °C for 20 hours under a 250 mL/ min flow rate of NH₃. (e) Titanium dioxide (f) Indium oxide. 27

3.10 XPS spectra of samples obtained by nitriding a mixture of TiO ₂ and In ₂ O ₃ at different ammonolysis temperatures (a) 850 °C (b) 800 °C (c) 750 °C (d) 700 °C for 20 hours under a 250 mL/ min flow rate of NH ₃	30
3.11 XPS spectra of (a) before (b) after hydrogen production from water reaction under UV-vis light for a nitrated mixture of TiO ₂ and In ₂ O ₃ at different ammonolysis temperatures (A) 850 °C (B) 800 °C (C) 750 °C (D) 700 °C for 20 hours under a 250 mL/ min flow rate of NH ₃	31
3.12 SEM images of synthesis Ti : In= 2 : 1, 800 °C ammonolysis 15 hours (a) before UV-vis irradiation at 15K magnification (b) after UV-vis irradiation at 15K magnification.....	33
3.13 Five types of adsorption isotherms. ²²	35
4.1 Dependence of photocatalytic activity of mixture of TiN (13 h)/In ₂ O ₃ at different ammonolysis time for (a) 1 (b) 3 (c) 5 h at 750 °C under a 250 mL/ min flow rate of NH ₃ . Catalyst (0.3g), a 20 % ethanol aqueous solution, high-pressure mercury lamp (450 W); inner irradiation-type reaction vessel.....	45
4.2 Dependence of photocatalytic activity of mixture of TiN (13 h)/In ₂ O ₃ further ammonolysis for 3 h at 750 °C under a 250 mL/ min flow rate of NH ₃ . Catalyst (0.3g), a 20 % ethanol aqueous solution, high-pressure mercury lamp (450 W); inner irradiation-type reaction vessel.....	46
4.3 Dependence of photocatalytic activity of TiO ₂ nitridation 18 h under a 250 mL/ min flow rate of NH ₃ . Catalyst (0.3g), a 20 % ethanol aqueous solution, high-pressure mercury lamp (450 W); inner irradiation-type reaction vessel.	47

4.4 Dependence of photocatalytic activity of nitridation TiN (18 h)/In ₂ O ₃ 3 h at 750 °C under a 250 mL/ min flow rate of NH ₃ . Catalyst (0.3g), a 20 % ethanol aqueous solution, high-pressure mercury lamp (450 W); inner irradiation-type reaction vessel.....	47
4.5 Powder XRD patterns of (a) TiN (13 h)/In ₂ O ₃ mixture and different nitridation time of TiN (13 h)/In ₂ O ₃ for (b) 1 (c) 3 (d) 5 h at 750 °C under a 250 mL/min flow rate of NH ₃	49
4.6 Schematic representation showing the particle size, different crystal sizes of compounds and the ratio of compounds for the composite. Distribution number and crystal sizes are based on the XRD data (figure 4.5).	50
4.7 Powder XRD patterns of (a) TiN (18 h)-In nitride ammonolysis 3 h (b) TiN (13 h)-In nitride ammonolysis 3 h (c) TiN (13 h)/In ₂ O ₃ mixture (d) TiN (18 h)/In ₂ O ₃ mixture.....	51
4.8 Powder XRD patterns of TiN (13 h)/In ₂ O ₃ mixture nitridation 1 h at 750 °C under a 250 mL/min flow rate of NH ₃ (a) before (b) after water splitting reaction.	52
4.9 Diffuse reflectance spectra of (a) In ₂ O ₃ (b) TiN (13 h) (c) TiN (13 h)/In ₂ O ₃ mixture and different nitridation time of TiN (13 h)-In nitride for (d) 1 (e) 3 (f) 5 h at 750 °C under a 250 mL/min flow rate of NH ₃ . (g) TiN (18 h)/In ₂ O ₃ mixture (h) TiN (18 h)-In nitride for 3 h.	53
4.10 SEM images of (a) TiN (13 h)/In ₂ O ₃ mixture and different nitridation time of TiN (13 h)-In nitride for (b) 1 (c) 3 (d) 5 h at 750 °C under a 250 mL/min flow rate of NH ₃ . (e) TiN (18 h)/In ₂ O ₃ mixture (f) TiN (18 h)-In nitride ammonolysis 3 h.	55
4.11 XPS spectra of (a) TiN (13 h)/In ₂ O ₃ mixture and different nitridation time of TiN (13 h)/In ₂ O ₃ for (b) 1 (c) 3 (d) 5 h at 750 °C under a 250 mL/min flow rate of NH ₃	58
5.1 Perovskite (ABO ₃) UnitCell.....	63
5.2 Perovskite structure (BO ₆ and A ²⁺ layers).....	65
5.3 Sintering by diffusion (path 1 - surface diffusion, path 2 - volume diffusion).....	78

5.4 Temperature-pressure Diagram for Supercritical Drying, where C – Critical Point, SCF – Super Critical Fluid, Tc – Critical Temperature, Pc – Critical Pressure. ^{26, 37}	81
5.5 UV-Visible Absorption Spectra of a) Pure TiO ₂ and b) –d) Cr Ion-implanted TiO ₂ with Cr of 2.2, 6.6, and 13 x10 ⁻⁷ mol/g. ³⁸	84
5.6 Diffuse reflectance spectra of SrTiO ₃ :M(0.5%). M = (a) Mn, (b) Ru, (c) Rh, (d) Pd, (e) Ir, and (f) Pt. A broken line represents a spectrum of nondoped SrTiO ₃ . ³	85
6.1 Modified aerogel procedure from alkoxides for Ru/SrTiO ₃ :Rh synthesis.	96
6.2 Powder XRD patterns of SrTiO ₃ :Rh calcined in air at different temperatures. (a) as synthesized (b) 300 °C (c) 400 °C (d) 500 °C.	98
6.3 Dependence of H ₂ evolution activity of SrTiO ₃ :Rh (1.5 wt% Ru, 1 mole% Rh, cal. 550 °C) at different pHs under visible light in 10 vol% methanol-water solution.	100
6.4 Dependence of H ₂ evolution activity of SrTiO ₃ :Rh (1.5 wt% Ru, 1 mole% Rh) upon different calcination temperatures under visible light in 10 vol % methanol-water solution.	102
6.5 Diffuse reflectance spectra of Rh-doped aerogel SrTiO ₃ (1.5 wt% Ru, 1.25 mole% Rh) from different calcination temperatures (a) 450 °C (b) 500 °C (c) 550 °C (d) 600 °C (e) 650 °C.	103
6.6 Dependence of H ₂ evolution activity of Rh-doped aerogel SrTiO ₃ (1.5 wt% Ru, cal. 500 °C) at different doping amounts in 10 vol % methanol-water solution (pH = 12.4, adjusted by NaOH) under visible light.	105
6.7 Diffuse reflectance spectra of Rh-doped aerogel SrTiO ₃ (1.5 wt% Ru, cal. 500 °C) from different doping amounts (a) 1 mole% (b) 1.25 mole% (c) 1.5 mole% (d) 1.75 mole%....	106
6.8 TEM images of Rh-doped aerogel synthesis SrTiO ₃ (1.5 wt% Ru, cal. 500 °C) upon the different Rh doping amount (a) 1 mole% (b) 1.25 mole% (c) 1.5 mole% (d) 1.75 mole%.	107

6.9 Dependence of H ₂ evolution activity of aerogel SrTiO ₃ : Rh (1.25 mole % Rh, cal. 500 °C) upon different amounts of co-catalyst Ru in 10 vol % methanol solution (pH = 12.4, adjusted by NaOH) under visible light.	108
6.10 Proposed schematic diagram for visible light response of Ru/SrTiO ₃ :Rh photocatalyst. ..	110
6.11 XPS spectra of Ru/SrTiO ₃ :Rh (1.25 mole % Rh, 1.5 wt% Ru, Cal. 500 °C) (a) C 1s (b) Ru 3p _{3/2} (c) Rh 3d _{5/2}	111

List of Tables

3.1 Elemental analysis before and after hydrogen production reaction of Ti-In (oxy)nitride (800 °C) under UV-vis light.....	24
3.2 The maximum absorbance wavelength, Band Gap Energies and hydrogen production rates in pure water of Ti-In (oxy)nitride samples prepared by different ammonolysis temperatures	26
4.1 BET and Photocatalytic activities of TiN/In ₂ O ₃ with various nitridation times under UV - Visible irradiation in 20 % ethanol solution	46
4.2 Diffraction Data Powder X-Ray	49
4.3 Characterization Data for various samples: UV-vis Absorption Spectra	53
5.1 Wet Chemical methods for the synthesis of mixed metal oxides	66
5.2 CVD based techniques	72
5.3 Oxide Powders Prepared by the Aerosol Method ²¹	73
5.4 Critical Points of Some Solvents ²⁶	81
6.1 Characteristic properties of SrTiO ₃ :Rh (1 mole %) calcined in air at different temperatures.	98

List of Equations

$\text{CH}_4 + \text{H}_2\text{O} \rightarrow \text{CO} + 3\text{H}_2$ (1.1)	1
$\text{CO} + \text{H}_2\text{O} \rightarrow \text{CO}_2 + \text{H}_2$ (1.2)	1
$2d \sin\theta = n\lambda$ (3.1)	17
$D = \frac{K\lambda}{B \cos\theta_B}$ (3.2)	17
$\text{TiIn}_{0.029}\text{N}_{0.63}\text{O}_{1.4} + 0.65\text{H}_2\text{O} \rightarrow 0.65\text{H}_2 + \text{TiO}_2 + 0.015\text{In}_2\text{O}_3 + 0.32\text{N}_2$ (3.3)	24
$\frac{1}{W(\frac{P_0}{P}-1)} = \frac{1}{W_m C} + \frac{C-1}{W_m C} \left(\frac{P}{P_0}\right)$ (3.4)	34
$S_t = \frac{W_m N A C S}{M}$ (3.5)	34
$S = \frac{S_t}{w}$ (3.6)	34
$R_K = \frac{-2\gamma V_m}{RT \ln(\frac{P}{P_0})}$ (3.7)	34
$(1-x) \text{MCO}_3 + x\text{M}'\text{CO}_3 \rightarrow \text{M}_{1-x}\text{M}'_x(\text{CO}_3) \rightarrow \text{M}_{1-x}\text{M}'_x\text{O}$ (5.1)	69
$\text{Si}(\text{OEt})_4 \rightarrow \text{SiO}_2 + 2 \text{C}_2\text{H}_4 + 2 \text{EtOH}$ (5.2)	71
$2 \text{H}_2 + \text{O}_2 \rightarrow 2 \text{H}_2\text{O}$ (5.3)	73
$\text{TiCl}_4 + 2 \text{H}_2\text{O} \rightarrow \text{TiO}_2 + 4 \text{HCl}$ (5.4)	73
$\text{SiCl}_4 + 2 \text{H}_2 + \text{O}_2 \rightarrow \text{SiO}_2 + 4 \text{HCl}$ (5.5)	74
$\equiv\text{M}-\text{OR} + \text{H}_2\text{O} \rightarrow \equiv\text{M}-\text{OH} + \text{HOR}$ (Hydrolysis) (5.6)	75
$\equiv\text{M}-\text{OH} + \equiv\text{M}-\text{OR} \rightarrow \equiv\text{M}-\text{O}-\text{M}\equiv + \text{HOR}$ (Condensation) (5.7)	75
$2 \equiv\text{M}-\text{OH} \rightarrow \equiv\text{M}-\text{O}-\text{M}\equiv + \text{H}_2\text{O}$ (Addition) (5.8)	75
$\text{M}(\text{OR})_n + m \text{H}_2\text{O} \rightarrow \text{M}(\text{OR})_{n-m}(\text{OH})_m + m \text{ROH}$ (5.9)	76

MOH + MOX → MOM + XOH (5.10) 76

Acknowledgements

Numerous people were helping me in the completion of this dissertation. First and foremost, I am appreciative and thankful for the support of my supervisor: Professor Kenneth J. Klabunde. He is the coolest adviser, who taught me how to scientifically approach and solve the problems with resolute mind and diligently unremitting spirit. Modeling from him, I learn the dedication to science and research.

I would like to thank my graduate committee members for taking time and efforts to have active roles in my graduate studies at Kansas State University, Dr. Kenneth J. Klabunde, Dr. Ryszard Jankowiak, Dr. Eric A. Maatta and Dr. Christopher M. Sorensen. I would like to thank them for their help for useful and valuable suggestions and discussions.

I would also like to express my thanks and gratitude to several professors, who kindly provided me their help: Professor Chun-Guey Wu built me the foundation of the chemistry. Professor Eric A. Maatta generously helped me for the reference letters and encouragement. Professor Christine Aikens generously helped me for the cover letters and presentation preparation.

Besides the faculties, I would like to thank the staff of department of chemistry, especially Jim Hodgson and Tobe Eggers, for their expertise support to all the experiments.

Last, but certainly not least, I would like to thank my family and friends for always supporting me. You do not know how much your support means to me and without you standing by me I would never have written this dissertation.

Dedication

The dissertation is dedicated to my parents and wife, Yufen. I give my deepest expression of love and appreciation for their support and encouragement, and their sacrificed devotion to help me to conquer my graduate program.

Preface

It is essential that the student acquires an understanding of and a lively feeling for values. He must acquire a vivid sense of the beautiful and of the morally good. Otherwise he with his specialized knowledge more closely resembles a well-trained dog than a harmoniously developed person.

By Albert Einstein

Chapter 1 - Introduction

The increase of energy requirement and decrease of fossil fuel result in the urgent development of renewable energy. Because of high fabrication costs, insufficient light absorption¹ and inefficient charge transfer,² photovoltaic² and electrochemical solar cells²⁻⁴ are still not economical. On the other hand, hydrogen is a clean energy when it is used in fuel cells and only produces water. Moreover, ammonia synthesis in the industrial world also needs a large scale source of H₂. However, the largest hydrogen source in the present day is mainly from fossil fuels as well as natural gas by steam reforming.⁵



The reaction requires natural gas and emits CO₂. Hydrogen has to be produced from water using natural energies such as sunlight for great economic and environmental interests. Therefore, direct splitting of water using a particulate photocatalyst would be a good way to produce clean and recyclable hydrogen on a large scale.⁶ There are several ways for solar hydrogen production from water.

- (i) Electrolysis of water using a solar cell, a hydroelectric power generator, etc.
- (ii) Reforming of biomass.
- (iii) Photocatalytic or photoelectrochemical water splitting (mimic photosynthesis).

Using a powdered photocatalyst for water splitting is the most simple method, as shown in figure 1.1. In a process that mimics photosynthesis, photocatalyst powders dispersed in water

absorb solar energy and convert water into H_2 and O_2 . Even though the separation of H_2 and O_2 evolved from the water splitting reaction is a disadvantage, the problem can be solved by using a Z-scheme photocatalyst system. Furthermore, powdered photocatalysts have an advantage for large-scale application of water splitting because of its simplicity. Therefore, H_2 from photocatalytic water splitting is a green and sustainable chemistry which can overcome energy and environmental issues resulting in an energy revolution.

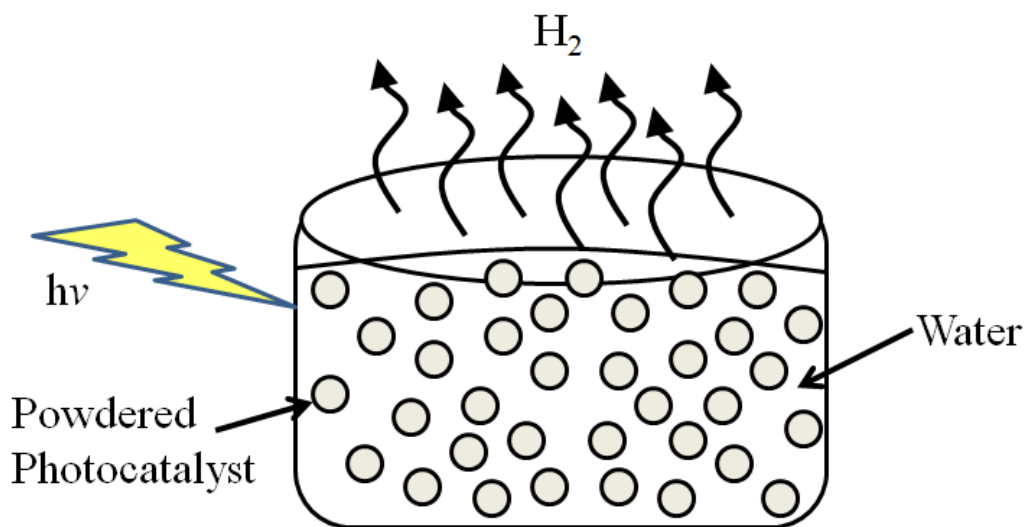


Figure 1.1 Conversion of solar energy to hydrogen energy by using powdered photocatalysts.

The water splitting reaction is the conversion of solar energy to chemical energy accompanied with a positive change in the Gibbs free energy as shown in Figure 1.2.⁵ It mimics the photosynthesis of green plants. Therefore, photocatalytic water splitting has the perspective of an artificial photosynthesis in chemistry. Based on the Gibbs free energy change of uphill reactions, photocatalytic water splitting is distinguished from photocatalytic degradation reactions such as photo-oxidation of organic compounds using oxygen molecules that are

generally downhill reactions.⁵ This downhill type reaction is regarded as a photoinduced reaction and has been extensively studied using TiO₂ photocatalysts.^{7,8}

The water splitting reaction of using TiO₂ as an electrode to process electrochemical photolysis reaction has been reported by Honda and Fujishima.⁹ Figure 3 shows the principle of electrons and holes generation from TiO₂ semiconductor electrodes under UV light. This reaction needs some external bias and pH adjusted solution. Electrons generated from electrochemical photolysis reduce water to form H₂ on the counter electrode (Pt) while holes oxidize water to form O₂ on the TiO₂ electrode. Over 130 materials are known to either do water splitting using semiconductor photoelectrodes or cause water oxidation or reduction in the presence of external redox agents.¹⁰ However, materials able to split water into H₂ and O₂ under visible light irradiation have not been found. Indeed, the solar energy conversion by water splitting using electrochemical photolysis or photocatalysts had been considered to be unrealistic, and the results are far from satisfactory. The efficiency of photo energy conversion by using powdered photocatalysts is not matched with the need for practical use. However, more and more new photocatalyst materials for water splitting have recently been discovered. This leads to advanced photocatalytic semiconductor research. Even though it is a marathon for photocatalytic water splitting, the optimistic mind is still being prepared for the challenge.

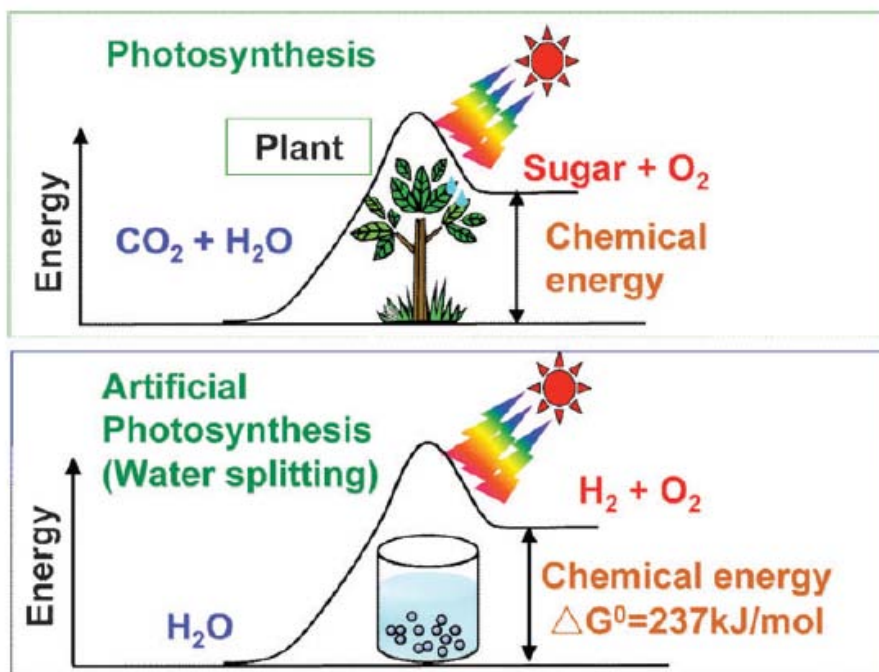


Figure 1.2 Comparison between photosynthesis of green plants and photocatalytic water splitting reaction.⁵

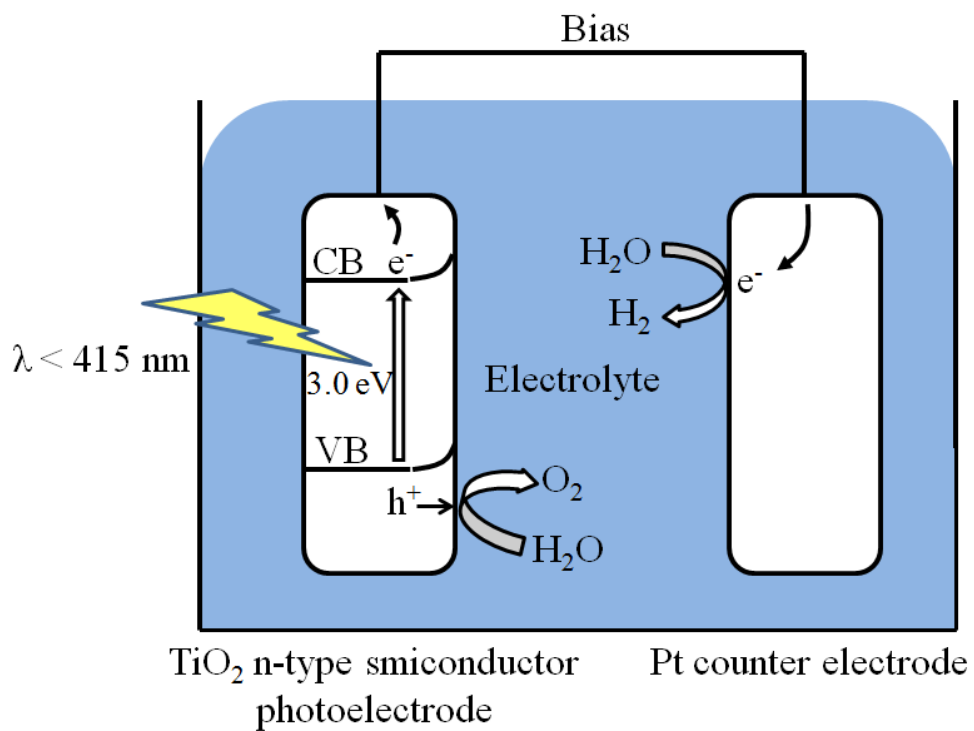


Figure 1.3 Water splitting by electrochemical photolysis using TiO₂ as photoelectrode.⁹

References

1. Law, M.; Greene, L. E.; Johnson, J. C.; Saykally, R.; Yang, P. D., Nanowire dye-sensitized solar cells. *Nature Materials* **2005**, 4, (6), 455-459.
2. Huynh, W. U.; Dittmer, J. J.; Alivisatos, A. P., Hybrid nanorod-polymer solar cells. *Science* **2002**, 295, (5564), 2425-2427.
3. Bach, U.; Lupo, D.; Comte, P.; Moser, J. E.; Weissortel, F.; Salbeck, J.; Spreitzer, H.; Gratzel, M., Solid-state dye-sensitized mesoporous TiO₂ solar cells with high photon-to-electron conversion efficiencies. *Nature* **1998**, 395, (6702), 583-585.
4. Gratzel, M., Photoelectrochemical cells. *Nature* **2001**, 414, (6861), 338-344.
5. Kudo, A.; Miseki, Y., Heterogeneous photocatalyst materials for water splitting. *Chemical Society Reviews* **2009**, 38, (1), 253-278.
6. Bard, A. J.; Fox, M. A., Artificial Photosynthesis: Solar Splitting of Water to Hydrogen and Oxygen. *Accounts of Chemical Research* **1995**, 28, (3), 141-145.
7. Fujishima, A.; Rao, T. N.; Tryk, D. A., Titanium dioxide photocatalysis. *Journal of Photochemistry and Photobiology C: Photochemistry Reviews* **2000**, 1, (1), 1-21.
8. Sheppard, L. R.; Bak, T.; Nowotny, J.; Nowotny, M. K., Titanium dioxide for solar-hydrogen V. Metallic-type conduction of Nb-doped TiO₂. *International Journal of Hydrogen Energy* **2007**, 32, (14), 2660-2663.
9. Fujishima, A.; Honda, K., electrochemical photolysis of water at a semiconductor electrode. *Nature* **1972**, 238, (5358), 37.
10. Osterloh, F. E., Inorganic Materials as Catalysts for Photochemical Splitting of Water. *Chemistry of Materials* **2008**, 20, (1), 35-54.

Chapter 2 - Basis of photocatalytic water splitting

Figure 2.1 shows the process of photocatalytic semiconductor water splitting. The first step is based on photon absorption and forming electron-hole pairs. The band structure of semiconductors strongly affects photocatalytic properties. For H_2 evolution to happen, the conduction band potential of the semiconductor must be higher than the proton reduction potential of 0.0 V vs NHE at pH = 0 (-0.41 V at pH = 7).¹ The potential of the valence band edge must exceed the oxidation potential of water of +1.23 V vs NHE at pH = 0 (+0.82 V at pH = 7) as shown in figure 2.2. Moreover, the band levels usually shift with a change in pH (-0.059 V/pH) of solution for oxide materials.²⁻⁴ Band-gap of semiconductor which does not match with oxidation or reduction potential usually requires a bias voltage, pH adjustment or external redox reagents to drive the reaction. Based on these criteria, a band-gap energy of 1.23 eV is a theoretical minimum requirement for driving the water splitting reaction, which corresponds to a wavelength of 1100 nm light. Band levels of various semiconductor materials are shown in figure 2.3. The band gap achieved so far is 2.3 eV in $NiO/RuO_2-Ni:InTaO_4$.^{5,6} Band-gap levels of ZrO_2 , $KTaO_3$, $SrTiO_3$ and TiO_2 are suitable for water splitting. But these materials are only active for water splitting when they are loaded with co-catalysts such as Pt, Ru or Rh. The band-gap of CdS seems to have a suitable visible light absorption to drive water splitting. But S^{2-} in CdS is oxidized rather than H_2O by photogenerated holes. This reaction is called photocorrosion and often results in metal sulfide photocatalysts having a short lifetime. However, CdS is an excellent photocatalyst for H_2 evolution under visible light irradiation if a hole scavenger is present. For O_2 evolution, WO_3 is a good photocatalyst under visible light with an electron acceptor such as Ag^+ and Fe^{3+} . If the photocatalyst is visible-light-driven, it should have a

narrower band-gap than 3.0 eV ($\lambda > 415$ nm). Therefore, band-gap engineering is necessary for photocatalysts having a water splitting activity under visible light. Furthermore, overall water splitting using a two-step photoexcitation system (Z-scheme) mimicking photosynthesis in a green plant also has been studied.⁷⁻¹¹ The two-step photoexcitation systems (figure 2.4) apply two small band-gap semiconductors which can be combined to drive the oxidation/reduction reaction by separate processes. Some Z-scheme visible-light responsive systems have been reported.¹⁰⁻¹² These constructed photocatalysis systems usually need to use an $\text{IO}^{-3}/\text{I}^{-}$ redox couple or $\text{Fe}^{3+}/\text{Fe}^{2+}$ electron as an electron mediator.

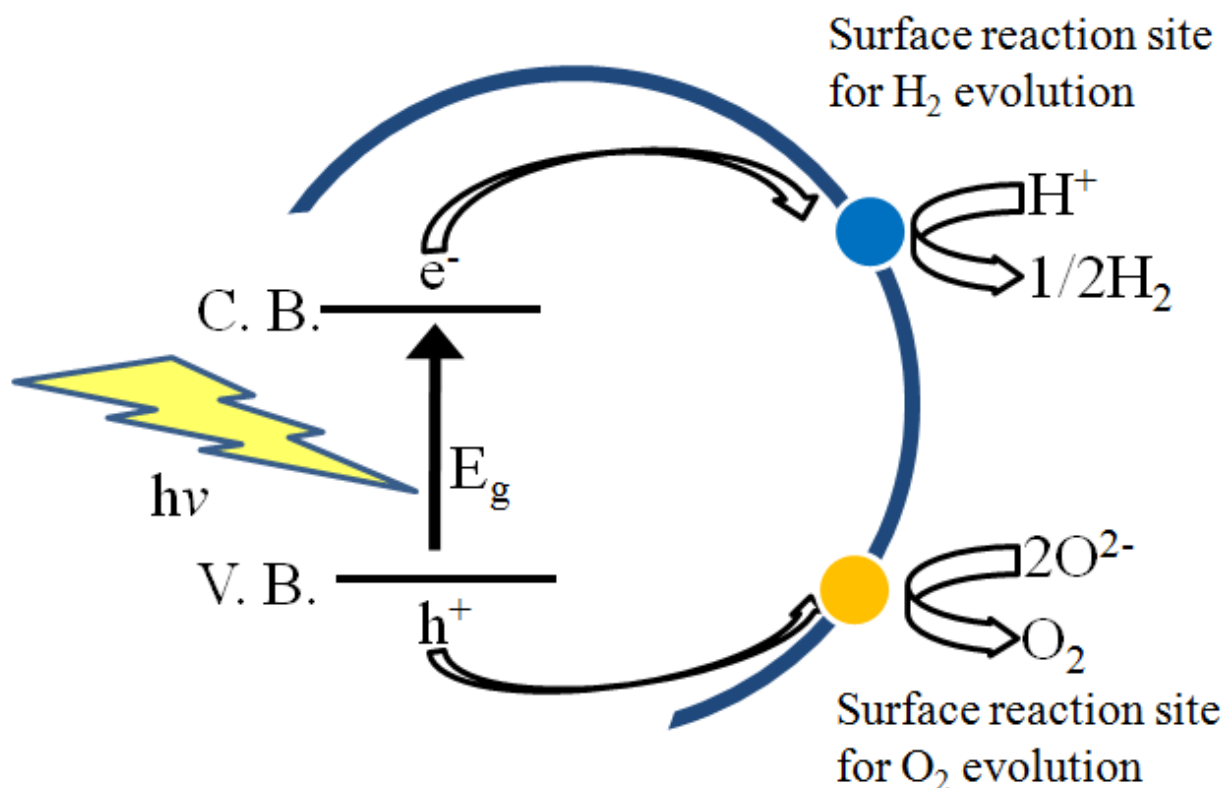


Figure 2.1 Main processes in photocatalytic water splitting.

The second step involves charge separation and migration. The separated charges migrate to surface reaction sites and react with water. The recombination of electron-hole pairs suppresses the photocatalytic water splitting reaction. Therefore, crystallinity and particle size strongly affect water splitting activity. The high crystalline quality results in a small amount of defects. Because the defects act as trapping and recombination centers for photogenerated electrons and holes, they result in a decrease in photocatalytic activity. On the other hand, the migration distance of photogenerated electrons and holes to reaction sites on the surface are based on particle size. When particle size becomes small, the distance becomes short, which results in a decreased probability of recombination and a higher activity.

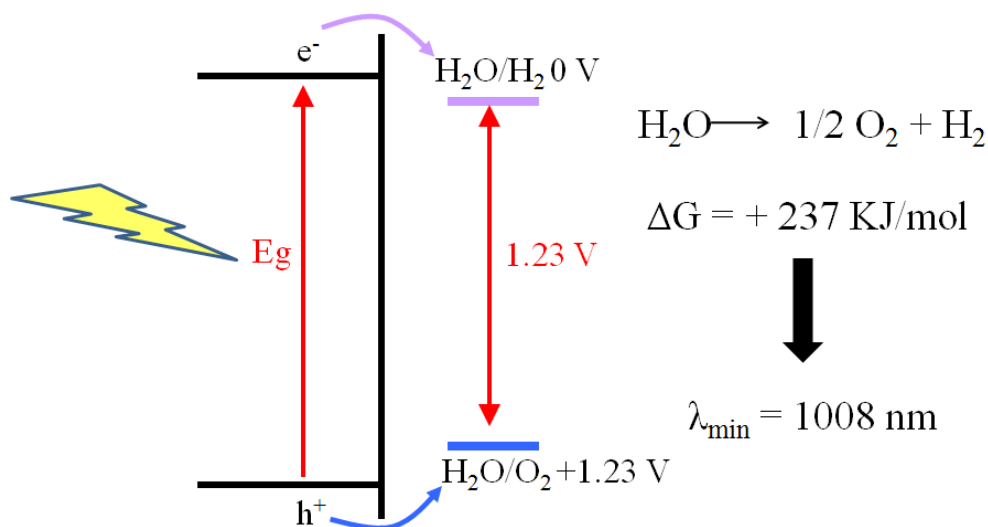


Figure 2.2 Principle of water splitting using semiconductor photocatalysts.

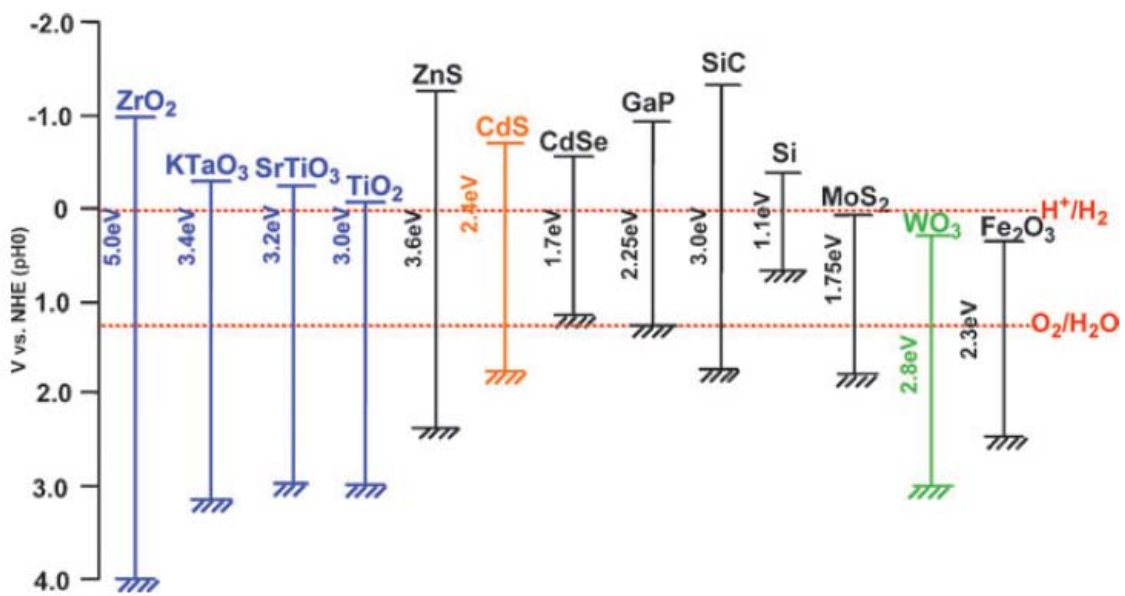


Figure 2.3 Relationship between band structure of semiconductor and redox potentials of water splitting.¹³

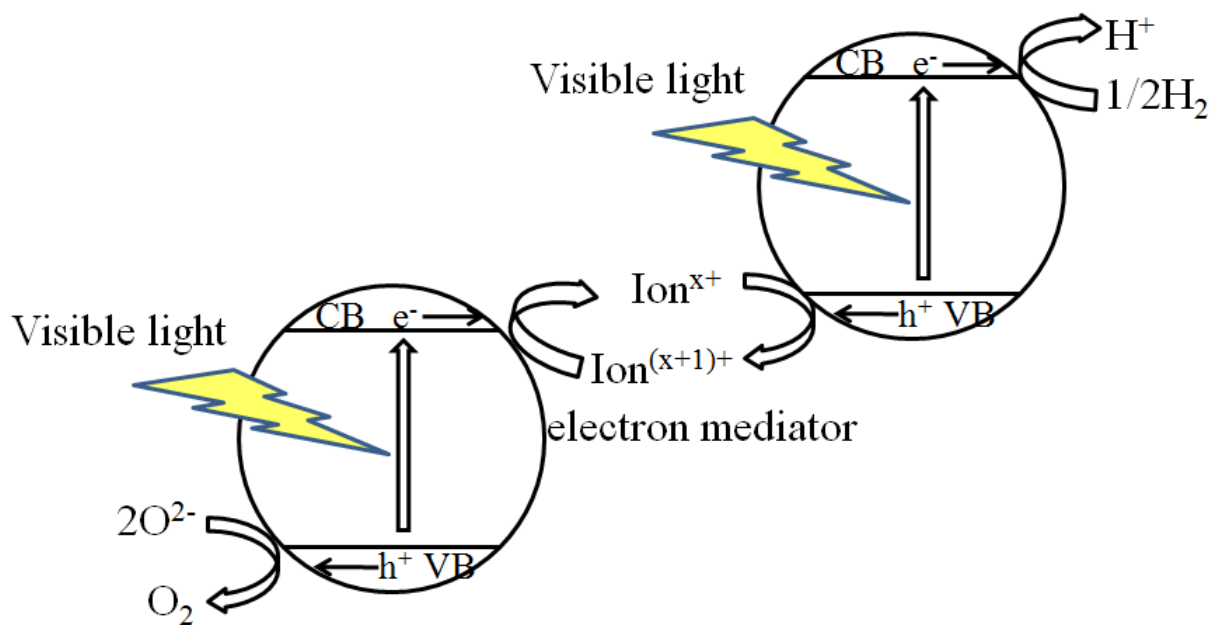


Figure 2.4 Mechanism of overall water splitting using the Z-scheme photocatalysis system driven by electron transfer photocatalysts.

The surface chemical reactions are the final step. Surface character (active sites) and quantity (surface area) strongly affect this step. The photogenerated electrons and holes will recombine with each other even if they carry thermodynamically sufficient potentials for water splitting, when the active sites for redox reactions do not exist on the surface. Pt, NiO, Rh and RuO₂ are usually used as co-catalysts for active sites for H₂ evolution. These co-catalysts help the oxide photocatalysts, which normally do not have high enough conduction band levels to reduce water and produce H₂. O₂ evolution usually does not need co-catalysts, even though the process needs 4-electron oxidation of water on active sites. This is the characteristic point of heterogeneous photocatalysts being different from homogeneous photocatalysts for which O₂ evolution with 4-electron oxidation of H₂O is a challenging reaction.¹⁴ Moreover, the evolved H₂ and O₂ can easily react with each other and turn back to water. Therefore, co-catalyst should not aid the back reactions on the reactive sites. The Fe³⁺/Fe²⁺ electron mediator is indispensable for overall water splitting using the Z-scheme system employing Pt/SrTiO₃: Rh because the iron ion not only shuttles the carriers but also suppresses a back reaction to form water from evolved H₂ and O₂ on the Pt cocatalyst by covering the Pt surface with iron species.^{7, 12, 15} In contrast to the Pt cocatalyst, a Ru cocatalyst is an effective cocatalyst that does not enhance the back reaction.⁸

Many materials of photovoltaic, phosphors and dielectric are also photocatalysts. However, the significant difference between the photocatalyst and the other materials is that chemical reactions are involved in the photocatalytic process, but not in the other physical properties.¹⁴ Photocatalytic activities are achieved only when three steps are simultaneously completed. Thus, crystalline quality, particle size and reactive sites on the surface are required for photocatalysts. Photocatalysts need to be highly functional materials.

References

1. Osterloh, F. E., Inorganic Materials as Catalysts for Photochemical Splitting of Water. *Chemistry of Materials* 2007, 20, (1), 35-54.
2. Grätzel, M., Energy resources through photochemistry and catalysis. Academic Press: New York, 1983; p xiv, 573 p.
3. Nozik, A. J., Photoelectrochemistry: Applications to Solar Energy Conversion. *Annual Review of Physical Chemistry* 1978, 29, (1), 189-222.
4. Gurevich, I. U. I. A.; Pleskov, I. U. V., Semiconductor photoelectrochemistry. Consultants Bureau: New York, 1986; p xxv, 422 p.
5. Zou, Z.; Arakawa, H., Direct water splitting into H₂ and O₂ under visible light irradiation with a new series of mixed oxide semiconductor photocatalysts. *Journal of Photochemistry and Photobiology A: Chemistry* 2003, 158, (2-3), 145-162.
6. Zou, Z.; Ye, J.; Sayama, K.; Arakawa, H., Direct splitting of water under visible light irradiation with an oxide semiconductor photocatalyst. *Nature* 2001, 414, (6864), 625-627.
7. Sasaki, Y.; Nemoto, H.; Saito, K.; Kudo, A., Solar Water Splitting Using Powdered Photocatalysts Driven by Z-Schematic Interparticle Electron Transfer without an Electron Mediator. *The Journal of Physical Chemistry C* 2009, 113, (40), 17536-17542.
8. Sasaki, Y.; Iwase, A.; Kato, H.; Kudo, A., The effect of co-catalyst for Z-scheme photocatalysis systems with an Fe³⁺/Fe²⁺ electron mediator on overall water splitting under visible light irradiation. *Journal of Catalysis* 2008, 259, (1), 133-137.
9. Fujihara, K.; Ohno, T.; Matsumura, M., Splitting of water by electrochemical combination of two photocatalytic reactions on TiO₂ particles. *Journal of the Chemical Society, Faraday Transactions* 1998, 94, (24), 3705-3709.
10. Sayama, K.; Mukasa, K.; Abe, R.; Abe, Y.; Arakawa, H., Stoichiometric water splitting into H and O using a mixture of two different photocatalysts and an IO³⁻/I⁻ shuttle redox mediator under visible light irradiation. *Chemical Communications* 2001, (23), 2416-2417.
11. Abe, R.; Takata, T.; Sugihara, H.; Domen, K., Photocatalytic overall water splitting under visible light by TaON and WO₃ with an IO³⁻/I⁻ shuttle redox mediator. *Chemical Communications* 2005, (30), 3829-3831.

12. Kato, H.; Hori, M.; Kato, R.; Shimodaira, Y.; Kudo, A., Construction of Z-scheme type heterogeneous photocatalysis systems for water splitting into H₂ and O₂ under visible light irradiation. *Chemistry Letters* 2004, 33, (10), 1348-1349.
13. Serpone, N.; Pelizzetti, E., *Photocatalysis : fundamentals and applications*. Wiley: New York, 1989; p x, 650 p.
14. Kudo, A.; Miseki, Y., Heterogeneous photocatalyst materials for water splitting. *Chemical Society Reviews* 2009, 38, (1), 253-278.
15. Kato, H.; Sasaki, Y.; Iwase, A.; Kudo, A., Role of Iron Ion Electron Mediator on Photocatalytic Overall Water Splitting under Visible Light Irradiation Using Z-Scheme Systems. *Bulletin of the Chemical Society of Japan* 2007, 80, (12), 2457-2464.

Chapter 3 - Titanium-Indium Oxynitrides for Water Splitting.

Photocatalysis vs. Light Induced Catalyst Oxidation by Water

3.1 Introduction

Osterloh¹ has recently reviewed inorganic materials for photochemical water splitting. Over 130 inorganic materials/composites are mentioned. Most successful composites contain co-catalysts, and NiO modified La/K/TaO₃,² and NiO modified La₄CaTi₅O₁₇³ appear to be the most efficient photocatalysts yet reported.

Metal nitrides and metal-oxynitride composites have also received some study.¹ For example, Domen and coworkers investigated a solid solution of GaN and ZnO with RuO₂ nanoparticles to achieve overall water splitting.^{4,5} These studies revealed that the photocatalytic activity for water splitting depends on the crystallinity and composition of the material.

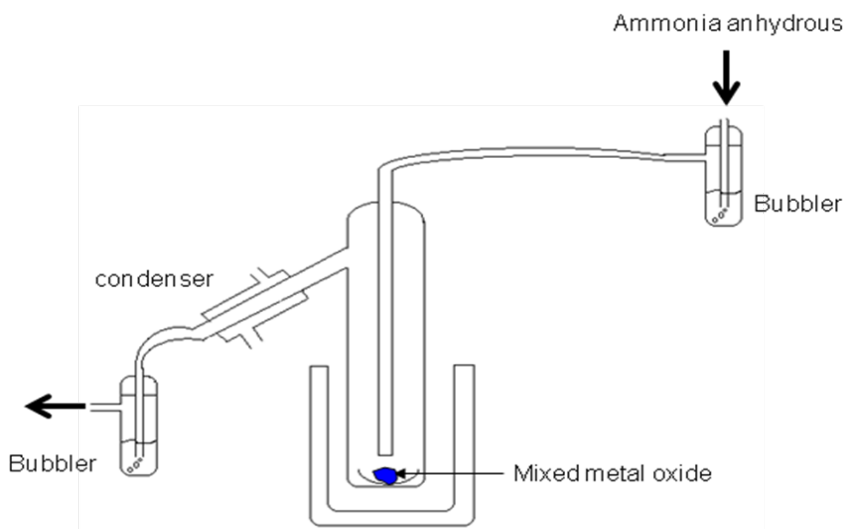
Another study describes advanced visible-light-driven photocatalysts by focusing on the refinement of non-oxide-type photocatalysts; this study used Nitrogen to replace Oxygen in TiO₂ to form TiO_{2-x}N_x.^{6, 7} Additionally, Poznyak and co-workers⁸ have investigated the photoelectrochemical properties of nanocrystalline TiO₂/In₂O₃ composite solids. It was shown that TiO₂/In₂O₃ composites allow efficient separation of photogenerated charge carriers occurring in interconnected TiO₂ and In₂O₃ particles, owing to the favorable energetics of the conduction bands of these oxides. Another report⁹ shows that nitrogen-doped In₂O₃ thin film electrodes are effective for photocatalytic water splitting. Therefore, it may be possible to combine the TiO₂ property of formation of electrons and holes by absorbing light and then using the interconnection between TiO₂ and In₂O₃ to transfer the holes to In₂O₃. We considered that partially nitrated composites of titanium and indium oxides may be effective in water splitting

under visible light. In our research, optimal preparation conditions were investigated in order to achieve the best hydrogen production. Reported herein are our results with pure water and with Ethanol-water solutions.

3.2 Experimental

3.2.1 Preparation of Ti-In nitride composites

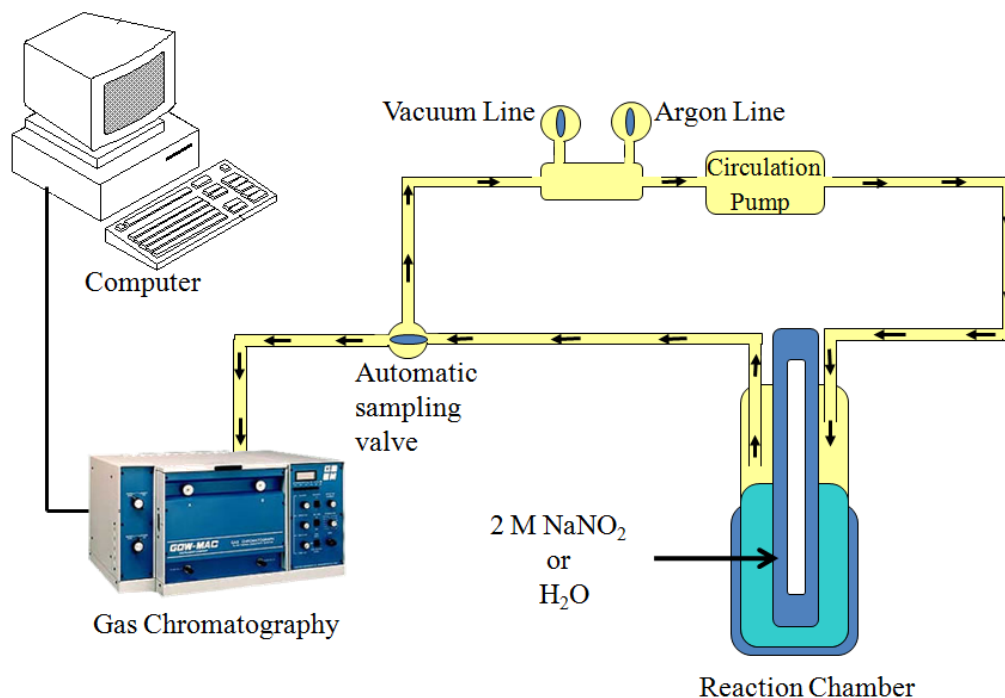
Composite powders were prepared by heating a mixture of 0.92 g (1.2×10^{-2} mol) anatase TiO_2 powder (Sigma-Aldrich, anatase, nanopowder, <25nm, 99.7%) and 3.2 g (1.2×10^{-2} mol) In_2O_3 powder (Sigma-Aldrich, nanopowder, <100nm, 99.9%) at different temperatures under NH_3 flow (250 mL/min) for 20 hours as shown in Figure 3.1 (The reaction chamber diameter is 4.5 cm). The mole ratio of Ti to In in the starting material (TiO_2 and In_2O_3) was 1/1, which should give a Ti:In ratio of 1:2. After 20 hours of ammonolysis, the sample was cooled to room temperature under NH_3 flow.



3.1 Experimental setup for nitridation of $\text{TiO}_2/\text{In}_2\text{O}_3$ mixture.

3.2.2 Hydrogen Production

The reactions were carried out in a glass-enclosed reaction chamber connected to a gas circulation and evacuation system with a quartz inner irradiation-type reaction vessel shown in figure 3.2. The apparatus contained 400 ml distilled water solution with 0.13 g sulfuric acid and 0.30 g of the composite Ti-In (oxy)nitride. The reactant solution was evacuated and filled with argon three times to remove air completely, followed by irradiation ($\lambda > 400$ nm) under a 450 W high-pressure Hg lamp via a quartz tube that was air filled for full spectrum UV-vis studies, or filled with 2 M NaNO₃ aqueous solution for visible light studies. The reaction temperature was controlled between 20 to 25 °C. H₂ production was monitored during the reaction with an online GC system (GOMAC model) employing a Supelco molecular 80/100 sieve 5A column with Ar as the carrier gas and a thermal conductivity detector (TCD).



8

3.2 Experimental setup for hydrogen production measurement.

3.2.3 Characterization of Composites

The prepared samples were studied by powder X-ray diffraction (XRD; Bruker D8 X-ray diffractometer with Cu K α radiation), scanning electron microscopy (SEM; Hitachi S-3500 N), UV-visible diffuse reflectance spectroscopy (DRS; Varian Cary 500 Scan). The Brunauer, Emmett, Teller (BET) surface area was measured with a Quantachrome NOVA-1200 instrument at liquid nitrogen temperature. X-ray photoelectron spectroscopy (XPS) was conducted using a SPECS Sage100 spectrometer operating in the fixed analyzer transmission mode using achromatic Mg K α (1253.6 eV) radiation at 240 W (12 kV and 20 mA) using a water-cooled X-ray gun cap and evacuated with turbomolecular pumping. The base pressure of the chamber was about 2×10^{-8} Torr, and the energy scales were calibrated using copper and the separation between photoelectron peaks generated by Mg and Al K α X-rays. Survey spectra were collected with a pass energy of 30 eV; a pass energy of 15 eV was used for both core and valence band spectra. Many of the spectra were calibrated by taking the C 1s peak due to residual hydrocarbon as being at 284.4 eV.

3.3 Results and Discussion

3.3.1 Crystal Structure

The structure of materials can be determined by Powder X-ray diffraction (XRD). But this technique has a limitation for disordered and amorphous materials. The XRD pattern is unique for each material, so there is no identical pattern for different substances. There is a lot of available data containing standard patterns that people can use to identify pure substance or crystalline phases by simple searching and matching procedures.

The arrangement of atoms in the crystal can be observed when an X-ray beam excites the atoms in the solid sample. The electrons of these atoms start to oscillate and form a constructive interference. The diffracted beam in the same phase mutually reinforces one another.

The theta angle (θ) of incident and reflected rays diffraction can be explained by Bragg's Law. The unit cell dimensions (d) can be express:

$$2d \sin\theta = n\lambda \quad (3.1)$$

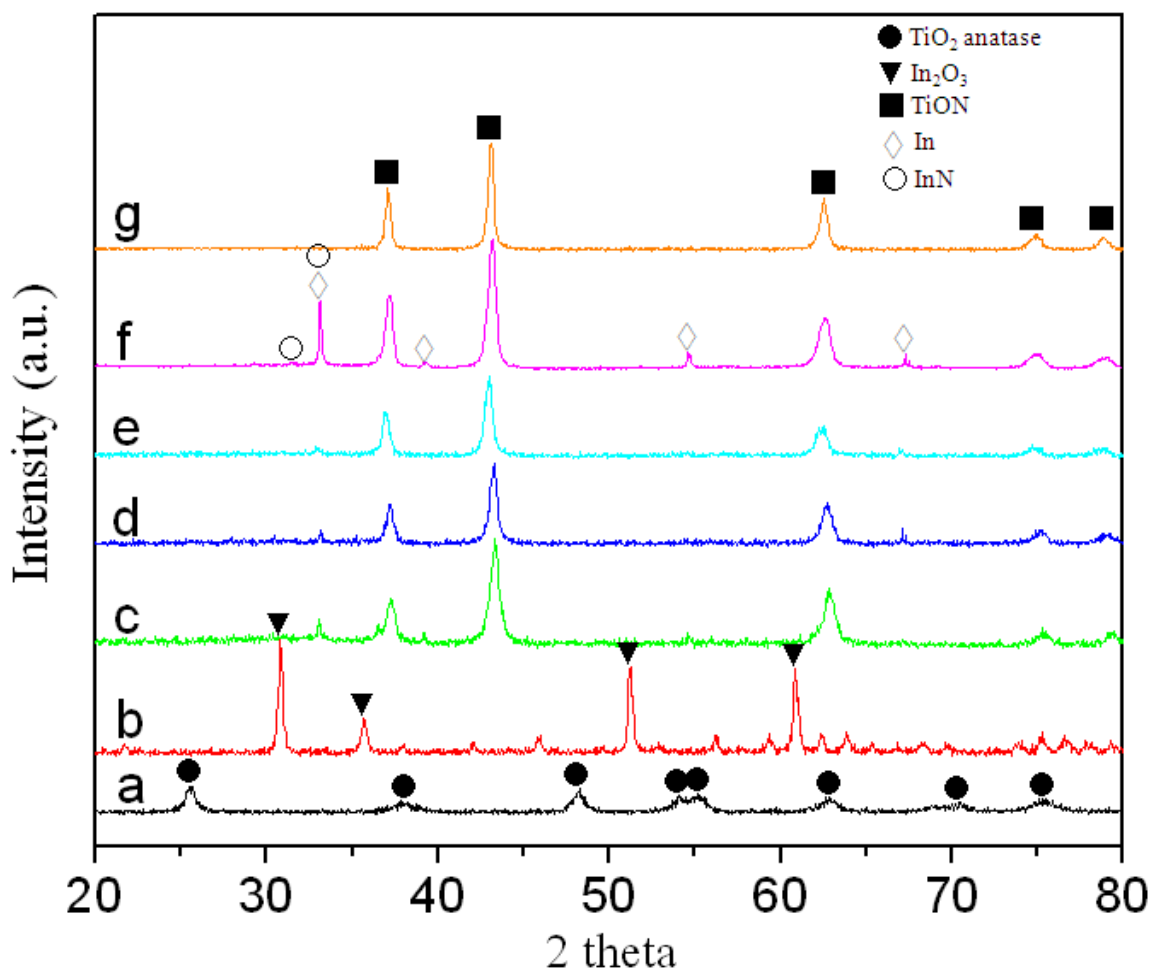
The crystallite sizes of samples can be calculated from the XRD spectra using the Debye-Scherrer equation:

$$D = \frac{K\lambda}{B \cos\theta_B} \quad (3.2)$$

Where D is the thickness of the crystal (\AA); K is a constant depends on the crystallite shape; λ is the X-ray wavelength (1.54051 \AA for $\text{CuK}\alpha$); θ_B is the Bragg angle (between incident and diffracted beam); B is FWHM (Full-Width Half-Maximum) in radians.

Figure 3.3 shows XRD patterns from samples obtained by nitriding a mixture of TiO_2 and In_2O_3 at several ammonolysis temperatures. TiO_2 , In_2O_3 and TiN data are shown for comparison. All composites' patterns are similar to TiN and the peak assignments are based on the ICSD database. None of the diffraction peaks of starting materials were observed, indicating that the obtained samples were not physical mixtures of TiO_2 and In_2O_3 . The peak around 34° corresponds to both InN and In metal. The XRD data demonstrate that an ammonolysis temperature above 850°C , caused an increase of In metal formation (which was generally lost due to its volatility). It is known that In_2O_3 is reduced to metallic Indium upon ammonolysis of Indium oxide by anhydrous ammonia above 650°C .¹⁰ Indeed, we found that starting with only In_2O_3 and then nitridation, indium metal was produced under the action of hot NH_3 . The high ammonolysis temperature not only reduced In^{3+} into In , but also could cause InN decomposition.

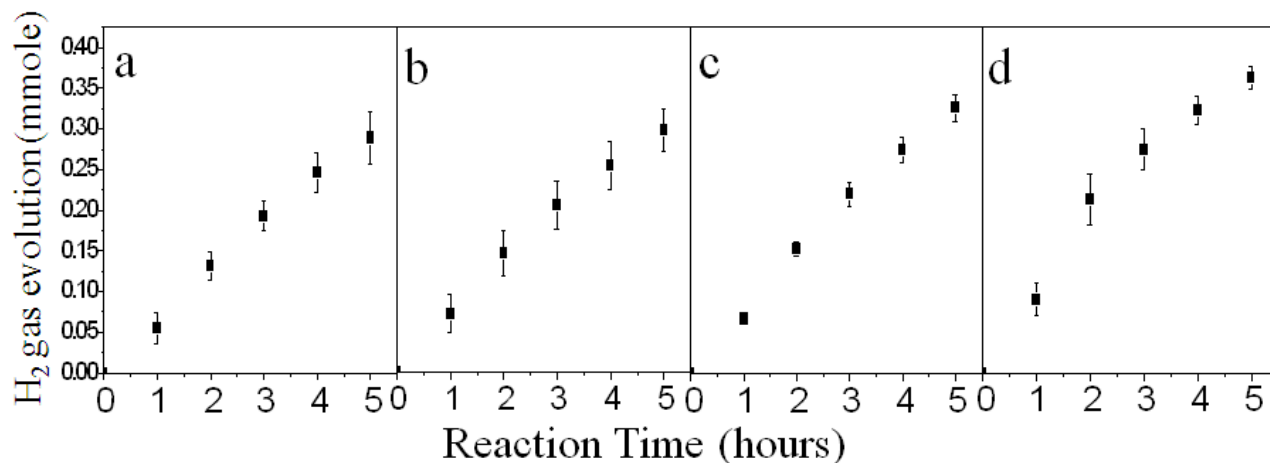
Decomposition temperatures reported for InN range from 500 °C for thin films^{11, 12} to 710 °C. In our research, even when the ammonolysis temperature was above 700 °C, some InN persisted when TiO₂ was also present as a co-reactant. Therefore, combining TiO₂ and In₂O₃ not only created H₂ production activity, but also helped to stabilize InN, and Indium Nitride is a key for H₂ generation performance. Normally, we found that the stronger the peak intensity for InN, the higher the efficiency of the hydrogen production. The full width at half maximum (FWHM) for the InN XRD peak varied for 700 °C, 750 °C, 800 °C and 850 °C ammonolysis temperature samples and at 43° were 0.61, 0.48, 0.49 and 0.49 degree, respectively. Therefore, hydrogen production was highest (samples d, e of Figure 3.3) when the crystallites were smaller.



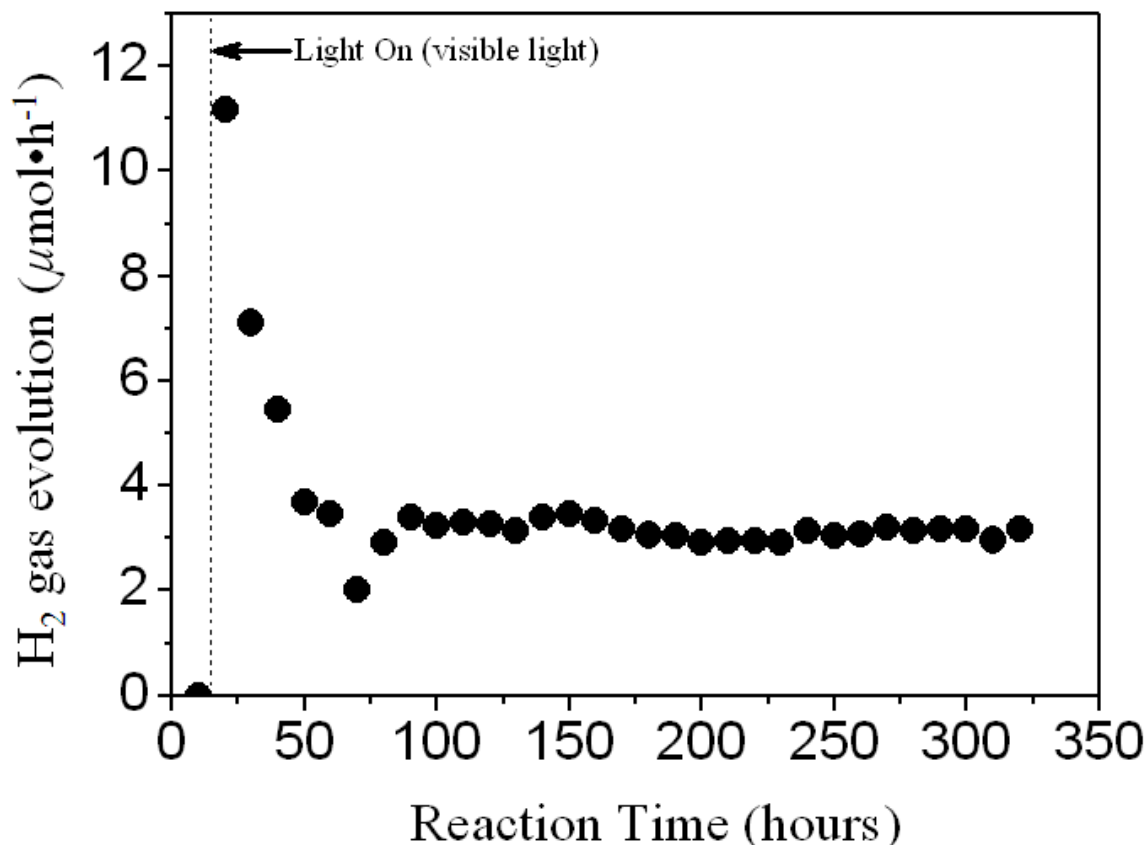
3.3 Powder XRD patterns obtained by nitriding a mixture of TiO₂ and In₂O₃ at different ammonolysis temperatures (c) 700 °C (d) 750 °C (e) 800 °C (f) 850 °C for 20 hours under a 250 mL/ min flow rate of NH₃. (a) TiO₂ anatase (b) In₂O₃ (g) TiN.

Slightly Acidic Pure Water

Figure 3.4 shows the H₂ evolution results in pH adjusted (sulfuric acid) pure water under UV-Vis light and reaction temperature was controlled between 20 to 25 °C. The starting slurry solution pH was adjusted to ~2.6, and after reaction the pH increased to 2.9. We believed that the pH adjustment would allow the H₂O/H₂ reducing potential to be better matched to the conducting band of the composites.¹³ Experiments were repeated at least three times. The comparative hydrogen production rates varied somewhat with ammoniolysis temperatures: (a) 58 (b) 59 (c) 65 (d) 73 μmole·h⁻¹. However, if the ammonolysis temperature was higher than 900 °C, only low activity was observed. Based on XRD data, the lower activity may be caused by forming more In metal than InN. The photocatalytic activity of Titanium (oxy)nitride (no indium) by using the same condition was also tested, and did not show activity; only the mixed Ti-In (oxy)nitride system was successful. Figure 3.5 shows the hydrogen production activity in pH adjusted (sulfuric acid) pure water under visible light. In the dark, there was no activity observed. However, after the light was on, the reaction can be driven by visible light, producing 11 μmoleh⁻¹ H₂ gas (~0.37 % quantum yield). After several hours of use with visible light, activity decreased. However, after 60 hours, the activity stabilized, and continued to produce H₂ gas at 4 μmole·h⁻¹ (~0.13 % quantum yield) for over 320 hours (Figure 3.5) and accumulated 1146 μmole H₂ gas.



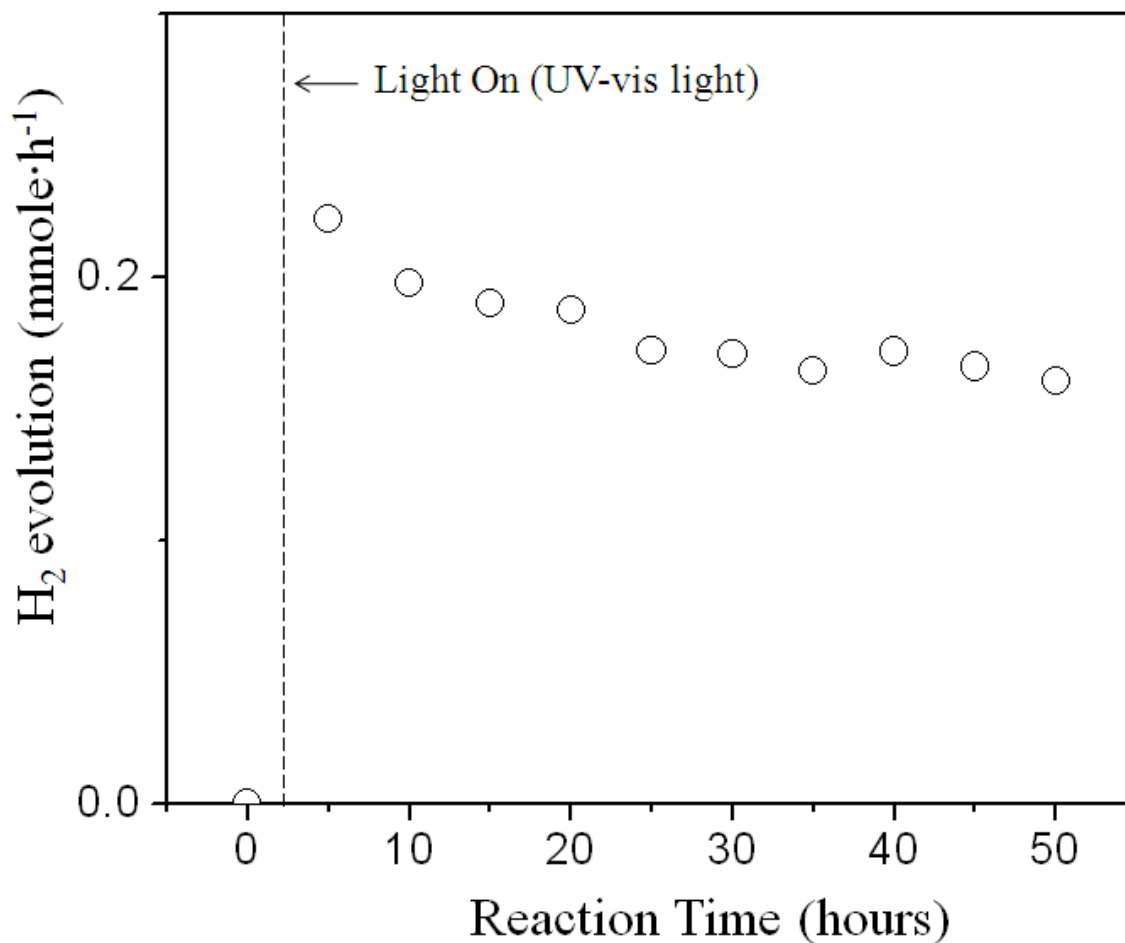
3.4 Dependence of UV-vis hydrogen production activity of nitrated mixture of TiO₂ and In₂O₃ at different ammonolysis temperatures (a) 700 °C (b) 750 °C (c) 800 °C (d) 850 °C for 20 hours under a 250 mL/ min flow rate of NH₃. Catalyst (0.3g), an aqueous slurry mixed with 0.13 g sulfuric acid (pH : ~2.6); light source, high-pressure mercury lamp (450 W); inner irradiation-type reaction vessel; reaction temperature was controlled between 20 to 25 °C.



3.5 Long term dependence of visible light hydrogen production activity of nitrated mixture of TiO₂ and In₂O₃ (750 °C ammonolysis temperatures for 18 hours under a 250 mL/ min flow rate of NH₃). Catalyst (0.3g), an aqueous solution mixed with 0.13 g sulfuric acid (pH : ~2.6); light source, high-pressure mercury lamp (450 W) with 2M NaNO₂ solution as light filter. Inner irradiation-type reaction vessel. Reaction temperature was controlled between 20 to 25 °C.

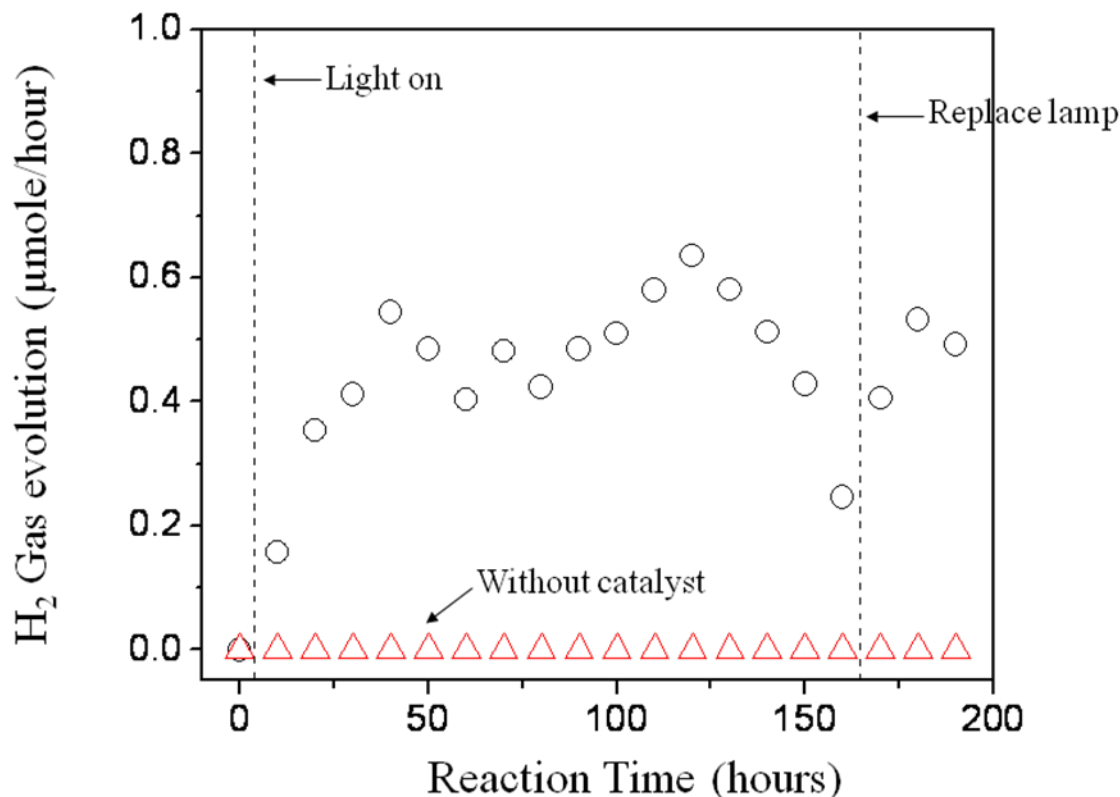
Water with Ethanol as a Sacrificial Agent

Sacrificial reagents are often employed to evaluate activity for H₂ production.¹⁴ Figure 3.6 shows the dependence of UV-Vis light activity of Ti-In (oxy)nitride (700 °C ammonolysis) in 20 % ethanol solution. It showed no activity in the dark. After turning on the light, the hydrogen production activity was observed at a high rate (222 μmol·h⁻¹) and very stable. This reaction was carried out for 50 hours and produced 9019 μmoles of hydrogen.



3.6 Dependence of UV-vis light hydrogen production activity of a nitrated mixture of TiO₂ and In₂O₃ at 700 °C ammonolysis temperatures for 20 hours under a 250 mL/ min flow rate of NH₃. Catalyst (0.3g), an 20 % ethanol aqueous solution; light source, high-pressure mercury lamp (450 W). Inner irradiation-type reaction vessel. Reaction temperature was controlled between 20 to 25 °C.

Fig. 3.7 shows the dependence of visible light activity of Ti-In (oxy)nitride (700 °C ammonolysis) in 10 % methanol solution. It showed no activity in the dark. Moreover, the control experiment (experiment without catalyst) also shows no H₂ production under visible light at any time. After turning on the light, hydrogen production activity was observed (~0.5 μmole·h⁻¹) and very stable. This reaction was carried out for 200 hours.



3.7 Long term dependence of visible light hydrogen production activity of nitrated mixture of TiO₂ and In₂O₃ (700 °C ammonolysis temperatures for 20 hours under a 250 mL/ min flow rate of NH₃). Catalyst (0.4 g), an 10 % methanol aqueous solution; light source, high-pressure mercury lamp (450 W) with 2M NaNO₂ solution as light filter. Inner irradiation-type reaction vessel. Reaction temperature was controlled between 20 to 25 °C.

3.3.2 Elemental composition of the TiInO_xY_z composites

Complete elemental analysis and subsequent empirical formulas of the composites before and after use in hydrogen production are shown in Table 3.1, and XRD spectra were given in Figure 3.8. Note that even before use, the amount of Indium is much lower than expected, and is almost gone in the after use sample (for the pure water long-term experiment). When a sacrificial agent (ethanol) was present, the empirical formula did not change upon use.

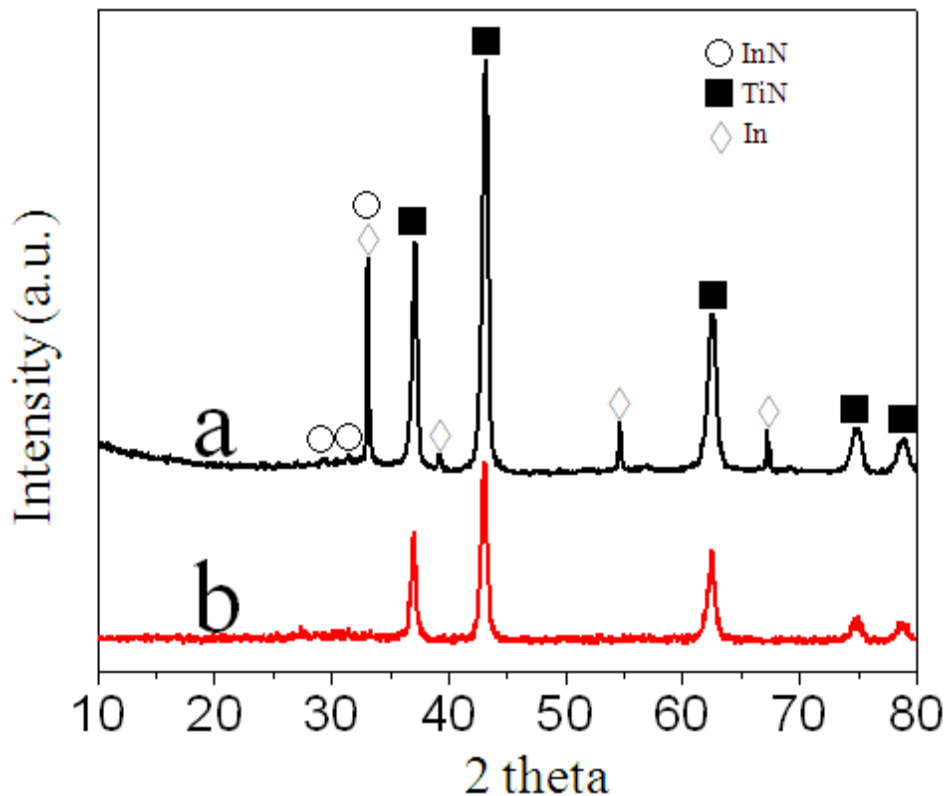
3.1 Elemental analysis before and after hydrogen production reaction of Ti-In (oxy)nitride (800 °C) under UV-vis light.

Analysis	Before reaction results	After reaction results	
		Pure water	Ethanol-water
Indium	4.08 %	1.4 %	4.3 %
Titanium	57.6 %	65.4 %	59.4 %
Nitrogen	10.5 %	15.5 %	10.5 %
Oxygen	27.8 %	17.7 %	25.7 %
Empirical Formula	$\text{TiIn}_{0.029}\text{N}_{0.63}\text{O}_{1.4}$	$\text{TiIn}_{0.0088}\text{N}_{0.8}\text{O}_{0.8}$	$\text{TiIn}_{0.031}\text{N}_{0.6}\text{O}_{1.3}$

With the starting material, assuming a stoichiometric reaction of the composite with water under the action of light (no reaction occurs in the dark), and assuming no photocatalytic reaction, a reasonable reaction can be written:



Using 0.3 g of composite, this equation predicts that about 2000 μmoles of H_2 could be produced. In an long term experiment about 1100 μmoles H_2 were produced in pure water. Thus, in pure water the reaction is not catalytic, but stoichiometric. This also explains why we did not observe the co-production of oxygen. So we have discovered a light driven reaction that is not very efficient (0.37 % quantum efficiency).



3.8 Powder XRD patterns of (a) before (b) after hydrogen production from water under UV-vis light obtained by nitriding a mixture of TiO_2 and In_2O_3 at 850°C for 20 hours under a 250 mL/min flow rate of NH_3 .

***These data show that the active composite is an intimate mixture of TiN and InN, and after use the InN has been destroyed, but TiN remains.**

On the other hand, when a sacrificial agent is present, the reaction is also light driven, but is much more efficient (2.2 % quantum efficiency) than using pure water. Furthermore, long term experiments show that the reaction must be catalytic since more than 9019 μmoles of hydrogen were produced.

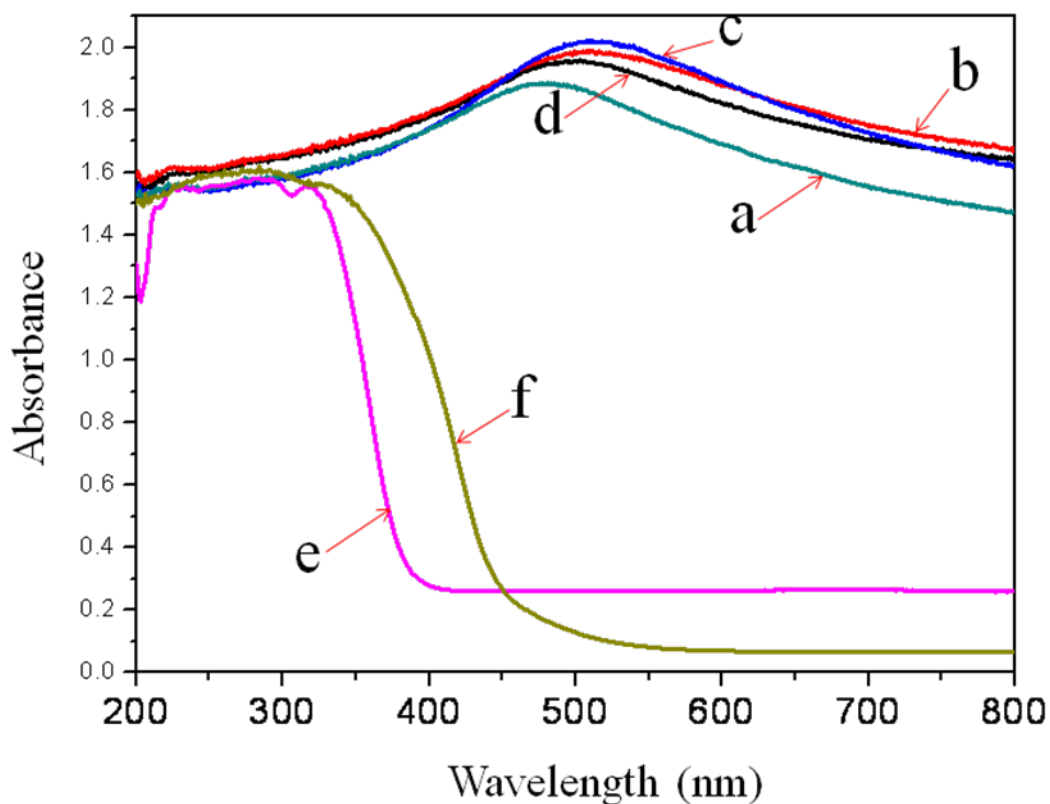
3.3.3 UV-Vis Diffuse Reflectance spectra

The Kubelka-Munk method is a solid-state diffuse reflection spectrum by converting reflection to absorbance through a UV-Visible-NIR spectrometer. Figure 3.9 shows UV-Visible

diffuse reflectance spectra for solid composites prepared by 20 hours of nitriding over several ammonolysis temperatures, along with TiO₂ and In₂O₃ for comparison. The UV-Visible spectra for the nitrated catalysts show a special phenomenon of having maximum absorbance in the visible region. Table 3.2 shows the maximum absorbance wavelength and band gap energies of Ti-In (oxy)nitride samples prepared by different ammonolysis temperatures. It demonstrates that the maximum absorbance can be adjusted by different synthetic methods. Based on UV-Visible spectra, the hydrogen production is affected by total absorbance and maximum absorbance position. The shorter the wavelength maximum, but still in the visible range, the higher the activity (Table 3.2).

3.2 The maximum absorbance wavelength, Band Gap Energies and hydrogen production rates in pure water of Ti-In (oxy)nitride samples prepared by different ammonolysis temperatures

Ammonolysis temperature	Surface Area (m ² /g)	Maximum absorbance Wavelength (nm)	Band gap (eV)	H ₂ gas evolution (μmmole · h ⁻¹)
700 °C	12.4	625	1.98	58
750 °C	13.5	465	2.67	59
800 °C	22	525	2.36	65
850 °C	8.5	470	2.64	73



3.9 UV-Vis diffuse reflectance spectra of samples obtained by nitriding a mixture of TiO_2 and In_2O_3 at different ammonolysis temperatures (a) 700 °C (b) 750 °C (c) 800 °C (d) 850 °C for 20 hours under a 250 mL/ min flow rate of NH_3 . (e) Titanium dioxide (f) Indium oxide.

3.3.4 X-ray Photoelectron Spectroscopy

X-ray photoelectron spectroscopy (XPS) is a quantitative spectroscopic technique that provides information on surface elemental composition, empirical formula, chemical state and electronic state of the elements. XPS spectra are obtained by irradiating a material with a beam of X-rays while simultaneously analyzing the kinetic energy and number of electrons that escape from the 1 to 10 nm depth of the material surface. The energy of a photon of all types of electromagnetic radiation is given by the Einstein relation:

$$E = h\nu \quad (3.3)$$

Where h is Planck constant (6.62×10^{-34} J s) and ν is frequency (Hz) of the radiation. The sample is placed in an ultrahigh vacuum environment and photoelectron spectroscopy uses monochromatic sources of radiation (i.e. photons of fixed energy). The x-ray photon is absorbed by an atom in a molecule or solid, leading to the ionization and emission of a core (inner shell) electron. The electron energy analyser records kinetic energy distribution of the emitted photoelectrons (i.e. the number of emitted photoelectrons as a function of their kinetic energy) resulting in a photoelectron spectrum. The spectrum represents the surface composition, which is obtained by counting the number of photoelectrons and Auger electrons as a function of their energy. The energy corresponding to each peak is characteristic of an element present in the sampled volume. The spectrum peak area is a measure of the relative amount of the element. The peak shape and precise position indicates the chemical state for the element. However, XPS is a surface sensitive technique because only the electrons generated near the surface can escape and are detected. Due to inelastic collisions within the sample's atomic structure, photoelectrons of interest have relatively low kinetic energy. Those photoelectrons that originate more than 20 to 50 Å below the surface cannot escape with sufficient energy to be detected.

We have examined four areas of the XPS spectra for several samples: the Ti 2p region (466-453 eV), In 3d region (450-454 eV), the O 1s region (525-537 eV), and the N 1s region (394-400 eV).

3.3.4.1 C 1s Core Level

The survey spectra of all the Ti-In (oxy)nitride powders confirmed the presence of Ti, In, O, N and C. The binding energies (BEs) were calibrated using the C 1s energy of 284.4 eV as an internal calibration.

3.3.4.2 Ti 2p Core Level

The Ti 2p_{3/2} has three peaks (Figure 3.10A), 458.5 eV, 457 eV and 455.6 eV. Ti 2p_{5/2} has three peaks, 463.9 eV, 462.5 eV and 461.3 eV. They are in agreement with the values reported in the literature for Ti⁴⁺, Ti³⁺ and Ti²⁺, respectively.^{10, 15} The XPS data show that the ammonolysis process can reduce Ti⁴⁺ to lower oxidation states. Moreover, the low ammonolysis temperature samples have a higher ratio of Ti⁴⁺, which shows that higher ammonia treatment temperature causes more reduction of Ti⁴⁺ into Ti³⁺ or Ti²⁺.

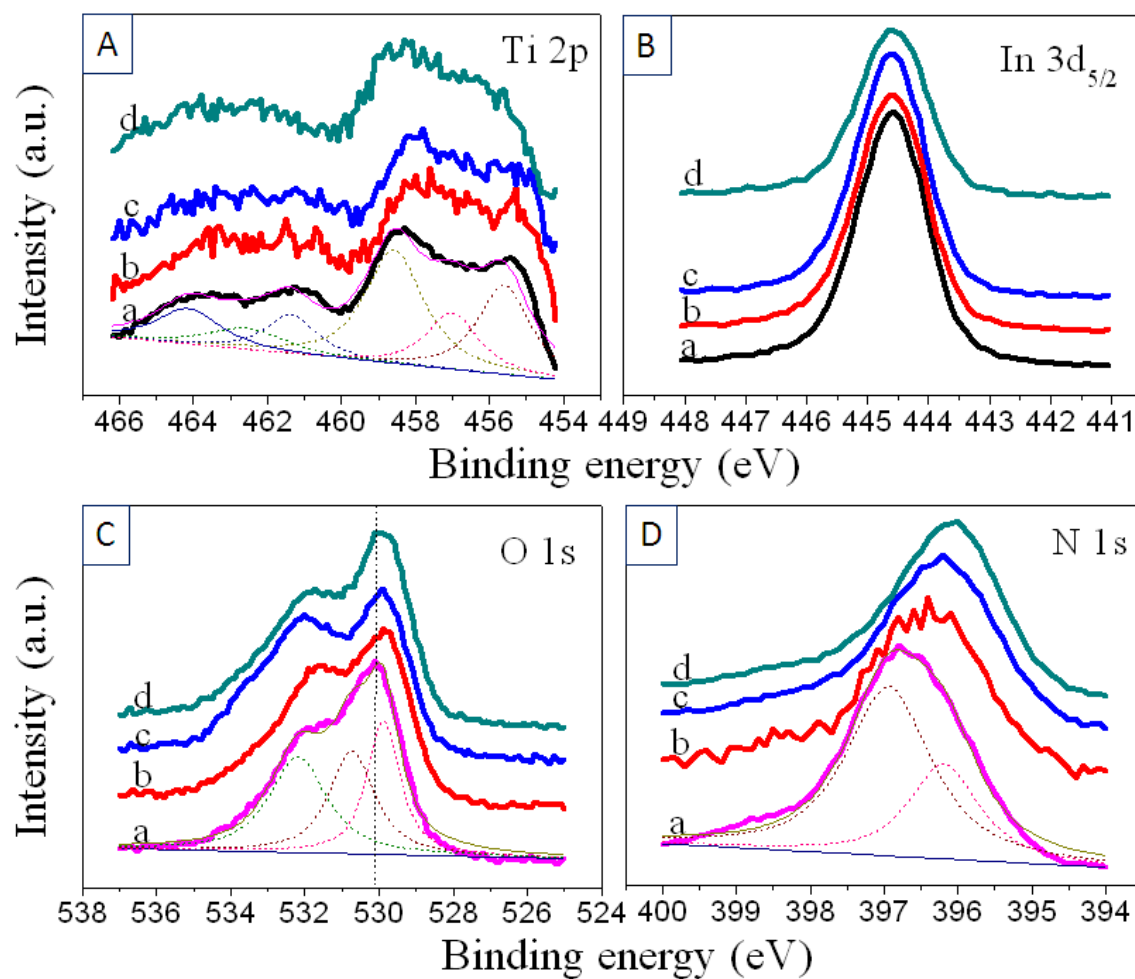
Figure 3.11 shows a comparison of XPS spectra before and after the H₂ production reaction in pure water (different ammonolysis temperatures). In the Ti 2p XPS spectra, the Ti³⁺ or Ti²⁺ peaks still can be observed after the photocatalytic reaction, indicating that H₂ production is not the result of reducing water by oxidizing Ti³⁺ or Ti²⁺ to Ti⁴⁺.

3.3.4.3 In 3d Core Level

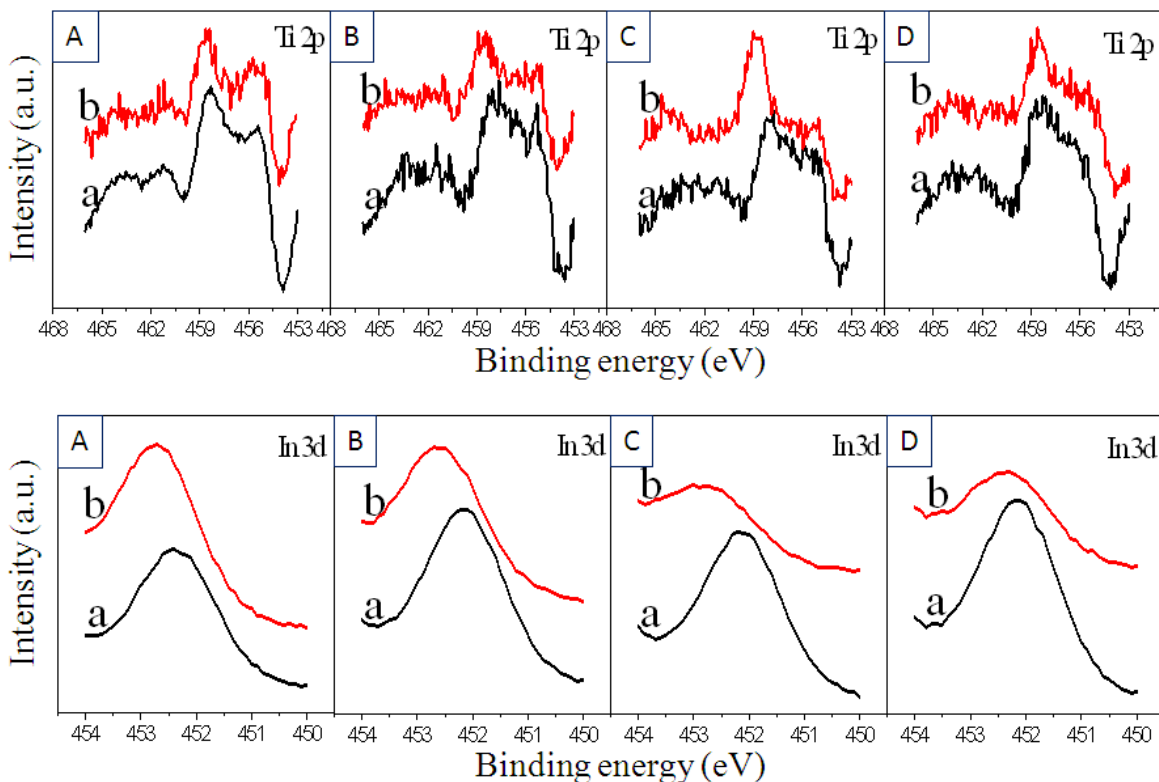
As shown in Figure 3.10B, The In core spin orbit split to the 3d_{5/2} peak at 444.5 eV. These results are close to the reported values for bulk InN (444.3 eV).^{9, 16} Therefore, XPS further confirms the formation of InN.

Regarding the XPS spectra after photocatalytic reaction, In 3d_{3/2} XPS spectra (Figure 3.11) show loss of intensity for low ammonolysis temperature samples, which suggests that the

lower temperatures yield less stable nitrides. But if the ammonolysis temperature exceeds 850°C, most of the In was sublimed and lost, and only TiN remained. The resulting sample had poor H₂ production activity. Therefore, a suitable ammonolysis temperature is very important, which has to be high enough to allow N doping, but not too high to further reduce In³⁺ into In metal. All In 3d_{3/2} XPS spectra (Figure 3.11) show the shifting to higher BE after the reaction, which indicates that some of the doped nitrogen was replaced by oxygen.



3.10 XPS spectra of samples obtained by nitriding a mixture of TiO₂ and In₂O₃ at different ammonolysis temperatures (a) 850 °C (b) 800 °C (c) 750 °C (d) 700 °C for 20 hours under a 250 mL/ min flow rate of NH₃.



3.11 XPS spectra of (a) before (b) after hydrogen production from water reaction under UV-vis light for a nitrated mixture of TiO_2 and In_2O_3 at different ammonolysis temperatures (A) 850 °C (B) 800 °C (C) 750 °C (D) 700 °C for 20 hours under a 250 mL/min flow rate of NH_3 .

3.3.4.4 O 1s Core Level

Figure 3.10C shows that the O 1s core level is composed of at least three components. The peak positions and intensities are reliably determined by a standard curve fitting procedure using XPSPEAKS software. The O 1s signal at 529.8 eV is assigned to In_2O_3 and TiO_2 according to the literature,¹⁷ while the signal at 530.8 eV is probably due to oxygen in surface adsorbed hydroxyl groups¹⁸ and the signal at 532.1 eV is from the surface adsorbed H_2O . Low ammonolysis temperature samples show a small shift to lower energy (529.0 eV) for the O 1s peak that is assigned to In_2O_3 and TiO_2 . This shift is similar to results found for substitutional

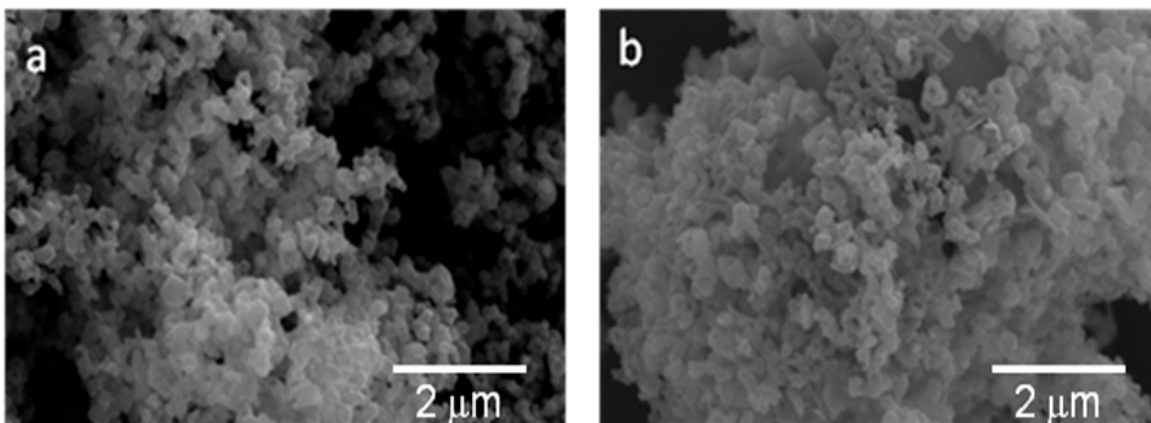
N-doped TiO₂ samples, in which the P25 TiO₂ sample shows an O 1s peak at 530.8 eV, versus a shift to 530.0 eV that is observed for the nitrogen-doped TiO₂ samples.¹⁹

3.3.4.5 N 1s Core Level

The N 1s XPS spectrum in Figure 3.10D has two components: 396.9 eV and 396.2 eV. The N 1s XPS data confirms the N is substitutional instead of interstitial.^{6, 7, 20} The 396.9 eV peak could be assigned to Ti-N, and In-N is at 396.2 eV because Ti has a higher electronegativity than In. The XPS high-resolution spectra of N 1s show the 850 °C ammonolysis sample's peak at 396.7 eV with a slight shift to 396.1 eV for the 700 °C sample (Figure 3.10D). The difference of 0.6 eV between these two N 1s peaks correlates with InN formation for the N 1s state in substitutional sites. Therefore, the data (Figure 3.10D) shows more formation of N in substitutional sites under higher ammonolysis temperature conditions.

3.3.5 Scanning Electron Microscopy

Figure 3.12 shows the SEM images of the catalyst before and after H₂ production reaction for comparison. After the loss of In, the overall morphology did not change much. Therefore, the morphology is not the major factor that affects H₂ production efficiency.



3.12 SEM images of synthesis Ti : In= 2 : 1, 800 °C ammonolysis 15 hours (a) before UV-vis irradiation at 15K magnification (b) after UV-vis irradiation at 15K magnification.

Brunauer, Emmett, Teller (BET) surface area

The texture of the solid-state material can be characterized by porosity, surface area, pore volume and pore size. Porous materials can have different formations such as cavities, channels or interstices. These pores have open and closed conditions. And open pores can have different shapes including cylindrical, blind with one open end, inkbottle and funnel.

Porosity is the total volume compared to the apparent volume of the particles in the powder. Pore volume is the volume of the pores in the investigated material. Pore size or pore diameter is the distance between two opposite walls of the pore.

Pore size is an important factor for catalyst materials. The pore character depends on different regions of the pores size: microporous (pore diameter < 2 nm), mesoporous (2 nm < pore diameter < 50 nm) and macroporous (pore diameter > 50 nm). The study of gas adsorption can characterize the porosity.

Gas adsorption on the surface of the subject material can yield information on specific surface area, total pore volume, and pore's size distribution. The pressure of the gas controls the surface coverage since the free and absorbed gases are in dynamic equilibrium. The fractional

surface coverage at different pressures and a set of temperature can give adsorption isotherms. Therefore, surface area and porosity can be calculated by mathematical analysis of the adsorption isothermal data. Nitrogen is a common gas used as the adsorbate since its intermediate value of C constant (50-250) and allows calculating the cross-sectional area of and adsorbate.

The Branauer-Emmet-Teller equation 3.4 is used to determine the surface area of the material.²¹

$$\frac{1}{W\left(\frac{P}{P_o}-1\right)} = \frac{1}{W_m C} + \frac{C-1}{W_m C} \left(\frac{P}{P_o}\right) \quad (3.4)$$

W is the weight of the absorbed gas at relative pressure P/P_o, C is a constant related to the energy of adsorption in the first adsorbed layer, and W_m is the weight of a monolayer of adsorbate. The total surface of the sample can be calculated by equation 3.5.

$$S_t = \frac{W_m N A_{cs}}{M} \quad (3.5)$$

N is an Avogadro's number (6.023×10^{23} molecules/mol) and M is a molecular weight of the adsorbate, and A_{cs} is a cross-sectional area (16.2 Å at 77 K).

The specific surface area can be calculated from the total surface area and the weight of the sample in equation 3.6.

$$S = \frac{S_t}{w} \quad (3.6)$$

The total pore volume can be calculated from the amount of gas adsorbed at relative pressure close to unity. And the pore size distribution can be calculated from the desorption branch of the isotherm by the Kelvin equation shown in equation 3.7.

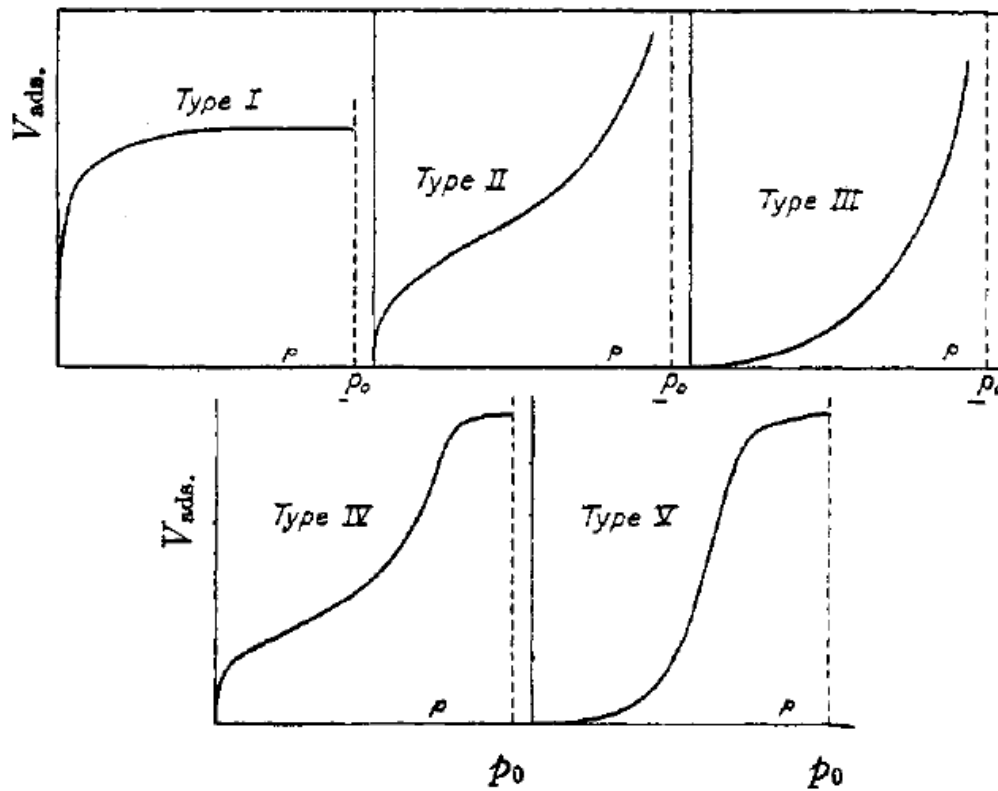
$$R_K = \frac{-2\gamma V_m}{RT \ln\left(\frac{P}{P_o}\right)} \quad (3.7)$$

Here, γ is a surface tension of nitrogen at the boiling point (8.85 ergs/cm² at 77 K), V_m is the molar volume of liquid nitrogen (34.6 cm³/mol), R is a gas constant (8.314×10^7 ergs/deg

mol), T is a boiling point of nitrogen (77 K), P/P_0 is a relative pressure of nitrogen and R_K is Kelvin radius of the pore.

Surface information such as area and porosity can be obtained by analyzing gas adsorption of the material. Through the introduction of a known gas volume (such as nitrogen), then measuring the equilibrium pressure, can yield adsorption isothermal data, which is obtained by measuring the quantities of released gas from the sample at a relative low pressure.

All isotherms may be divided into five types (figure 3.13) based on the ways how the nitrogen is adsorbed.²²



3.13 Five types of adsorption isotherms.²²

Type I isotherm is attributed to microporous materials which adsorb nitrogen on the external surface, and limited accessibility to the porous structure. Type II isotherm is found for

nonporous or macroporous materials which can absorb multilayers of nitrogen. Type III isotherm shows which materials have less heat of adsorption than the heat of adsorbate liquefaction, with an additional adsorption that interacts with the adsorbed layers. Type IV isotherm represents mesoporous materials with the mesopores filled by higher elevated pressures. Type V isotherm is similar to the type III but more common for mesoporous materials.

The adsorption and desorption branches in type I, II and III isotherms are the same and only rarely show hysteresis. But Type IV and V isotherms have hysteresis effects between adsorption and desorption. Most of the time, it is caused by bottleneck shape of pores materials and differences in the meniscus of the condensing and evaporation nitrogen.^{23, 24}

The surface area increased from 12.4 to 22 m²/g, when ammonolysis temperature increased from 700 to 800 °C, but decreased at 850 °C (Table 3.2, page 26). Another interesting finding was that the surface area of the Ti-In (oxy)nitride (800 °C, ammonolysis 15 hours) increased substantially, from 42 m²/g at the start of the UV experiment, to 98 m²/g after reaction (and loss of activity). This change in surface area/ unit mass could be due to the loss of some Indium, as substantiated by elemental analysis results, and the formation of additional pores.

3.4 Conclusions

A novel Ti-In (oxy)nitride was prepared by nitridation of TiO₂ and In₂O₃ under an NH₃ flow of 250 mL·min⁻¹. This preparation of (oxy)nitride provides a new strategy to synthesize InN at high temperature (> 700 °C). And Ti⁴⁺ could be reduced to 3+ and 2+ upon ammonia treatment with In₂O₃ presence. The change in the product with nitridation temperature was examined, and it was revealed that an active mixed nitride/oxide phase formed above 700 °C of nitridation. However, temperature above 900 °C caused Indium metal to form, which is volatile

at 900 °C and was lost, resulting in mainly TiN formation, and no hydrogen evolution activity. The XRD and XPS spectra confirmed that the prepared powders had nitrogen substituted at some of the oxygen sites in the TiO₂ and In₂O₃. The maximum UV-Visible diffuse reflectance spectra absorbance varied with nitridation temperature from 700 °C to 850 °C, and the oxygen 2p and nitrogen 2p XPS spectra showed a different valance band structure.²⁵ The optimum preparation conditions for Ti-In (oxy)nitride in order to achieve high hydrogen evolution are thus considered to be nitridation at 850 °C under NH₃ flow at 250 mLmin⁻¹. The composite produced under these conditions minimizes Indium loss by reduction to Indium metal and subsequent volatilization, but some Indium is retained as InN that is stabilized in the structure, and is important in hydrogen production.

Use of these materials for reaction with water to form hydrogen revealed that: (1) in the absence of a sacrificial agent to soak up the holes of the electro-hole pair, the reaction was not catalytic, but instead a UV and visible light driven stoichiometric reaction took place that continued for hundreds of hours; (2) in the presence of a sacrificial agent (methanol) the reaction did become photocatalytic and continued for hundreds of hours producing hydrogen under visible light irradiation at a constant rate.

References

1. Osterloh, F. E., Inorganic Materials as Catalysts for Photochemical Splitting of Water. *Chemistry of Materials* **2007**, 20, (1), 35-54.
2. Kato, H.; Asakura, K.; Kudo, A., Highly Efficient Water Splitting into H₂ and O₂ over Lanthanum-Doped NaTaO₃ Photocatalysts with High Crystallinity and Surface Nanostructure. *Journal of the American Chemical Society* **2003**, 125, (10), 3082-3089.
3. G. Kim, H.; W. Hwang, D.; Kim, J.; G. Kim, Y.; S. Lee, J., Highly donor-doped (110) layered perovskite materials as novel photocatalysts for overall water splitting. *Chemical Communications* **1999**, (12), 1077-1078.
4. Sato, J.; Saito, N.; Yamada, Y.; Maeda, K.; Takata, T.; Kondo, J. N.; Hara, M.; Kobayashi, H.; Domen, K.; Inoue, Y., RuO₂-Loaded β-Ge₃N₄ as a Non-Oxide Photocatalyst for Overall Water Splitting. *Journal of the American Chemical Society* **2005**, 127, (12), 4150-4151.
5. Maeda, K.; Takata, T.; Hara, M.; Saito, N.; Inoue, Y.; Kobayashi, H.; Domen, K., GaN:ZnO Solid Solution as a Photocatalyst for Visible-Light-Driven Overall Water Splitting. *Journal of the American Chemical Society* **2005**, 127, (23), 8286-8287.
6. Irie, H.; Watanabe, Y.; Hashimoto, K., Nitrogen-concentration dependence on photocatalytic activity of TiO_{2-x}N_x powders. *Journal of Physical Chemistry B* **2003**, 107, (23), 5483-5486.
7. Asahi, R.; Morikawa, T.; Ohwaki, T.; Aoki, K.; Taga, Y., Visible-light photocatalysis in nitrogen-doped titanium oxides. *Science* **2001**, 293, (5528), 269-271.
8. Poznyak, S. K.; Talapin, D. V.; Kulak, A. I., Structural, Optical, and Photoelectrochemical Properties of Nanocrystalline TiO₂-In₂O₃ Composite Solids and Films Prepared by Sol-Gel Method. *The Journal of Physical Chemistry B* **2001**, 105, (21), 4816-4823.
9. Reyes-Gil, K. R.; Reyes-Garcia, E. A.; Raftery, D., Nitrogen-doped In₂O₃ thin film electrodes for photocatalytic water splitting. *Journal of Physical Chemistry C* **2007**, 111, (39), 14579-14588.
10. Schwenzer, B.; Loeffler, L.; Seshadri, R.; Keller, S.; Lange, F. F.; DenBaars, S. P.; Mishra, U. K., Preparation of indium nitride micro- and nanostructures by ammonolysis of indium oxide. *Journal of Materials Chemistry* **2004**, 14, (4), 637-641.
11. Trainor, J.; Rose, K., Some properties of inn films prepared by reactive evaporation. *Journal of Electronic Materials* **1974**, 3, (4), 821-828.

12. Guo, Q.; Kato, O.; Yoshida, A., Thermal stability of indium nitride single crystal films. *Journal of Applied Physics* **1993**, 73, (11), 7969-7971.
13. Abe, R.; Sayama, K.; Sugihara, H., Development of New Photocatalytic Water Splitting into H₂ and O₂ using Two Different Semiconductor Photocatalysts and a Shuttle Redox Mediator IO₃⁻/I⁻. *The Journal of Physical Chemistry B* **2005**, 109, (33), 16052-16061.
14. Kudo, A.; Miseki, Y., Heterogeneous photocatalyst materials for water splitting. *Chemical Society Reviews* **2009**, 38, (1), 253-278.
15. Idriss, H.; Pierce, K. G.; Barteau, M. A., Synthesis of Stilbene from Benzaldehyde by Reductive Coupling on TiO₂(001) Surfaces. *Journal of the American Chemical Society* **1994**, 116, (7), 3063-3074.
16. Maruyama, T.; Yorozu, K.; Noguchi, T.; Seki, Y.; Saito, Y.; Araki, T.; Nanishi, Y., Surface treatment of GaN and InN using (NH₄)₂S_x. *physica status solidi (c)* **2003**, 0, (7), 2031-2034.
17. Donley, C.; Dunphy, D.; Paine, D.; Carter, C.; Nebesny, K.; Lee, P.; Alloway, D.; Armstrong, N. R., Characterization of indium-tin oxide interfaces using X-ray photoelectron spectroscopy and redox processes of a chemisorbed probe molecule: Effect of surface pretreatment conditions. *Langmuir* **2002**, 18, (2), 450-457.
18. Asai, N.; Inoue, Y.; Sugimura, H.; Takai, O., Electrochromic Reaction of InN Thin Films. *Journal of The Electrochemical Society* **1999**, 146, (6), 2365-2369.
19. Chen, X.; Burda, C., Photoelectron Spectroscopic Investigation of Nitrogen-Doped Titania Nanoparticles. *The Journal of Physical Chemistry B* **2004**, 108, (40), 15446-15449.
20. Sano, T.; Negishi, N.; Koike, K.; Takeuchi, K.; Matsuzawa, S., Preparation of a visible light-responsive photocatalyst from a complex of Ti⁴⁺ with a nitrogen-containing ligand. *Journal of Materials Chemistry* **2004**, 14, (3), 380-384.
21. Brunauer, S.; Emmett, P. H.; Teller, E., Adsorption of Gases in Multimolecular Layers. *Journal of the American Chemical Society* **1938**, 60, (2), 309-319.
22. Brunauer, S.; Deming, L. S.; Deming, W. E.; Teller, E., On a Theory of the van der Waals Adsorption of Gases. *Journal of the American Chemical Society* **1940**, 62, (7), 1723-1732.
23. McBain, J. W., An Explanation of Hysteresis in the Hydration and Dehydration of Gels. *Journal of the American Chemical Society* **1935**, 57, (4), 699-700.
24. Cohan, L. H., Sorption Hysteresis and the Vapor Pressure of Concave Surfaces. *Journal of the American Chemical Society* **1938**, 60, (2), 433-435.

25. Maeda, K.; Teramura, K.; Takata, T.; Hara, M.; Saito, N.; Toda, K.; Inoue, Y.; Kobayashi, H.; Domen, K., Overall Water Splitting on $(\text{Ga}_{1-x}\text{Zn}_x)(\text{N}_{1-x}\text{O}_x)$ Solid Solution Photocatalyst: Relationship between Physical Properties and Photocatalytic Activity. *The Journal of Physical Chemistry B* **2005**, 109, (43), 20504-20510.

Chapter 4 - Hydrogen from ethanol solution under UV-visible light. Photocatalysts produced by Nitriding Titanium nitride and Indium oxide Intimate mixtures to Form Ti-In nitride composites

Photocatalytic production of hydrogen gas from 20 % ethanol-water was accomplished with Ti-In nitride composites. These materials were produced by nitriding a TiO_2 with ammonia at a high temperature, then adding In_2O_3 and further ammonolysis for different periods of time. The catalysts were very stable and continued to produce H_2 gas at $920 \mu\text{mole}\cdot\text{h}^{-1}\cdot\text{g}^{-1}$ for 50 hours and accumulated 12.8 mmole H_2 gas. The water splitting photocatalytic reaction can be driven by UV-vis light, maximum producing H_2 gas at $1277 \mu\text{mole}^{-1}\cdot\text{g}^{-1}$. It is critical that we understand how having high, stable activity is possible. We used XPS, X-ray (XRD), UV-Vis diffuse reflectance spectrometry, and BET surface area and pore size distribution for further characterization.

4.1 Introduction

Titanium Dioxide is a well known photocatalyst^{1, 2} but absorbs only in the ultraviolet region for photochemical reactions. In order to extend the utilization of solar energy; many approaches aim to modify the TiO_2 to enhance visible light application. One way is to substitute Cr, Fe or Ni for Ti.^{3, 4} Such substitution could improve TiO_2 absorption into the visible light region ($> 450 \text{ nm}$) and those catalysts demonstrated photocatalytic activity to decompose NO into N_2 , O_2 and N_2O .⁴ Another approach is to create Ti^{3+} sites by introducing oxygen vacancies in TiO_2 .⁵ And it is also reported that by doping NH_4Cl or NH_4OH into TiO_2 , the TiO_2 can be sensitive to visible light.⁶ Moreover, Hashimoto has reported a nitrogen-doped TiO_2 by

annealing anatase TiO₂ powder under NH₃ flow at different temperatures.⁷ It was confirmed that nitrogen substituted at some of the oxygen sites in TiO₂, formed a narrow N 2p band above the valance band, and the narrow N 2p band was responsible for visible light absorption.

Indium nitride (InN) has a low band gap (0.7 eV) and recently has become the focus of intense research.^{8,9} The methods of synthesis have included molecular-beam epitaxy (MBE)^{8,10} and metal organic chemical vapor deposition (MOCVD).¹¹ The decomposition temperatures reported for InN range from ~500 °C for thin films⁵ to ~710 °C.⁶ Therefore, InN is easily decomposed and is more difficult to fabricate into nanoparticles and nanowires than aluminum nitride (AlN)^{12,13} or gallium nitride (GaN).¹⁴ However, recently it was shown that InN could be prepared by nitriding In₂O₃ at different temperatures.¹⁵ In the work reported herein, we have prepared samples combined TiN-InN by an in-situ synthesis, and have investigated their behavior in photocatalytic water splitting in the present of a sacrificial agent, ethanol.

4.2 Experimental Section

4.2.1 Preparation of TiN/InN composites

TiN-In nitride composites powders were prepared by annealing a mixture of 0.92 g anatase TiO₂ powder (1.15×10^{-2} moles) (Sigma-Aldrich, anatase, nanopowder, <25nm, 99.7%) at 750 °C under NH₃ flow (250 mL/min) for 13 or 18 hours and marked as TiN (13 h) and TiN (18 h) in this paper. Then the product was mixed with 3.2 g In₂O₃ powder (1.15×10^{-2} moles) (Sigma-Aldrich, nanopowder, <100nm, 99.9%) in the 20 mL water solution and sonicated for more than 90 minutes until completely dried (TiN/In₂O₃ mixture). Mixtures were further annealed again at 750 °C under NH₃ flow (250 mL/min) for 1 to 5 hours. The mole ratio of Ti to

In the starting material (TiO₂ and In₂O₃) was 1/1. In all of the ammonolysis procedures, the samples were finally cooled to room temperature under NH₃ flow.

4.2.2 Characterization of Catalysts

The prepared samples were studied by powder X-ray diffraction (XRD; Bruker D8 X-ray diffractometer with Cu K α radiation), scanning electron microscopy (SEM; Hitachi S-3500 N), UV-visible diffuse reflectance spectroscopy (DRS; Varian Cary 500 Scan). The Brunauer, Emmett, Teller (BET) surface areas were measured with a Quantachrome NOVA-1200 instrument at liquid nitrogen temperature. X-ray photoelectron spectroscopy (XPS); a SPECS Sage100 spectrometer was used operating in the fixed analyzer transmission mode using achromatic Mg K α (1253.6 eV) radiation at 240 W (12 kV and 20 mA) using a water-cooled X-ray gun cap and evacuated with turbomolecular pumping. The base pressure of the chamber was about 2×10^{-8} Torr, and the energy scales were calibrated using copper and the separation between photoelectron peaks generated by Mg and Al K α X-rays. Survey spectra were collected with a pass energy of 30 eV; a pass energy of 15 eV was used for both core and valence band spectra. Many of the spectra were calibrated by taking the C 1s peak due to residual hydrocarbon as being at 284.4 eV.

4.2.3 Photocatalytic Reactions

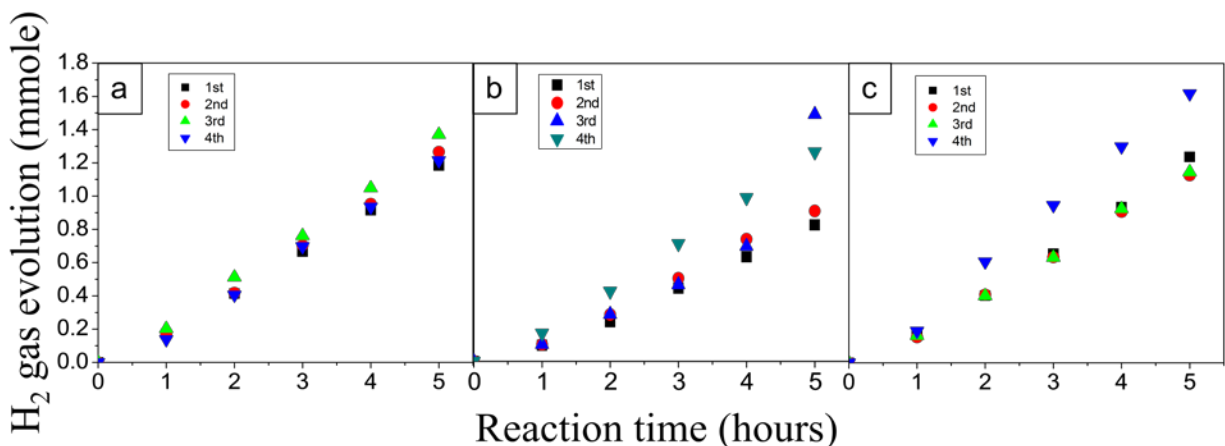
The reactions were carried out in a glass-enclosed reaction chamber connected to a gas circulation and evacuation system with a quartz inner irradiation-type reaction vessel. The reaction was performed in a 345 ml 20 % ethanol solution and containing 0.3 g of the composite catalyst sample. The reactant solution was evacuated and filled with argon 3 times to remove air completely, followed by irradiation under a 450 W high-pressure Hg lamp. H₂ production was

monitored during the reaction with an online GC system (GOMAC model) employing a Supelco molecular 80/100 sieve 5A column with Ar as the carrier gas and a thermal conductivity detector (TCD).

4.3 Results and Discussion

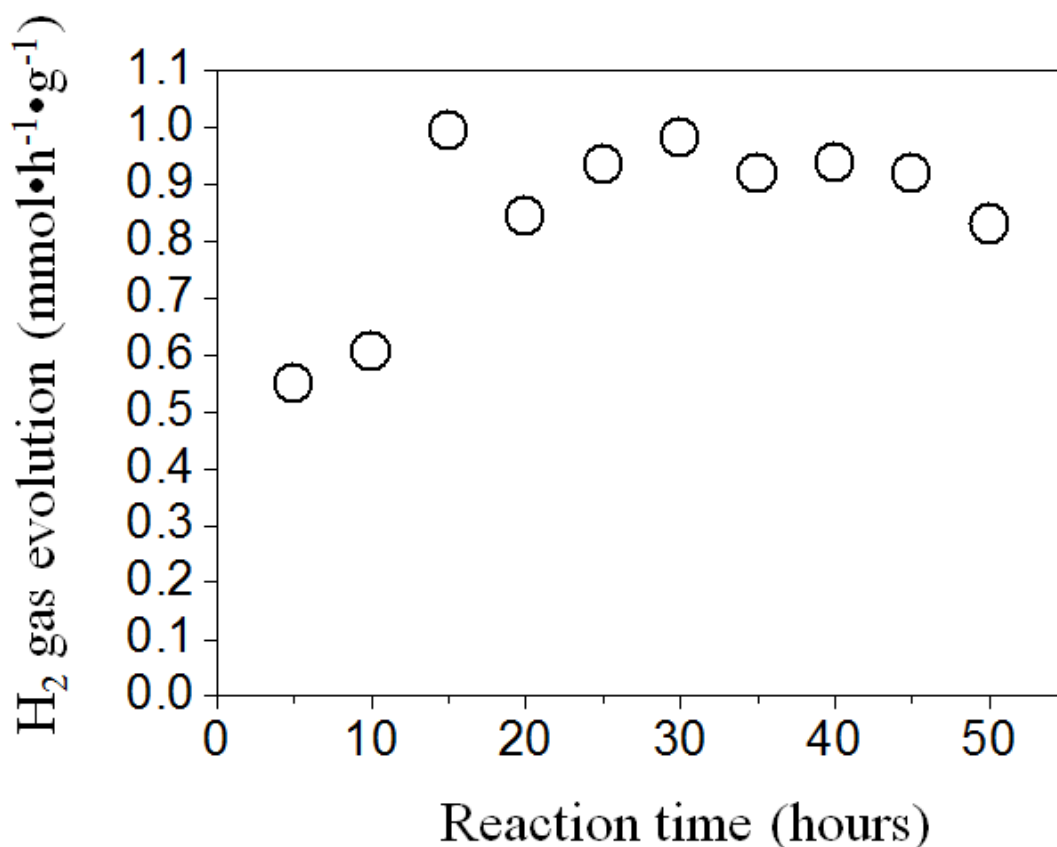
4.3.1 Dependence of Photocatalytic Activity on Ammonolysis time

Figure 4.1 shows the water splitting reactivity results of the photocatalysis in 20% ethanol solution under UV-vis light. Nitridation of the TiN/In₂O₃ sample for one hour produced a catalyst with very good stability for producing H₂ gas at 839 $\mu\text{mol} \cdot \text{h}^{-1} \cdot \text{g}^{-1}$. As the nitridation time increased to 3 h, the sample was less stable. Interestingly, the water splitting activity increased with time, and leveled off at about 920 to 950 $\mu\text{mol} \cdot \text{h}^{-1} \cdot \text{g}^{-1}$ in trail after trial of different samples made under the same conditions. This was also true of the 5 h sample. Indeed, after the fourth trial a steady activity of 1080 $\mu\text{mol} \cdot \text{h}^{-1} \cdot \text{g}^{-1}$ was achieved and remained stable for more than 50 h of reaction (figure 4.2). The total amount of H₂ gas evolved over 50 h under UV-Visible irradiation of the nitridation 3 h sample was 12.8 mmole, much greater than the amount of catalyst employed; hence, proving that the H₂ gas generation is not a stoichiometric reaction. In order to compare the activity without adding In₂O₃, figure 4.3 shows the photoactivity of TiN (18 h). Every 5 hours water splitting reaction time, the glass-enclosed system was evacuated and refilled with the argon gas, then restarted using by the same sample. The sample was tested for 15 hours, and did not have a very good performance and was quite unstable.



4.1 Dependence of photocatalytic activity of mixture of TiN (13 h)/In₂O₃ at different ammonolysis time for (a) 1 (b) 3 (c) 5 h at 750 °C under a 250 mL/ min flow rate of NH₃. Catalyst (0.3g), a 20 % ethanol aqueous solution, high-pressure mercury lamp (450 W); inner irradiation-type reaction vessel.

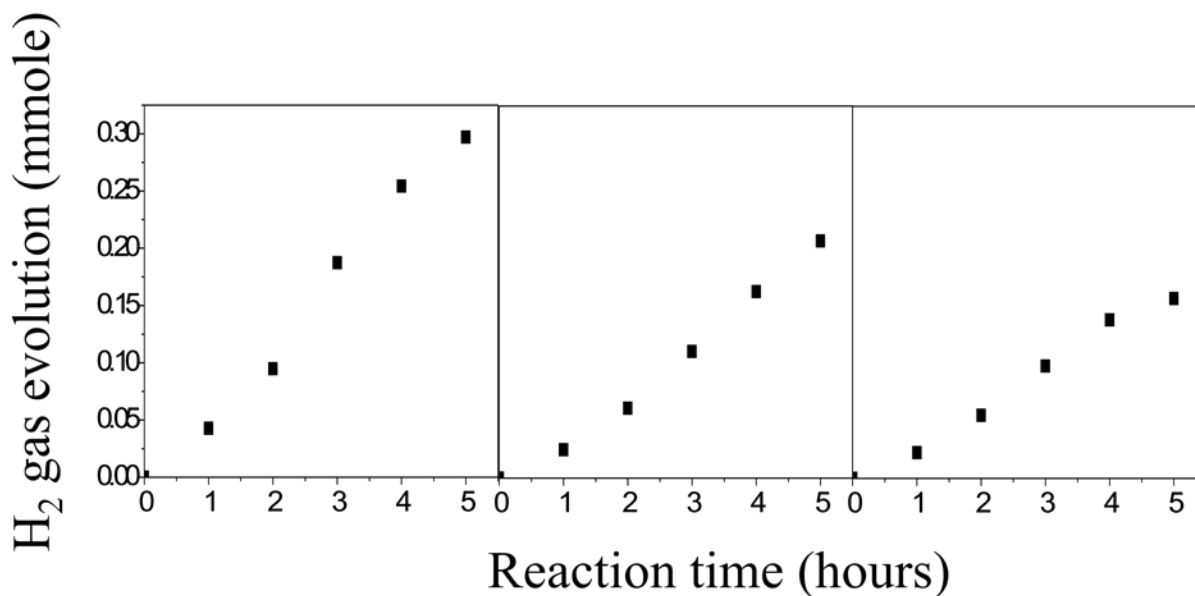
A series of TiN samples prepared by 18 h nitridation were compared after addition of In₂O₃ and further nitridation (table 4.1 and figure 4.3). The water splitting efficiencies reveal that the combination of TiN and In₂O₃ not only improved catalyst activity dramatically, but also increased stability. Figure 4.4 shows the photocatalysis activity of TiN (18 h)-In nitride ammonolysis for 3 h. The sample was examined for 20 hours by repeated evacuation and refilling every 5 hours. The data demonstrate higher catalyst performance than others, and reached as high as $1277 \mu\text{mol} \cdot \text{h}^{-1} \cdot \text{g}^{-1}$, the H₂ gas evolution was stable and reproducible. The better efficiency was perhaps caused by the better crystallization based on the XRD (figure 4.6a). A high degree of crystallinity is often required, and sometimes more important than a high surface area (Table 4.1) for water splitting.¹⁶



4.2 Dependence of photocatalytic activity of mixture of TiN (13 h)/In₂O₃ further ammonolysis for 3 h at 750 °C under a 250 mL/ min flow rate of NH₃. Catalyst (0.3g), a 20 % ethanol aqueous solution, high-pressure mercury lamp (450 W); inner irradiation-type reaction vessel.

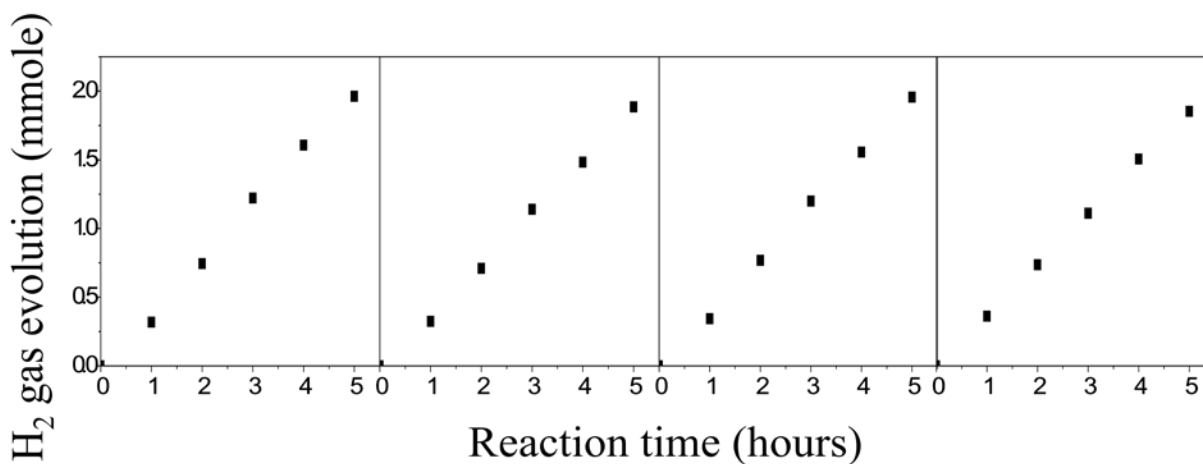
4.1 BET and Photocatalytic activities of TiN/In₂O₃ with various nitridation times under UV -Visible irradiation in 20 % ethanol solution

Catalyst	Nitridation time (hours)	H ₂ gas evolution photocatalytic activity (μmol · h ⁻¹ · g ⁻¹)	Surface Area (m ² /g)
TiN (18 h)	18	147	
TiN(13 h)-In nitride	1	839	2.0
TiN(13 h)-In nitride	3	749	2.4
TiN(13 h)-In nitride	5	855	4.5
TiN(18 h)-In nitride	3	1277	4.6



4.3 Dependence of photocatalytic activity of TiO₂ nitridation 18 h under a 250 mL/ min flow rate of NH₃. Catalyst (0.3g), a 20 % ethanol aqueous solution, high-pressure mercury lamp (450 W); inner irradiation-type reaction vessel.

***Every 5 hours water splitting reaction time, the glass-enclosed system was evacuated and refilled with the argon gas, then restarted using by the same sample. The procedures were repeated for 3 times.**

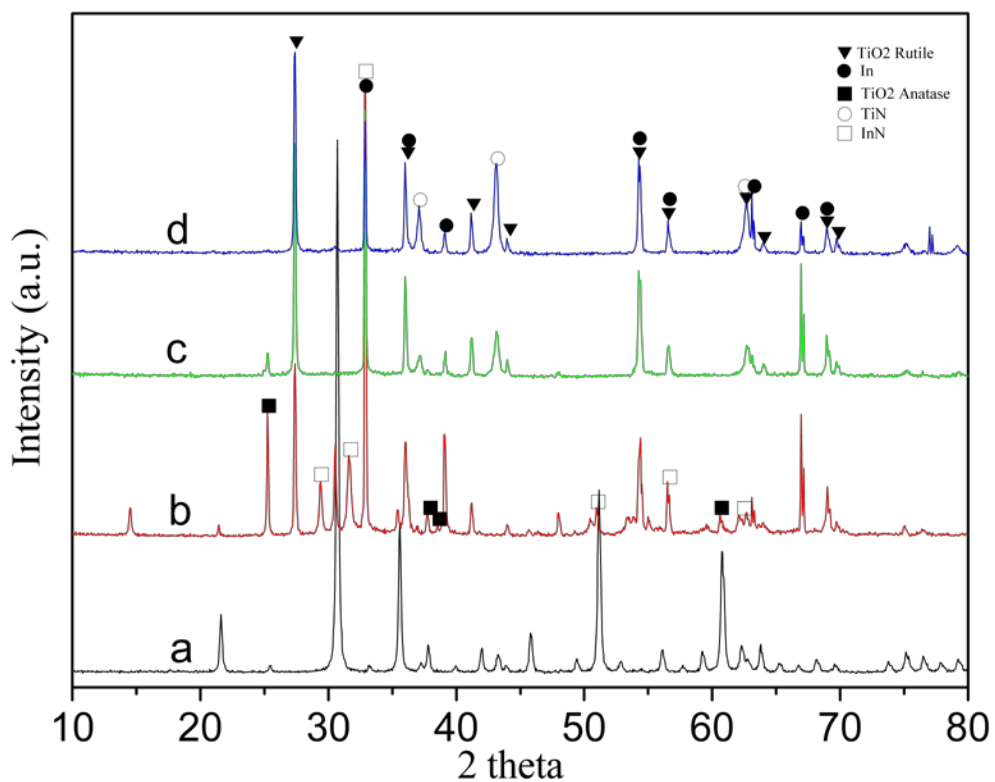


4.4 Dependence of photocatalytic activity of nitridation TiN (18 h)/In₂O₃ 3 h at 750 °C under a 250 mL/ min flow rate of NH₃. Catalyst (0.3g), a 20 % ethanol aqueous solution, high-pressure mercury lamp (450 W); inner irradiation-type reaction vessel.

4.3.2 Crystal Structure

Figure 4.5 shows XRD patterns from samples obtained by nitriding a mixture of TiN (13 h)/In₂O₃ at several nitridation times. TiN (13 h)/In₂O₃ is shown for comparison. The major pattern of the TiN (13 h)/In₂O₃ mixture is the In₂O₃ phase with TiO₂ anatase phase as a residue. However, after nitridation for 1 hour, a sample with multiple phases resulted in a diffraction pattern, showing TiN, InN, TiO₂ anatase and rutile phases. There were no other oxygen sources available during the nitridation process. Hence, these results suggest that oxygen exchange between TiN and In₂O₃ occurred.

The crystal structures of samples are summarized in table 2. Moreover, it is known that In₂O₃ is reduced to metallic Indium upon ammonolysis of Indium oxide by anhydrous ammonia above 650 °C.¹⁸ Decomposition temperatures reported for InN range from 500 °C for thin films¹⁷,¹⁸ to 710 °C. Wet chemical synthesis of InN fibers¹⁹ and InN nanocrystals²⁰ by a low-temperature method have been reported. The formation of InN more likely proceeds via a vapor–solid (VS) mechanism,²¹ if more than 700 °C is employed as a synthesis temperature. However, in this research, even when the ammonolysis temperature was 750 °C, InN formed and was also stable, when TiO₂ was also present as a coreactant. As the nitridation time of TiN/In₂O₃ was increased from 1 to 3 h, the TiO₂ anatase phase was lowered with complete disappearance of InN, TiN and In₂O₃. However, the TiN phase became more prominent, indicating the possible further reduction of TiO₂. After the nitridation time increased to 5 h, the TiO₂ anatase phase disappeared totally, but the rutile phase remained. Figure 4.6 gives the idea of particle size, different crystal sizes of compounds and the ratio of compounds by schematic representation for the composite. Distribution number and crystal sizes are based on the XRD data (figure 4.5).

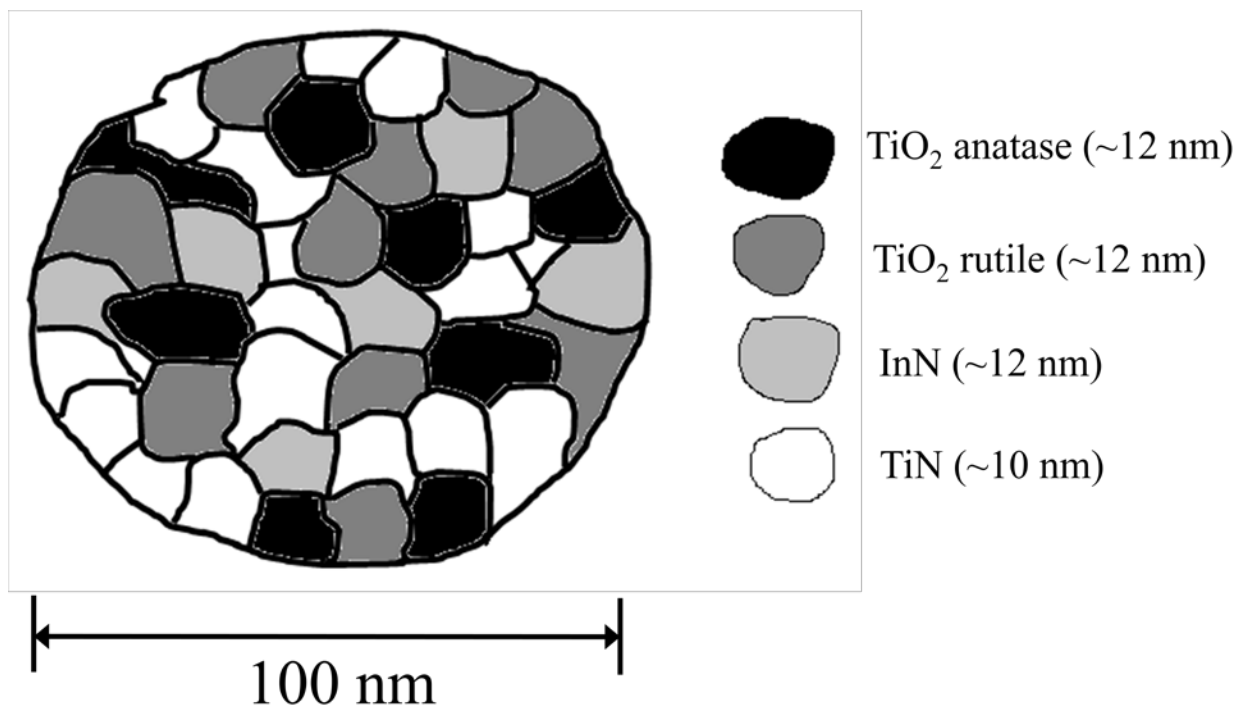


4.5 Powder XRD patterns of (a) TiN (13 h)/In₂O₃ mixture and different nitridation time of TiN (13 h)/In₂O₃ for (b) 1 (c) 3 (d) 5 h at 750 °C under a 250 mL/min flow rate of NH₃.

4.2 Diffraction Data Powder X-Ray

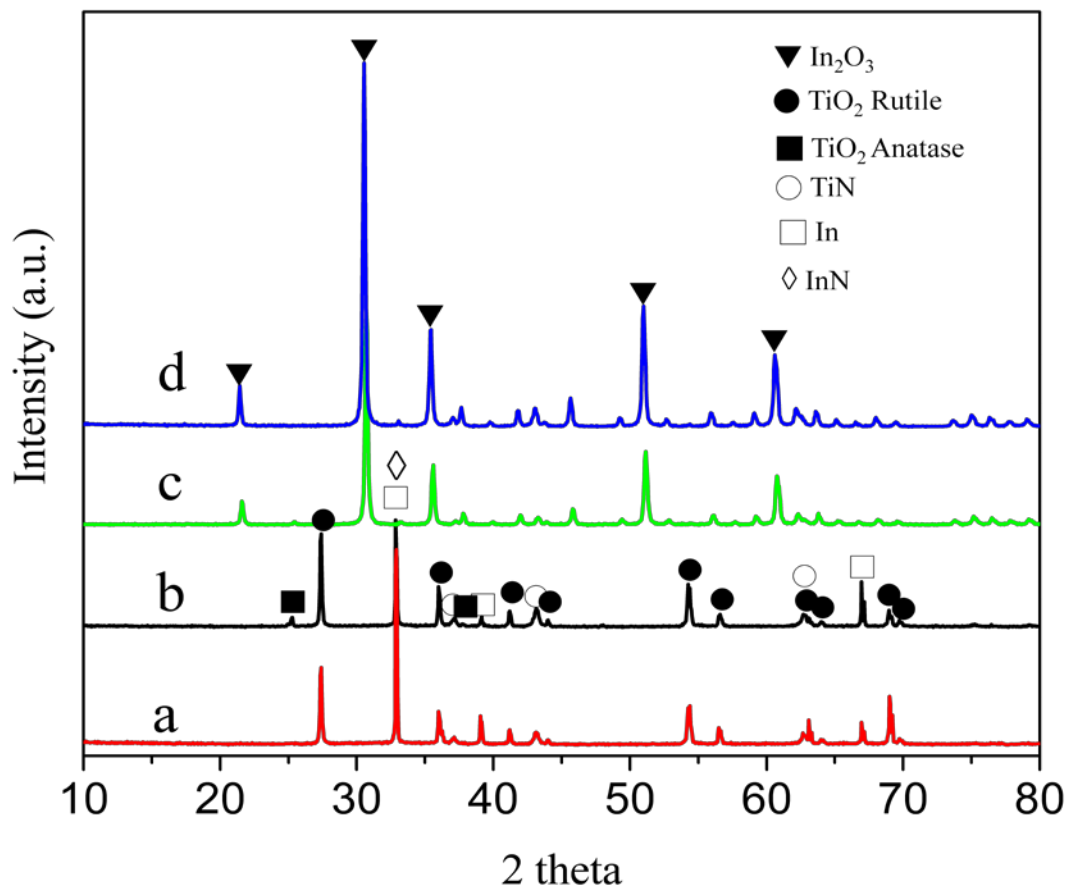
Catalyst	Nitridation Time (hours)	TiN	TiO ₂ (anatase)	TiO ₂ (rutile)	In ₂ O ₃	InN	In
TiN(13 h)-In nitride	0	No	Yes	No	Yes	No	No
TiN(13 h)-In nitride	1	No	Yes	Yes	No	Yes	Yes
TiN(13 h)-In nitride	3	Yes	Yes	Yes	No	Yes	Yes
TiN(13 h)-In nitride	5	Yes	No	Yes	No	Yes	Yes
TiN(18 h)-In nitride	3	Yes	No	Yes	No	Yes	Yes

Figure 4.7 shows XRD patterns of TiN (13 h)/In₂O₃, TiN (18 h)/In₂O₃, TiN (13 h)-In nitride and TiN (18 h)-In nitride. TiN(13 h)/In₂O₃ and TiN(18 h)/In₂O₃ are identical in patterns, with the In₂O₃ phase as major with TiO₂ anatase phase as minor. After further nitridation for 3 h the two nitride samples both show the arising of the TiO₂ rutile phase. However, TiN (13 h)-In nitride has more TiO₂ anatase phase, and TiN (18 h)-In nitride has more In and InN phases. The crystallization conditions of these two samples are different. The full width at half maximum (FWHM) of TiN (18 h)-In nitride is 0.2 degree, and TiN (13 h)-In nitride is 0.3 degree. This indicates that the nitridation time of TiO₂ can affect the interaction between TiN and In₂O₃, resulting in various crystal phase compositions.

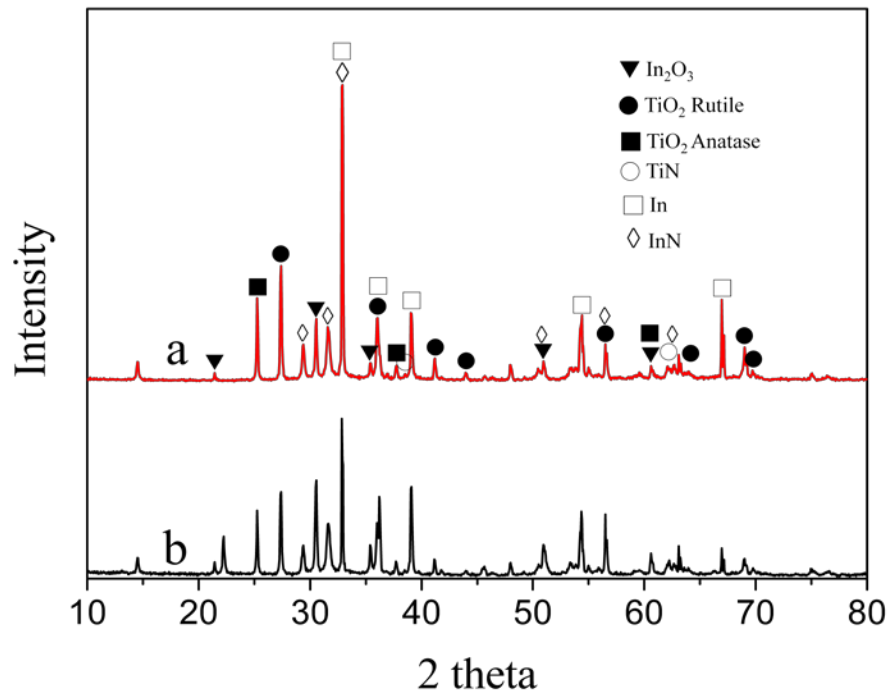


4.6 Schematic representation showing the particle size, different crystal sizes of compounds and the ratio of compounds for the composite. Distribution number and crystal sizes are based on the XRD data (figure 4.5).

Figure 4.8 shows the XRD patterns before and after water splitting reaction. The patterns are almost the same after 20 h of reaction time, indicating the stability of the catalyst.



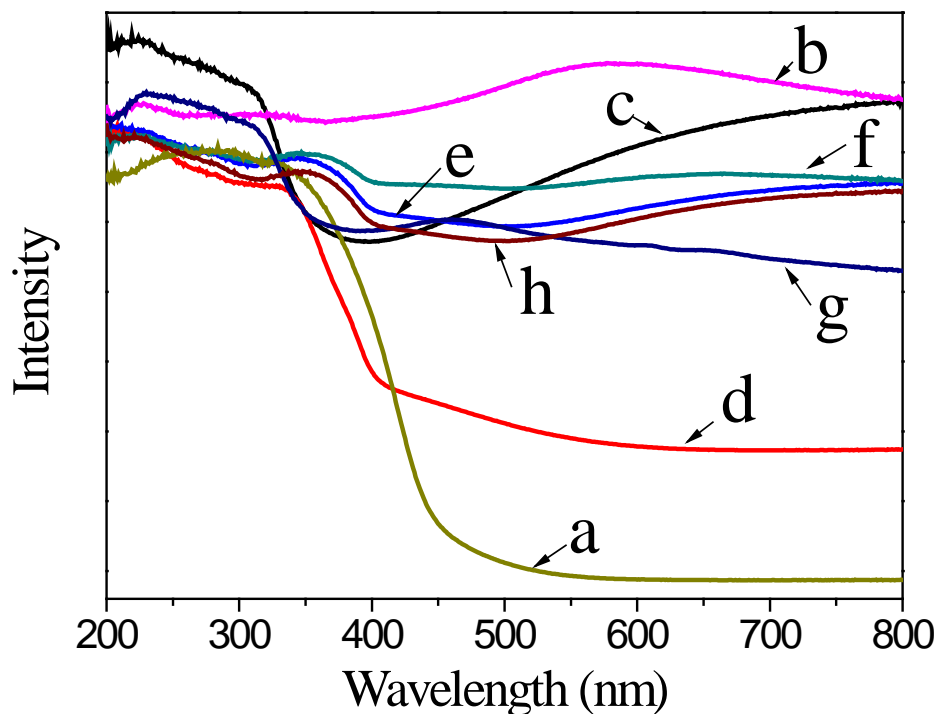
4.7 Powder XRD patterns of (a) TiN (18 h)-In nitride ammonolysis 3 h (b) TiN (13 h)-In nitride ammonolysis 3 h (c) TiN (13 h)/ In_2O_3 mixture (d) TiN (18 h)/ In_2O_3 mixture.



4.8 Powder XRD patterns of TiN (13 h)/In₂O₃ mixture nitridation 1 h at 750 °C under a 250 mL/min flow rate of NH₃ (a) before (b) after water splitting reaction.

4.3.3 UV-Visible Diffuse Reflectance Spectra

Figure 4.9 shows UV-Visible diffuse reflectance spectra of different TiN (13 h)-In nitride samples along with In₂O₃, TiN (13 h), TiN (18 h)/In₂O₃ mixture and TiN (13 h)/In₂O₃ mixture for comparison. In₂O₃ and TiO₂ are wide band gap materials with band gaps of 2.8 and 3.2 eV, respectively. As nitridation time increases from 1 to 5 hours, the absorption of visible light of each sample increased (>400 nm). The color of the specimens changed from gray to black by different nitridation time, also the absorption edge of each sample shifted slightly to longer wavelength (table 4.3), and exhibited a broad absorption extending well into the visible region.



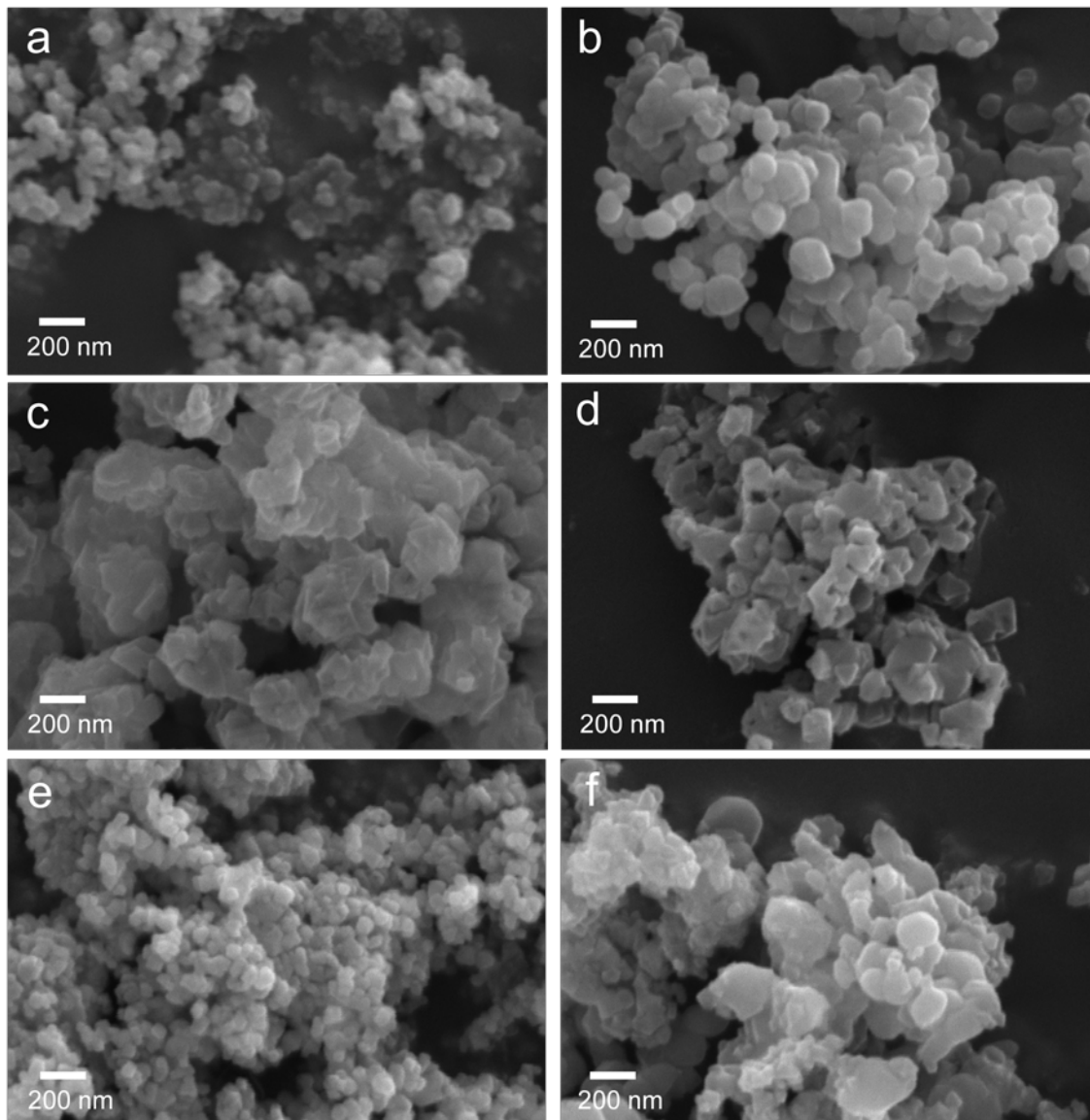
4.9 Diffuse reflectance spectra of (a) In_2O_3 (b) TiN (13 h) (c) TiN (13 h)/ In_2O_3 mixture and different nitridation time of TiN (13 h)-In nitride for (d) 1 (e) 3 (f) 5 h at 750 °C under a 250 mL/min flow rate of NH_3 . (g) TiN (18 h)/ In_2O_3 mixture (h) TiN (18 h)-In nitride for 3 h.

4.3 Characterization Data for various samples: UV-vis Absorption Spectra

Sample	Nitridation Time (hours)	Band Edge (eV)	Broad visible Absorption	Color
TiN (13 h)	13	2.1*	Yes	Black
TiN(13 h)-In nitride	0	3.5	Yes	Dark blue
TiN(13 h)-In nitride	1	3.1	No	Gray
TiN(13 h)-In nitride	3	3.0	Yes	Dark green
TiN(13 h)-In nitride	5	3.0	Yes	Black
TiN(18 h)-In nitride	3	3.1	Yes	Dark green
In_2O_3	0	2.8	No	Yellow
TiO_2	0	3.2	No	White

4.3.4 SEM Observations

The morphologies of the prepared samples were observed by SEM. Figure 4.10 shows SEM images of TiN (13 h)/In₂O₃ and TiN (18 h)/In₂O₃ mixtures and their further nitridation (various times) samples. The information of particle size and morphology are collected into table 4. Two of the samples have smaller size and spherical-like particles. After further nitridation for 1 h, the TiN (13 h)-In nitride particle size increased. As the nitridation time increased to 3 h and 5 h, the morphology changed and turned into a layered structure. Moreover, nitridation 5 h TiN (13 h)-In nitride yielded more cubic architecture with sharper edges, similar to the 3 h TiN (13 h)-In sample (figure 10c). The SEM revealed that mixing with In₂O₃ resulting in morphology change and size increase. But after mixing with In₂O₃ and ammonolysis for only 1 h, the morphology and size had changed. Therefore, the SEM images also show that the interaction between TiN and In₂O₃ causes a change in morphology.



4.10 SEM images of (a) TiN (13 h)/In₂O₃ mixture and different nitridation time of TiN (13 h)-In nitride for (b) 1 (c) 3 (d) 5 h at 750 °C under a 250 mL/min flow rate of NH₃. (e) TiN (18 h)/In₂O₃ mixture (f) TiN (18 h)-In nitride ammonolysis 3 h.

4.3.5 X-ray Photoelectron Spectra

We have examined four areas of the XPS spectra for several samples: the Ti 2p region (466-453 eV), In 3d region (450-454 eV), the O 1s region (525-537 eV), and the N 1s region (394-400 eV).

4.3.5.1 C 1s Core Level

The survey spectra of all the Ti-In nitride powders confirmed the presence of Ti, In, O, N and C. The binding energies (BEs) were calibrated using the C 1s energy of 284.4 eV as an internal calibration.

4.3.5.2 Ti 2p Core Level

The Ti 2p peak (figure 4.11A), 457.85 eV is in good agreement with the value reported in the literature for N-doped TiO₂.²² The XPS data shows that the ammonolysis process can cause the BE to shift to lower values with increased nitridation time. The XPS data are consistent with the XRD results. The Ti in TiN/In₂O₃ mixture had more N-doped in the beginning, after 1 h further nitridation of the mixture, the Ti scavenged oxygen from In₂O₃ as the TiO₂ anatase phase increased (as shown in the XRD pattern figure 4.5b); thus, the peak shifted to higher BE. As the nitridation time increased to 3 h, more N atoms were doped into the system. The peak shifted to lower BE again, when the nitridation time increased.

4.3.5.3 In 3d Core Level

As shown in figure 4.11B, the In 3d peak of the TiN(13 h)/In₂O₃ mixture appears at 451.5 eV, and is very similar to the value of commercial In₂O₃.²² And the longer ammonolysis time samples show a shift to a lower BE. This BE shift suggests a reduction of the In cation valence state. This situation has been seen in In bonding to oxygen in In₂O₃ that results in a higher BE than In bonding to nitrogen in InN.²³ This is also consistent for TiO₂ and substitutional N-doped TiO₂, in which the lower BE of the Ti 2p peak after nitrogen treatment can be attributed to nitrogen substitutional doping.^{24, 25} Therefore, we can conclude that this lower BE shift suggests that N-substitution modifies the electronic interaction of In with the

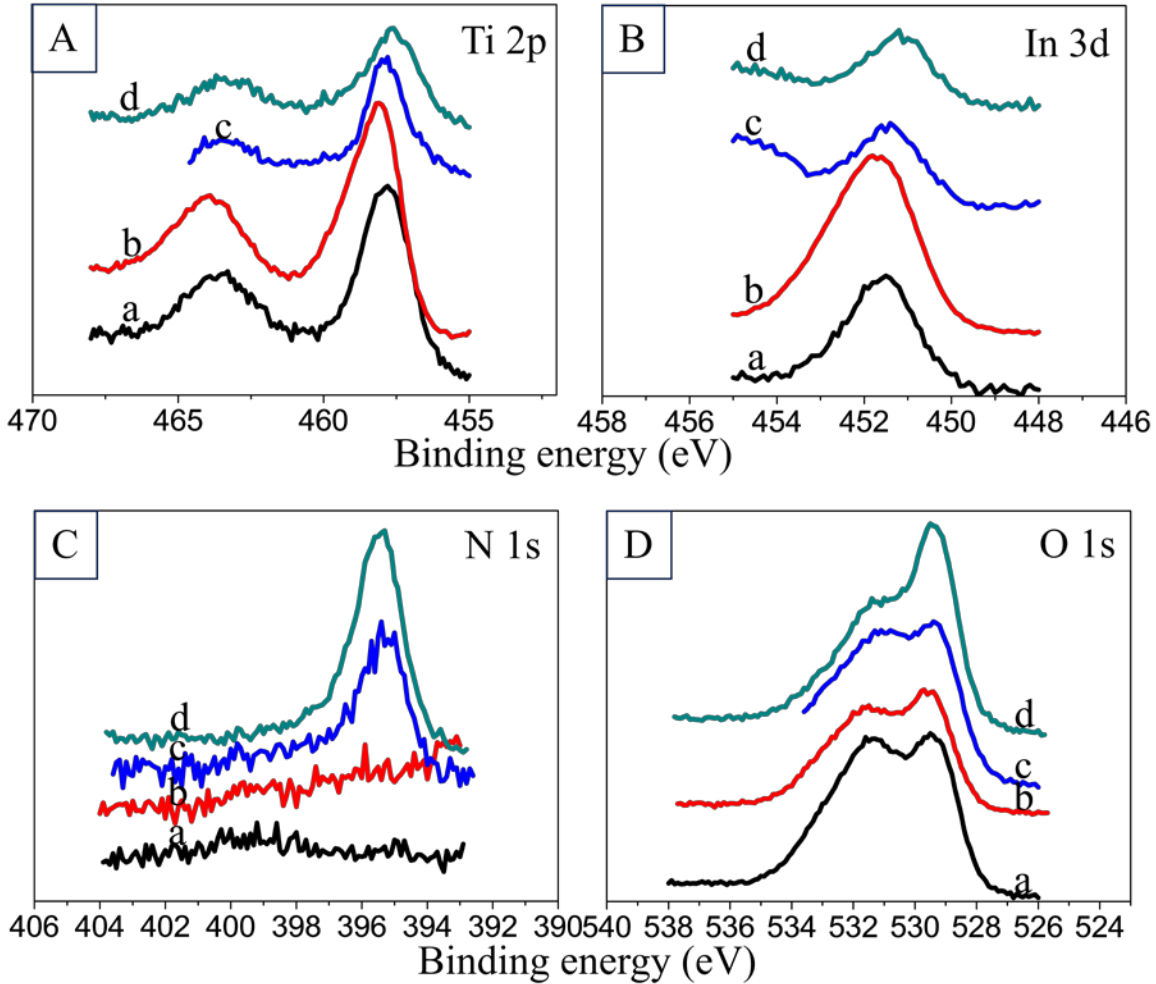
oxygen anions.²⁵ As N is less electron negative than O, the electron density around the anions decreases, increasing the electron density around the cations and caused the BE shift.²⁵

4.3.5.4 O 1s Core Level

Figure 4.11D shows that the O 1s core level is composed of at least three components. The peak positions and intensities are reliably determined by a standard curve fitting procedure using XPSPEAKS software. The O 1s signal at 529.8 eV is assigned to metal oxide according to the literature,²⁶ while the signal at 530.8 eV is probably due to oxygen in surface adsorbed hydroxyl groups²⁷ and the signal at 532.1 eV is from the surface adsorbed H₂O.

4.3.5.5 N 1s Core Level

The N 1s XPS spectrum in figure 11C has the peak position at 395.4 eV. In the report,²³ if the In₂O₃ was doped by ethylenediamine, which was described as substitutional doping, the N 1s peak is ~398 eV. The big difference of 2.6 eV between these two N 1s peaks correlates with the theoretical calculations of the relative values for the N 1s state in substitutional versus interstitial sites with a higher core level BE for the interstitial site.²⁸ Therefore, the N 1s XPS data confirms the N is substitutional instead of interstitial doping.



4.11 XPS spectra of (a) TiN (13 h)/In₂O₃ mixture and different nitridation time of TiN (13 h)/In₂O₃ for (b) 1 (c) 3 (d) 5 h at 750 °C under a 250 mL/min flow rate of NH₃.

4.4 Conclusions

A novel TiN-In nitride composite of TiN and InN was prepared by nitridation of TiO₂ first, then mixed with In₂O₃ and ammonolysis again under a NH₃ flow of 250 mL min⁻¹. The N-doped TiO₂ mixed with the InN system not only can increase water splitting activity, but also the stability. The change in the product with nitridation time was examined, and it was revealed that an active photocatalyst can be achieved by prolonging the first TiO₂ ammonolysis time. The

XRD and XPS spectra confirmed that the prepared powders had nitrogen substituted at some of the oxygen sites in the TiO_2 and In_2O_3 . The UV-Visible diffuse reflectance spectra absorbance varied with nitridation time from 1 to 5 h, whereas the oxygen 2p and nitrogen 2p electrons content changed and resulted in different valance band structure.²⁹ The optimum preparation conditions for TiN-In nitride in order to achieve high photocatalytic activity for water splitting are thus considered to be nitridation at 750 °C under NH_3 flow at 250 mL min^{-1} TiO_2 for 18 h then adding In_2O_3 , and further nitriding 3 h. The produced catalyst under these conditions has high crystallinity, which was achieved by complete reaction between starting materials, and the catalyst can stably generate H_2 gas maximum at 1277 $\mu\text{mol} \cdot \text{h}^{-1} \cdot \text{g}^{-1}$.

References

1. Heller, A., Chemistry and Applications of Photocatalytic Oxidation of Thin Organic Films. *Accounts of Chemical Research* **1995**, 28, (12), 503-508.
2. Linsebigler, A. L.; Lu, G.; Yates, J. T., Photocatalysis on TiO₂ Surfaces: Principles, Mechanisms, and Selected Results. *Chemical Reviews* **1995**, 95, (3), 735-758.
3. Borgarello, E.; Kiwi, J.; Graetzel, M.; Pelizzetti, E.; Visca, M., Visible light induced water cleavage in colloidal solutions of chromium-doped titanium dioxide particles. *Journal of the American Chemical Society* **1982**, 104, (11), 2996-3002.
4. Yamashita, H.; Ichihashi, Y.; Takeuchi, M.; Kishiguchi, S.; Anpo, M., Characterization of metal ion-implanted titanium oxide photocatalysts operating under visible light irradiation. *Journal of Synchrotron Radiation* **1999**, 6, (3), 451-452.
5. Nakamura, I.; Negishi, N.; Kutsuna, S.; Ihara, T.; Sugihara, S.; Takeuchi, E., Role of oxygen vacancy in the plasma-treated TiO₂ photocatalyst with visible light activity for NO removal. *Journal of Molecular Catalysis a-Chemical* **2000**, 161, (1-2), 205-212.
6. Sato, S., Photocatalytic activity of NO_x-doped TiO₂ in the visible light region. *Chemical Physics Letters* **1986**, 123, (1-2), 126-128.
7. Irie, H.; Watanabe, Y.; Hashimoto, K., Nitrogen-concentration dependence on photocatalytic activity of TiO_{2-x}N_x powders. *Journal of Physical Chemistry B* **2003**, 107, (23), 5483-5486.
8. Yu, J. C.; Yu, Ho; Jiang; Zhang, Effects of F- Doping on the Photocatalytic Activity and Microstructures of Nanocrystalline TiO₂ Powders. *Chemistry of Materials* **2002**, 14, (9), 3808-3816.
9. Wu, J.; Walukiewicz, W.; Shan, W.; Yu, K. M.; Ager, J. W.; Haller, E. E.; Lu, H.; Schaff, W. J., Effects of the narrow band gap on the properties of InN. *Physical Review B* **2002**, 66, (20), 201403.
10. Wu, J.; Walukiewicz, W.; Yu, K. M.; Ager Iii, J. W.; Haller, E. E.; Lu, H.; Schaff, W. J.; Saito, Y.; Nanishi, Y., Unusual properties of the fundamental band gap of InN. *Applied Physics Letters* **2002**, 80, (21), 3967-3969.
11. Matsuoka, T.; Okamoto, H.; Nakao, M.; Harima, H.; Kurimoto, E., Optical bandgap energy of wurtzite InN. *Applied Physics Letters* **2002**, 81, (7), 1246-1248.
12. Faulhaber, S.; Loeffler, L.; Hu, J.; Kroke, E.; Riedel, R.; Lange, F. F., Synthesis of nanocrystalline aluminum-gallium nitride (Al_{1(x)}Ga_(1-x)N; x=0.1 to 0.5) with oxide precursors via ammonolysis. *Journal of Materials Research* **2003**, 18, (10), 2350-2358.

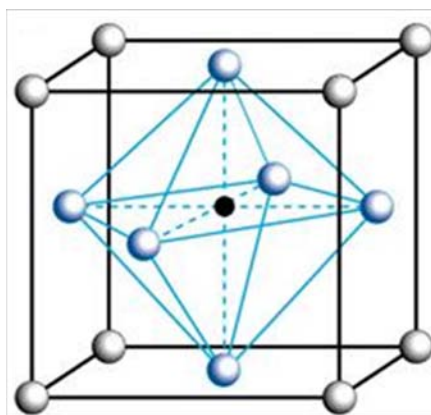
13. Kroke, E.; Loeffler, L.; Lange, F. F.; Riedel, R., Aluminum nitride prepared by nitridation of aluminum oxide precursors. *Journal of the American Ceramic Society* **2003**, 85, (12), 3117-3119.
14. Kisailus, D.; Choi, J. H.; Lange, F. F., GaN nanocrystals from oxygen and nitrogen-based precursors. *Journal of Crystal Growth* **2003**, 249, (1-2), 106-120.
15. Schwenzer, B.; Loeffler, L.; Seshadri, R.; Keller, S.; Lange, F. F.; DenBaars, S. P.; Mishra, U. K., Preparation of indium nitride micro- and nanostructures by ammonolysis of indium oxide. *Journal of Materials Chemistry* **2004**, 14, (4), 637-641.
16. Kudo, A.; Miseki, Y., Heterogeneous photocatalyst materials for water splitting. *Chemical Society Reviews* **2009**, 38, (1), 253-278.
17. Trainor, J. W.; Rose, K., Some Properties of InN Films Prepared by Reactive Evaporation. *Journal of Electronic Materials* **1974**, 3, (4), 821-828.
18. Guo, Q.; Kato, O.; Yoshida, A., Thermal-stability of Indium Nitride Single-crystal Films. *Journal of Applied Physics* **1993**, 73, (11), 7969-7971.
19. Dingman, S. D.; Rath, N. P.; Markowitz, P. D.; Gibbons, P. C.; Buhro, W. E., Low-Temperature, Catalyzed Growth of Indium Nitride Fibers from Azido-Indium Precursors. *Angewandte Chemie International Edition* **2000**, 39, (8), 1470-1472.
20. Xiao, J. P.; Xie, Y.; Tang, R.; Luo, W., Benzene thermal conversion to nanocrystalline indium nitride from sulfide at low temperature. *Inorganic Chemistry* **2003**, 42, (1), 107-111.
21. Levitt, A. P., *Whisker technology*. Wiley-Interscience: New York., 1970; p xii, 478 p.
22. Reyes-Gil, K. R.; Reyes-Garcia, E. A.; Raftery, D., Nitrogen-doped In₂O₃ thin film electrodes for photocatalytic water splitting. *Journal of Physical Chemistry C* **2007**, 111, (39), 14579-14588.
23. Lee, I. J.; Kim, J. Y.; Shin, H. J.; Kim, H. K., Near-edge x-ray absorption fine structure and x-ray photoemission spectroscopy study of the InN epilayers on sapphire(0001) substrate. *Journal of Applied Physics* **2004**, 95, (10), 5540-5544.
24. Chen, X.; Burda, C., Photoelectron Spectroscopic Investigation of Nitrogen-Doped Titania Nanoparticles. *The Journal of Physical Chemistry B* **2004**, 108, (40), 15446-15449.
25. Sathish, M.; Viswanathan, B.; Viswanath, R. P.; Gopinath, C. S., Synthesis, characterization, electronic structure, and photocatalytic activity of nitrogen-doped TiO₂ nanocatalyst. *Chemistry of Materials* **2005**, 17, (25), 6349-6353.

26. Donley, C.; Dunphy, D.; Paine, D.; Carter, C.; Nebesny, K.; Lee, P.; Alloway, D.; Armstrong, N. R., Characterization of indium-tin oxide interfaces using X-ray photoelectron spectroscopy and redox processes of a chemisorbed probe molecule: Effect of surface pretreatment conditions. *Langmuir* **2002**, 18, (2), 450-457.
27. Asai, N.; Inoue, Y.; Sugimura, H.; Takai, O., Electrochromic Reaction of InN Thin Films. *Journal of The Electrochemical Society* **1999**, 146, (6), 2365-2369.
28. Di Valentin, C.; Pacchioni, G.; Selloni, A.; Livraghi, S.; Giamello, E., Characterization of Paramagnetic Species in N-Doped TiO₂ Powders by EPR Spectroscopy and DFT Calculations. *The Journal of Physical Chemistry B* **2005**, 109, (23), 11414-11419.
29. Maeda, K.; Takata, T.; Hara, M.; Saito, N.; Inoue, Y.; Kobayashi, H.; Domen, K., GaN:ZnO Solid Solution as a Photocatalyst for Visible-Light-Driven Overall Water Splitting. *Journal of the American Chemical Society* **2005**, 127, (23), 8286-8287.

Chapter 5 - Synthesis and characterization of strontium titanate

5.1 Literature review on strontium titanate

Perovskites are mixed metal oxides with a general formula of ABO_3 (Figure 5.1). The A^{2+} metal ions sit on the corners of the structure and B^{4+} metal ions form an octahedral structure along with oxygen anions (Figure 5.2). All different kinds of perovskite oxide powders have wide applications, such as dense ferroelectric, thin film electronic components and electro-optical materials. Moreover, perovskite oxides are well-known catalysts for many purposes especially in photocatalytic oxidation and hydrogenation.¹⁻⁵ However, the small surface and low homogeneity of bulk materials, caused by incomplete solid-state reactions, result in less attractive catalysts.

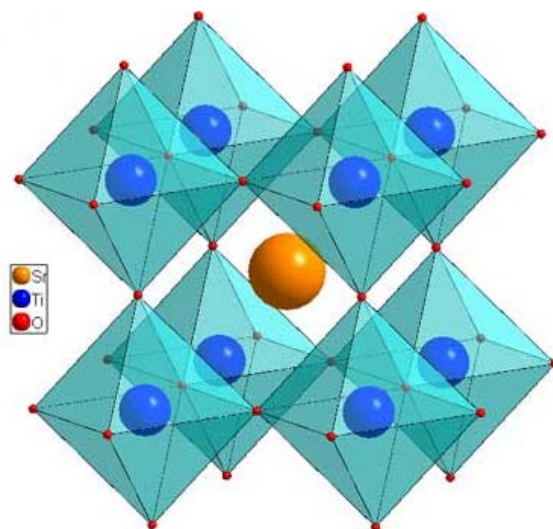


5.1 Perovskite (ABO_3) UnitCell

Many titanate compounds are perovskites such as strontium titanate ($SrTiO_3$), barium titanate ($BaTiO_3$) and strontium barium titanate ($Sr_{1-x}BaxTiO_3$). The work discussed here

focuses on synthesis, characterization and application of alkaline-earth metal titanates and in particular strontium titanate.

Strontium titanate is a perovskite with a cubic structure whose dielectric constant increases upon cooling.⁶ Non-stoichiometric or doped n-type semiconducting strontium titanate is used as dielectric and photoelectric materials.⁷ Strontium titanates are traditionally synthesized by solid-state methods. Metal carbonate and titanium oxide are mixed and ground together, then calcined above 1000 °C for more than 10 hours. Kudo et al. synthesized a series of strontium titanates by solid-state reaction at different temperatures and hours with different dopants.³ The synthesis is very easy and low cost. However, the resultant bulk materials have low surface areas, approximately 1 m²/g, and low homogeneity caused by incomplete reaction among starting materials. Since high sintering temperatures are required for reaction, many research groups approached titanate oxides synthesis by other methods and techniques, to obtain the perovskite structure phase with high purity and small particle size at low temperature. Some of those groups have used wet chemical methods for the synthesis of mixed metal oxides (Table 5.1).⁸ The mixed metal oxides prepared by wet chemical methods have advantages of higher homogeneity, surface area, and reactivity than by solid-state synthesis. For example, the perovskite oxides prepared by coprecipitation methods can reach up to 10 m²/g surface area. Wet chemical methods can produce pure strontium titanate phase at a low temperature by thermal decomposition of SrTiO(C₂O₄)₂·4H₂O⁹ precursor, or hydrolysis of strontium titanium carboxylates.¹⁰



5.2 Perovskite structure (BO₆ and A²⁺ layers)

The sol-gel process is one of the most widely used techniques for producing colloidal sols. Mixed metal oxides can be synthesized by the sol-gel technique by using a mixture of two metal alkoxides. The mixture can be metal salt and metal alkoxide or metal hydroxide and metal alkoxide. The final products can be obtained by calcination of dried or wet gels. These final crystalline products have fine homogeneous composition and high surface areas. Sol-gel synthesis of strontium titanates gives high purity, homogeneous and fine crystallinity.¹¹ For examples, strontium acetate and titanium isopropoxide were hydrolyzed together and form a gel. The gel was dried at 110 °C and then calcined at 900 °C. The calcination caused an increase of the particles size up to 500 nm and surface area to 20 m²/g. Moreover, S. Ahuja et al. have reported a method of gel to crystallite conversion, which can obtain the particle size of SrTiO₃ in the range 5-13 nm.¹² The experiment also shows the photocatalytic activities of these powders in the mineralization of phenol.

5.1 Wet Chemical methods for the synthesis of mixed metal oxides

Process	Method
Thermal decomposition	Oxalate
	Citrate
	Peroxide
	Acetate
	Complex cyanide
Evaporative Decomposition	Spray pyrolysis
	Liquid Mix
	Mixed-alkoxide
Sol-gel process	Carboxy-alkoxide
	Hydroxide-alkoxide
Hydrothermal synthesis	Hydroxides

5.2 Nanomaterials

The properties of materials are strongly affected by particle size, crystallinity and surface area. The particle size of nanomaterials is intermediate between single atoms and crystalline solids of 100 nm or less. The small sizes of materials result in a larger surface areas, which exhibit unexpected and new properties compared with bulk materials.^{13, 14} Moreover, the surface area is not the only factor affected; reactivity and optical band gap are also affected. The band gap influences the light absorption of the materials and significantly affects photocatalytic activities. It is the result of finite size when some of the electronic bands are converted into molecular orbitals. Also, surface atoms have a higher ratio compared with bulk atoms resulting in differences of chemical and physical properties compared with a single atom or the bulk materials, and some properties become quantized. Because of those interesting properties, every field of materials science, such as chemistry, physics, biochemistry and engineering are

exploring the new applications of those nano-size materials for varied purposes like electronics, optics, catalysis and solar energy conversion.¹⁵ The synthesis of the desired particle size, shape and surface structure are widely studied.

For semiconductor nanoparticles, the band gap between the conductance band and valance band gets bigger when the size of particles get smaller, resulting in a blue shift of the absorption edge. Moreover, these nanoparticles have non-linear optical properties because of induced polarization, which is affected by the intensity of incident light. The electric properties of the nanomaterials are changed by the different sizes.¹⁴ The electrical conductivity of nanoparticles decreases along with the transition of electronic band structure from bulk into separated molecular orbitals. Also, the sintering and miscibility of the nanomaterials are affected by size; smaller particles can achieve homogeneity of a certain phase at relatively lower temperatures.

5.3 Synthesis of titanates

5.3.1 Introduction

There are many ways for the synthesis of nanomaterials. Milling can decrease the sizes of bulk materials to a certain level. However, the resultant products are not homogeneous and could be contaminated by the milling media. For gas-phase synthesis, the reactions can be carried out by aerosol, chemical vapor deposition (CVD), solvated metal atom dispersion method (SMAD) or others. The aerosol applies heat treatment of the dispersed droplets of precursor.¹⁶ In the SMAD process, metals are vaporized and trapped in the frozen organic solvent matrix. For the wet chemical synthesis, there are xerogel, aerogel, hydrothermal, microemulsion and others methods. Microemulsion forms small droplets in the solution and each one is a reactor for

synthesis of nanoparticles. In hydrothermal, the precursors of metal oxides are sealed into an autoclave and heated up to make a high pressure environment. In aerogel synthesis, sol is formed first and then a gel network. The gel is treated by supercritical drying to preserve the network from collapse and preserve pore structure and high surface area.

5.3.2 Solid-state synthesis

Different inorganic solids can react with each other as molten liquids or gas phase, and high temperatures are required. The process includes many interfacial reactions such as solid-gas or solid-liquid. It has been applied for metal oxides synthesis for a long time. For example, the ceramic method is one of the oldest solid-state syntheses.¹⁷ The advantages of the method are low cost, easily available precursors and simplicity. But it also has problems of unexpected phases, inhomogeneity of dopants and observation of reaction progress is not easy.

The solid-state reaction starts from nuclei formation at the interfaces between reactants. The reaction rate depends on the diffusion of ions from the reacting materials and decreases when the counter ions become difficult to move around. Therefore, it requires high temperature to provide enough energy for ion transport. And the starting precursors have to be well mixed by grinding in order to increase contact between surfaces. Since the solid-state reaction relies on the interaction between starting precursors, the final oxide products can gain oxide from the atmosphere by decomposition of compounds. For example, the $\text{YBa}_2\text{Cu}_3\text{O}_{7-x}$ can be synthesized by mixing yttrium oxide, barium peroxide and cupric oxide, then calcinated in the air. And barium peroxide can be replaced by barium carbonate. When barium carbonate is used in the reaction, it decomposes at high temperature and produces highly reactive barium oxide. A similar reaction can be achieved by using precursors in citrates and acetates or nitrates. An

alternative way for solid-state synthesis is using co-precipitation or precursor methods.¹⁸ Because the cations are closer to each other in this situation, a lower temperature is required to proceed with the reaction.

For the co-precipitation method, the metal salts (carbonates, oxalates, formates or citrates) are dissolved in water then co-precipitated by concentration of the solution. The precipitated compounds are later treated with a high temperature. The reaction is shown in equation 5.1.



For the precursor methods, two different metal oxides co-exist as one material. For example, barium titanate can be synthesized by slowly heating of the barium titania citrate in air to burn out the organic matter. This method can obtain a higher purity and more accurate stoichiometry than other ceramic methods.

5.3.3 Gas phase synthesis

Using gaseous precursors or intermediates for synthesis of metal oxides is fairly common. There are many choices for reaction in gas phase, such as chemical transport, or aerosol methods.

5.3.3.1 Chemical vapor deposition (CVD) technique

CVD is often used for crystal growth and for the purification of solids. Purification is carried out by treating solid A with gaseous agent B, then transport of gaseous product AB followed by decomposition back to solid A and gaseous agent B. For example, chromium oxide can be synthesized by using halides as the solid A and water as the transport agent, gaseous agent

B. The reaction is a continual process, and the equilibrium constant depends on the temperature. Therefore, the desired final AB product can be achieved by adjusting temperature. And the final AB product can continuously flow.

Chemical vapor deposition (CVD) can be used to prepare fine thin films and coatings of inorganic materials. Various metal oxides can be deposited to form thin films on substrates. The process of film deposition can be carried out at a relatively lower temperature than the melting point of the material. The basic idea of CVD is that vapor phases of volatile precursors reach the heated substrate in the reaction chamber to form a new film of materials. Precursors are adsorbed onto the surface of substrate, and then react with substrate to form a thin film. The basic CVD components include the precursor delivery system, reactor, and pumping system to remove by-products of the reaction. The reactor can operate up to 800°C, and pressure is controlled between 0.1 mbar to 1 bar. This technique is widely used in industry for hard coatings such as cutting tools or engine parts.¹⁹ There are also other applications such as three-dimensional microelectronic components, coatings on glass, and catalyst coatings and layered architecture in solar cells.

A lot of precursors can be used for the CVD process, for example, metal hydrides (SiH_4), metal alkoxides ($\text{Si}(\text{OEt})_4$), metal alkyls ($\text{Al}(\text{iBu})_3$, GaEt_3), and volatile metal halides (TiCl_4) in the presence of an oxygen source (O_2 , N_2O , or water). Organometallic precursors are more widely used, since they are more volatile than the inorganic metal compounds. However, lower thermal stability causes easier decomposition and contamination. More than one metal precursor can be deposited simultaneously to produce mixed-metal oxide films, but the desired formula is difficult to be obtained. Because precursors or their intermediates have different volatilities and reactivity, the final product may have unexpected excess or deficiency of one agent. For

example, when a lead titanate (PbTiO_3) is synthesized by CVD, there is lead deficiency of lead caused by a higher desorption rate to the substrate and higher volatility of the lead oxide (PbO). On the other hand, a precursor with all stoichiometric elements for the product can be used.

Silicon oxide (SiO_2) films are common insulation and passivation layers in electronics. The insulation of Silicon oxide helps to separate and protect semiconductor layers in microcircuit electronic devices. Silicon alkoxides (tetraalkoxysilane, TEOS) are the precursors to produce SiO_2 thin film without an external oxygen source.



The decomposition temperature of the alkoxides is 750°C with or without outside oxygen sources. But the quality of the films can be enhanced by using oxygen in the air to remove the carbon contamination. Moreover, if ozone is used as the oxygen source, not only can the decomposition temperature be reduced to 300°C , but also results in a good quality of the product.

The CVD based techniques are summarized in the table 5.2. The vapor phase epitaxy (VPE) technique can grow epitaxial crystalline films with crystallographic orientation and single crystal lattice. The OMCVD and OMVPE techniques apply organometallic compound precursors with metal-carbon bonds. MOCVD technique uses the metal-organic precursors without any metal-carbon bonds (alkoxide, amines).

5.2 CVD based techniques

Acronym	Full Name of the Techniques
CVD	Chemical Vapor Deposition
VPE	Vapor Phase Epitaxy
OMCVD	Organometallic Chemical Vapor Deposition
OMVPE	Organometallic Vapor Phase Epitaxy
MOCVD	Metal-organic Chemical Vapor Deposition
MOVPE	Metal-organic Vapor Phase Epitaxy
PACVD	Plasma-assisted Chemical Vapor Deposition
LCVD	Laser-induced Chemical Vapor Deposition

5.3.4 Aerosol technique

The aerosol technique uses a suspension of fine solid particles or liquid droplets in a gas and passed through a heated region.²⁰ The reaction with gas and pyrolysis of precursor give the product particles. The solvent is dried out using high temperature and yield the solid particles. However, often hollow particles may form due to the precipitation of solutes.

Many ultrafine particles (< 100 nm) of oxides were obtained by the aerosol process (Table 5.3). The presence of oxygen is required for oxides production. Moreover, mixed-metal oxides can be prepared by using a precursor mixture (for example SiCl₄ and TiCl₄). The resultant aerogel samples usually agglomerate together due to the weak van der Waals forces. Compared with the chemical vapor deposition method, which uses substrate surface adsorbed gaseous precursors which then react to form the solid, the solid particles are produced right in the

gas phase through the aerosol method. Therefore, CVD makes films and the aerosol technique produces fine powders.

5.3 Oxide Powders Prepared by the Aerosol Method²¹

The most common aerosol produced samples are highly dispersed silicon oxide (silica)

Oxide Precursors	Oxide Precursors
SiO ₂	SiCl ₄
TiO ₂	TiCl ₄
Al ₂ O ₃	AlCl ₃
Bi ₂ O ₃	BiCl ₃
Cr ₂ O ₃	CrO ₂ Cl ₂
Fe ₂ O ₃	FeCl ₃ or Fe(CO) ₅
GeO ₂	GeCl ₄
NiO	Ni(CO) ₄
MoO ₂	MoCl ₅
SnO ₂	SnCl ₄ or SMe ₄
V ₂ O ₅	VOCl ₃
WO ₃	WOCl ₄
ZrO ₂	ZrCl ₄
AlBO ₃	AlCl ₃ and BCl ₃
Al ₂ TiO ₅	AlCl ₃ and TiCl ₄

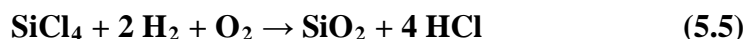
and titanium oxide (titania). A German company named Degussa developed the Aerosil® process to obtain silica product, which is called Aerosil A200 fumed silica, and the titania product named titania P25 Degussa.²² These oxides are all produced by flame hydrolysis/pyrolysis.

Titanium is produced by the reaction of titanium tetrachloride with water in the oxygen-hydrogen flame according to the following chemical reactions:



The overall reaction gives a highly dispersed titanium oxide sample combined with hydrogen chloride as a byproduct. This titanium oxide is a light powder composed with up to 40 nm diameter and a high surface area of 50 m²/g spherical particles. And it is widely used as a pigment for paints.

Fumed silica is obtained by the similar flame hydrolysis reaction:



Fumed silica and aerosol titania are widely used as the filler for rubber, additive for drilling fluids, plastics, paints, creams, tablets, cosmetic powders, toners, and toothpastes. The aerosol materials have high surface areas and low density. In the aerosol process, products are produced at the expense of energy. However, the products from aerosol methods sometimes cause the formation of hollow particles, which may be due to differences in nucleation and growth rate of the precursors.

5.3.5 Sol-gel technique

The sol-gel technique is one of the most widely used soft chemical methods for the metal and semimetal oxides synthesis. In this process, an oxide network is built by hydrolysis of alkoxides, followed by gelation and finally by removal of the solvent.²³ In contrast to the conventional solid-state method, a wet chemical synthesis can yield products which are homogenous nanosized oxides with high purity, and lower temperatures are required. It involves a colloidal sol which is converted into a gel during the aging.²⁴ The aging process is a controlled hydrolysis of metal-organic compounds (alkoxides) in an organic solvent. The sol-gel process

involves ololation (formation of hydroxyl bridges) and oxolation (formation of oxygen bridges) during hydrolysis (reactions 5.6-5.8). The oxolation is a condensation reaction, which causes the formation of colloidal agglomerates, and the ololation is responsible for the aggregation into a polymeric gel.



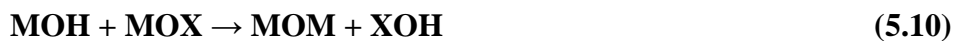
Where R is alkyl group and M is metal or semimetal (IV).

The gel formation is very complicated and is affected by the nature of starting material(s) (precursor[s]), solvents, precursor concentration, mixed solvents ratio, temperature, pH and aging time. In the process, metal alkoxides serve as starting materials and are hydrolyzed by water. During hydrolysis, alkoxy groups are replaced by OH followed by condensation and addition resulting in a sol containing oxide chains. The sol composed by colloidal particles or units in a solution goes through a gelation process by the agglomeration of these particles or sub-units into a big gel network structure. The final products are obtained by removing the solvent and further treated by annealing. The significant reduction in the volume of the gel causes increasing capillary forces. The gel network structure collapses because of the high capillary pressure in the pores and results in a less porous powder (xerogel). However, if supercritical extraction is applied, the solvent is removed above its critical temperature, which can preserve the structure of the gel network and yield a highly porous material (aerogel), which is discussed below.

5.3.6 Aerogel technique

The sol-gel method can prepare samples as a three dimensional porous solid. Because of liquid-vapor interfacial tension, the polymeric network could be destroyed during the drying. However, if the solvent is removed by supercritical drying, the structure can be prevented from collapse.²⁵⁻²⁸ Under the supercritical extraction of the solvent, the gel is processed with heat and pressure, giving rise to a nanocrystalline product with homogeneous composition, high porosity, and large surface area.^{29, 30}

Mixed oxides can be prepared by the sol-gel method to cogelate a mixture of metal precursors. Alcohol will be produced by the following hydrolysis of the metal alkoxide (5.9). A condensation reaction (5.10) of the partial hydrolyzed intermediate takes place to form a metal-oxygen-metal bridge (M-O-M) by either the removal of water (X is H) or alcohol (X is R).



After the condensation, the reaction yields MOM, MOM', and M'OM' (where M and M' are different metals). The final products may consist of three dimensional crosslinked networks with oxo-bridged metals. In mixed-metal aerogels, each metal site has several possible combinations of bridged neighbors. However, mixed metal oxides can result in two separate oxide phases (oxide segregation), or of one phase with cationic substitution in the lattice, depending on the solubility of the metal oxides in each other.³¹

Generally, different alcohols are used for the aerogel synthesis. For mixed metal oxide systems, one metal alkoxide is mixed with the other metal salt (nitrate, acetate, acetylacetonate,

citrate, or carbonate) through the acid-alkoxide route, or metal alkoxide is mixing with metal hydroxide through the hydroxide-alkoxide route followed by hydrolysis (gelation). The combination of acid anions or hydroxide leads to a faster gelation. However, it also causes impurities in the samples, which can be removed by calcination.^{12, 24, 31} Recently, strontium titanate aerogel synthesis using mixed two metal alkoxides was carried out to achieve a better gelation and prevent the formation of impurities.³² Since strontium oxides tend to produce a carbonate phase, during hydrolysis, supercritical drying, and calcination procedures, reagents have to be prevented from exposure to CO₂, thus supercritical solvent extraction was executed in a N₂ atmosphere.

The influence of solvent on the aerogel properties has been widely studied in our research group.^{33, 34} It was found that a solvent mixture of alcohol and toluene affected the hydrolysis of the aerogel, and resulted in higher surface areas of aerogels compared to pure alcohol solvents.³² The presence of the hydrophobic solvent may reduce surface tension in gel pores and thereby prevent sintering.³³ Therefore, toluene used as solvent not only accelerated the hydrolysis but also gelation processes. The resultant samples consisted of a more porous structure with less dense wet gels and a lower mass fractal dimension.³⁴ Finally, the excess of toluene in solvent was removed by supercritical drying in the autoclave to prevent the gel from stress and shrinkage and yielded a higher surface area.

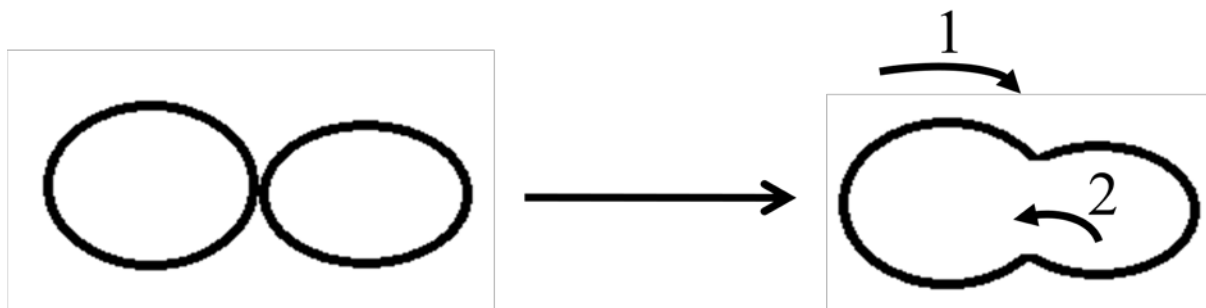
5.4 Temperature treatment

In the final process, heat treatment is usually needed for the preparation of the oxide products. The drying by heating the samples leads to the collapse of the network structure and a smaller surface area. Heating the powders at high temperatures forces the particles of the

powders to fuse together. Further heat treatment can produce dense solids. Different materials such as ceramics and ironware can be produced in this way. But the sintering process is undesirable for some nanomaterials, if a porous powder or monolith are desired.

In the heating process, particles were agglomerated to decrease the total surface area to lower free surface energy. Surfaces within particles have different chemical potentials based on the curvature. The convex surface has a positive surface energy, while the concave surface has a negative free energy. Mass transport goes through the diffusion process from the surface of convex particle to the concave interparticle. The driving force of sintering is greater for smaller particles, and nanoparticles can undergo significant increase of particle sizes.

The vacancy concentrations may decide the driving force for the diffusion of mass flow. Mass transportation has two main paths, which are surface diffusion and volume diffusion. In the surface diffusion, vacancies go from the neck surface to the convex surface, so the mass flow goes oppositely from the convex surface to the neck (Figure 5.3, path 1). In the volume diffusion, vacancies in the grain boundaries and/or dislocations in the grain matrix move in the volume to the surface while the mass flow tend to fill the place of moved vacancies (Figure 5.3, path 2).



5.3 Sintering by diffusion (path 1 - surface diffusion, path 2 - volume diffusion)

5.4.1 Heat treatment

In the heat treatment, reaction of particles goes through three main steps. The first step includes the fusing of particles together and the mass transfer from the convex to concave surfaces. In this step, the total pore volume and distance between particles decreases slightly. During the second step, diffusion and mass transfer processes occur and cause an increase in density and growing of interparticle necks and decrease in pore diameters and distances between particles. The final step creates a dense material with no remaining pores.

Particle size, shape, and packing are directly affected by heat treatment, especially for smaller particles, the mass transport happens faster and starts at lower temperatures. Larger particles growing by consuming smaller particles leads to a coarsening process. The influence of particles with a high surface area to volume ratio is bigger. During the agglomeration, a larger contact area between particles may cause a faster sintering and densification of the material.

5.4.1.1 Calcination

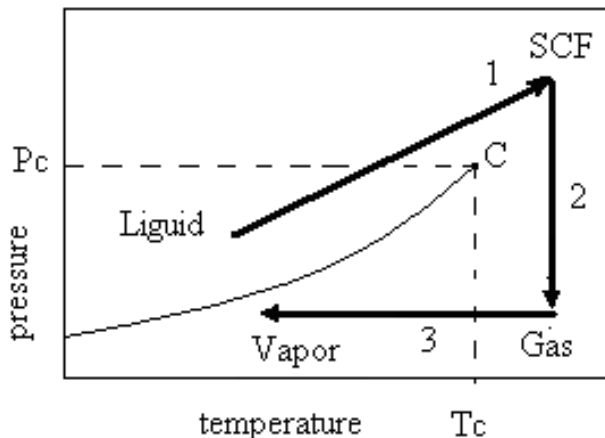
Calcination is required for decomposition of the precursor or the degradation of the impurities in the product to release gases (H_2O and CO_2 , or other gaseous products of degradation) in the open atmosphere (air, oxygen, nitrous oxide, or ozone). Metal oxides prepared by wet chemical methods usually include organic residues from the organic components during the synthesis, such as physisorbed solvent, ligands, or modifiers. Studies on different aerogels showed that calcination at 300-500°C is necessary to remove these organic residues, but it is still possible that a small amount remains in the pores and on the surface of the aerogel.³⁵

Calcination conditions have a significant influence on final characteristics of particle size, particle shape, surface area, crystallinity and phase purity. The organic residuals on the surface also cause samples having different physical and chemical properties. The reactive and catalytic activity of the samples may decrease because of covered active sites of the material.

5.4.1.2 Drying

There are several techniques which can help to dry just prepared wet gels. In the drying process, the wet gel always results in a collapsed network. Supercritical drying, low-temperature supercritical drying, and freeze-drying techniques have been applied to avoid the network structure from shrinkage.³⁶

In the supercritical drying process, the solvent in pores is transferred into a supercritical fluid (SCF). When solvent is above its critical pressure and critical temperature, it includes properties of liquid and gas together; therefore, there is no liquid-vapor interface and capillary pressure. During the supercritical drying, a gel is placed into an autoclave and heated as described steps showed in Figure 5.4. In the process, the solvent does not cross the liquid–gas phase boundary, so the gel structure is preserved from collapsing by capillary forces when solvent is vented out in the form of gas. After venting the aerogel is cooled down to room temperature in an inert atmosphere (N₂).



5.4 Temperature-pressure Diagram for Supercritical Drying, where C – Critical Point, SCF – Super Critical Fluid, T_c – Critical Temperature, P_c – Critical Pressure.^{26, 37}

Because many oxides dissolve in water at supercritical conditions and the oxide peptizes causing the production of a dense crystallized oxide bulk, water cannot be applied as a solvent. Alcohols are the most widely used solvents for the supercritical drying and preparation of the aerogels. However, extra caution is needed because of flammability combined with high critical temperature and pressure (Table 5.3).

5.4 Critical Points of Some Solvents²⁶

Solvent	Critical temperature T_c , °C	Critical pressure P_c , bar
H ₂ O	374	221
CO ₂	31	74
Methanol	240	80
Ethanol	243	64
Isopropanol	235	47
1-Butanol	290	43

It was found that a mixture of alcohol and organic solvent such as benzene or toluene is essential for obtaining mixed metal oxides with high surface areas and small crystallite sizes.³³ The adding of Toluene can help to reduce the surface tension at the gas-liquid interface and obtain more open porous network products with higher surface areas. However, the toluene and benzene cannot replace the alcohols totally. In the supercritical condition, alcohols are required for the prevention of phase separation of the alkoxide precursors.

Instead of alcohols, carbon dioxide can be used since it has a very low critical temperature of 31°C, and is non-flammable. These advantages make it a good candidate for low-temperature supercritical drying. Because of low temperature reaction, this process is energy efficient and non-explosive. The solvent in the gel is exchanged by liquid CO₂ before the drying step which gives dried aerogels (carbogels). However, CO₂ cannot be used for the preparation of some oxides because of reaction with carbon dioxide to form carbonates, such as alkaline-earth metal oxides. Instead of supercritical drying, the freeze-drying method can be applied by quickly freezing the gel, so the solvent can be prevented from crystallization, and later, it slowly evaporates by sublimation under vacuum. The final product (cryogel) is also a highly porous solid with a structure similar to an aerogel sample.

5.5 Modification of titanates by doping

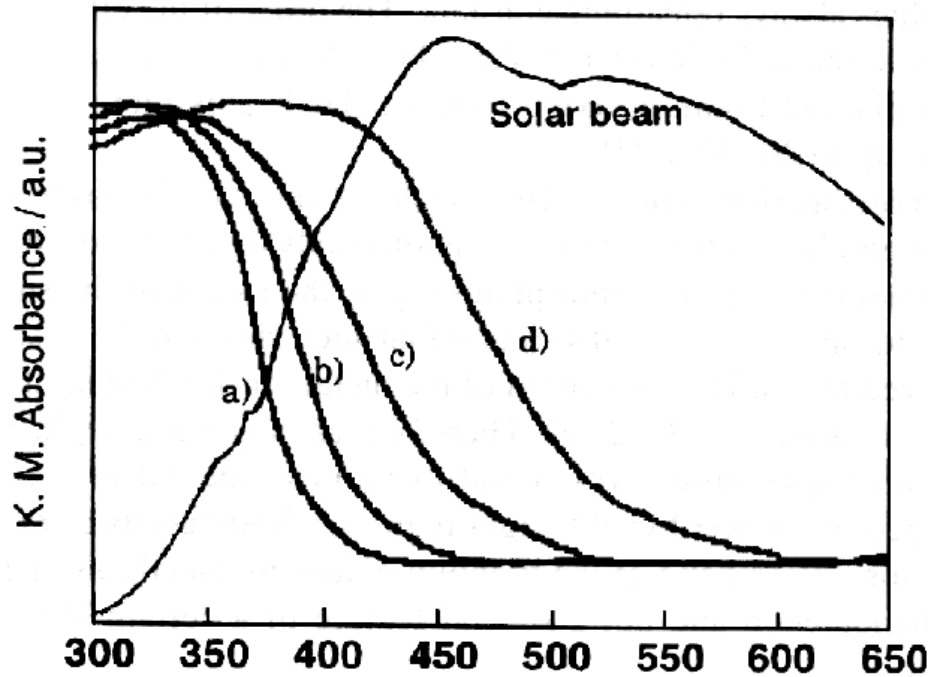
Modification of semiconductor photocatalysts to shift the light absorption into the visible light region can be achieved using several methods:³⁸

1. Phosensitization by dyes (sensitizers) and transition metal complexes of the type [Ru(2,2'-bipyridyl)₃].
2. Ion-implantation by surface bombardment with V, Cr, Mn, Fe, or Ni ions.

3. Doping with V, Cr, Rh, Mn, Fe, Co, Ni, or Cu metals.
4. Doping with S, N, or F nonmetals.
5. Impregnation or incorporation with fullerenes (C60).

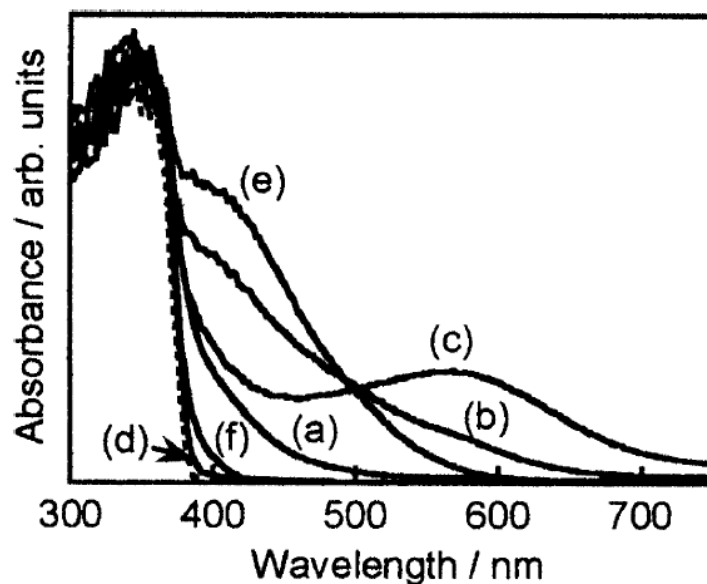
The modification of photocatalysts using doping with transition metal ions creates a forbidden band level between the band gap to enhance the visible light absorption. Our group has developed a way to modify the UV photocatalytic materials so that they can respond to visible irradiation.³⁹⁻⁴¹ These photocatalysts allow absorption of visible light due to being doped with metal ions during the synthesis. These novel nanosized catalysts may have a higher photocatalytic activity than bulk catalyst using visible light. Since nanomaterials have advantages of more surface area and active sites on the surface, the doping of strontium titanate nanoparticles can yield enhanced photocatalytic activity in visible light.

Ion implantation is a very effective method and can significantly enhance the adsorption of visible light by the sample. Figure 5.5 shows that Cr implanted TiO₂ has an increase in absorption of visible light with increasing of the concentration of implanted chromium.³⁸ The big disadvantage of this method is the high cost of catalyst production.



5.5 UV-Visible Absorption Spectra of a) Pure TiO₂ and b) –d) Cr Ion-implanted TiO₂ with Cr of 2.2, 6.6, and 13 x10⁻⁷ mol/g.³⁸

Instead of Ion-implantation, semiconductor catalysts can be doped with transition metals by wet chemical methods, and a variety of transition and noble metals were used for the doping of photocatalysts to enhance the visible light absorption (Figure 5.5).³ Electron donor levels were created between the Ti 3d and O 2p band gap by the dopants and caused the visible light response.



5.6 Diffuse reflectance spectra of SrTiO₃:M(0.5%). M = (a) Mn, (b) Ru, (c) Rh, (d) Pd, (e) Ir, and (f) Pt. A broken line represents a spectrum of nondoped SrTiO₃.³

However, the absorption of visible light does not always create a good photocatalyst, but it indicates the possibility for harvest of visible light. For example, Cr³⁺ doped TiO₂ or SrTiO₃ can have visible light absorption, but photoactivity was not enhanced and sometimes it even decreases.^{42, 43} The imbalanced charge in the crystal because of substitution of Ti⁴⁺ with Cr³⁺ leads to oxygen defects and/or Cr⁶⁺ ions, which stabilizes the charge balance. However, oxygen defects and Cr⁶⁺ ions act as recombination centers for excitons, and result in a decrease of photoactivity. In contrast, chromium and antimony co-doped SrTiO₃ showed an increase in photoactivity for H₂ production in the visible light range.⁴⁴ This study showed that the high photoactivities of co-doped TiO₂ and SrTiO₃ were due to co-doped Sb⁵⁺ ions which kept the charge balance. By a similar method, the Cr and Ta co-doped, Cr and Nb co-doped, Sb and Ni co-doped SrTiO₃ catalysts were synthesized by the solid-state reaction method and showed an increase in photocatalytic activities.⁴⁵

Doping TiO_2 with Fe^{3+} , Mo^{5+} , Ru^{3+} , Os^{3+} , Re^{5+} , V^{4+} and Rh^{3+} did enhance the photoactivity for carbon tetrachloride reduction and chloroform oxidation, but doping with Co^{3+} and Al^{3+} caused a decrease of photoactivity.⁴⁶

Instead of doping cations, the doping of titania with anions has been reported, which achieved the substitution of O^{2-} by anions in the lattice of TiO_2 to form $\text{TiO}_{2-x}\text{F}_x$, $\text{TiO}_{2-x}\text{N}_x$, or $\text{TiO}_{2-x}\text{S}_x$.⁴⁷⁻⁴⁹ If nitrogen was used as dopant for SrTiO_3 , anion defects form charge imbalance and caused problems, since the defects can act as electron-hole recombination centers. But charge could be balanced by adding F^- ion, which combined with N^{3-} to replace two O^{2-} . N doped SrTiO_3 had a lower photoactivity under visible light irradiation than the N and F co-doped sample.

References

1. Osterloh, F. E., Inorganic Materials as Catalysts for Photochemical Splitting of Water. *Chemistry of Materials* **2008**, 20, (1), 35-54.
2. Sasaki, Y.; Nemoto, H.; Saito, K.; Kudo, A., Solar Water Splitting Using Powdered Photocatalysts Driven by Z-Schematic Interparticle Electron Transfer without an Electron Mediator. *The Journal of Physical Chemistry C* **2009**, 113, (40), 17536-17542.
3. Konta, R.; Ishii, T.; Kato, H.; Kudo, A., Photocatalytic Activities of Noble Metal Ion Doped SrTiO₃ under Visible Light Irradiation. In *The Journal of Physical Chemistry B*, American Chemical Society: 2004; Vol. 108, pp 8992-8995.
4. Kudo, A.; Miseki, Y., Heterogeneous photocatalyst materials for water splitting. *Chemical Society Reviews* **2009**, 38, (1), 253-278.
5. Kim, J.; Hwang, D.; Kim, H.; Bae, S.; Lee, J.; Li, W.; Oh, S., Highly Efficient Overall Water Splitting Through Optimization of Preparation and Operation Conditions of Layered Perovskite Photocatalysts. *Topics in Catalysis* **2005**, 35, (3), 295-303.
6. Rooksby, H. P., Compounds of the structural type of calcium titanate. *Nature* **1945**, 155, (3938), 484-484.
7. Burn, I.; Neirman, S., Dielectric-Properties of Donor-Doped Polycrystalline SrTiO₃. *Journal of Materials Science* **1982**, 17, (12), 3510-3524.
8. Padmini, P.; Kutty, T. R. N., Wet chemical syntheses of ultrafine multicomponent ceramic powders through gel to crystallite conversion. *Journal of Materials Chemistry* **1994**, 4, (12), 1875-1881.
9. Gallagher, P. K.; Schrey, F.; Dimarcello, F. V., Preparation of Semiconducting Titanates by Chemical Methods. *Journal of the American Ceramic Society* **1963**, 46, (8), 359-365.
10. Riman, R. E.; Landham, R. R.; Bowen, H. K., Synthesis of Uniform Titanium and 1-1 Strontium-Titanium Carboxyhydrosols by Controlled Hydrolysis of Alkoxy-metal Carboxylate Precursors. *Journal of the American Ceramic Society* **1989**, 72, (5), 821-826.
11. Pfaff, G., Sol-gel synthesis of strontium titanate powders of various compositions. *Journal of Materials Chemistry* **1993**, 3, (7), 721-724.
12. Ahuja, S.; Kutty, T. R. N., Nanoparticles of SrTiO₃ prepared by gel to crystallite conversion and their photocatalytic activity in the mineralization of phenol. *Journal of Photochemistry and Photobiology A: Chemistry* **1996**, 97, (1-2), 99-107.

13. Rossetti, R.; Nakahara, S.; Brus, L. E., Quantum size effects in the redox potentials, resonance Raman spectra, and electronic spectra of CdS crystallites in aqueous solution. *The Journal of Chemical Physics* **1983**, 79, (2), 1086-1088.
14. Brus, L. E., Electron--electron and electron-hole interactions in small semiconductor crystallites: The size dependence of the lowest excited electronic state. *The Journal of Chemical Physics* **1984**, 80, (9), 4403-4409.
15. Zunger, A.; Wagner, S.; Petroff, P., New materials and structures for photovoltaics. *Journal of Electronic Materials* **1993**, 22, (1), 3-16.
16. Gurav, A.; Kodas, T.; Pluym, T.; Xiong, Y., Aerosol Processing Processing of Materials. *Aerosol Science and Technology* **1993**, 19, (4), 411-452.
17. Lengauer, W., Characterization of nitrogen distribution profiles in fcc transition metal nitrides by means of Tc measurements. *Surface and Interface Analysis* **1990**, 15, (6), 377-382.
18. Rao, C. N. R., Chemical synthesis of solid inorganic materials. *Materials Science and Engineering: B* **1993**, 18, (1), 1-21.
19. Hintermann, H. E., Tribological and protective coatings by chemical vapour deposition. *Thin Solid Films* **1981**, 84, (3), 215-243.
20. Drygas, M.; Czosnek, C.; Paine, R. T.; Janik, J. F., Aerosol-assisted vapor phase synthesis of powder composites in the target system GaN/TiN for potential electronic applications. *Materials Research Bulletin* **2005**, 40, (7), 1136-1142.
21. Schubert, U.; Hüsing, N., *Synthesis of inorganic materials*. Wiley-VCH: Weinheim New York, 2000; p xvii, 396 p.
22. Wagner, E.; Brünner, H., Aerosil, Herstellung, Eigenschaften und Verhalten in organischen Flüssigkeiten. *Angewandte Chemie* **1960**, 72, (19-20), 744-750.
23. Gopalakrishnan, J., Chimie Douce Approaches to the Synthesis of Metastable Oxide Materials. *Chemistry of Materials* **1995**, 7, (7), 1265-1275.
24. Hubert-Pfalzgraf, L. G.; Daniele, S.; Decams, J. M.; Vaissermann, J., The Quest for Single-Source Precursors for BaTiO₃; and SrTiO₃. *Journal of Sol-Gel Science and Technology* **1997**, 8, (1), 49-53.
25. Kistler, S. S., Coherent Expanded-Aerogels. *The Journal of Physical Chemistry* **1932**, 36, (1), 52-64.
26. Brinker, C. J.; Scherer, G. W., *Sol-gel science : the physics and chemistry of sol-gel processing*. Academic Press: Boston, 1990; p xiv, 908 p.

27. Campbell, L. K.; Na, B. K.; Ko, E. I., Synthesis and characterization of titania aerogels. *Chemistry of Materials* **1992**, 4, (6), 1329-1333.
28. Carnes, C. L.; Kapoor, P. N.; Klabunde, K. J.; Bonevich, J., Synthesis, Characterization, and Adsorption Studies of Nanocrystalline Aluminum Oxide and a Bimetallic Nanocrystalline Aluminum Oxide/Magnesium Oxide. *Chemistry of Materials* **2002**, 14, (7), 2922-2929.
29. Klabunde, K. J.; Stark, J.; Koper, O.; Mohs, C.; Park, D. G.; Decker, S.; Jiang, Y.; Lagadic, I.; Zhang, D., Nanocrystals as Stoichiometric Reagents with Unique Surface Chemistry. *The Journal of Physical Chemistry* **1996**, 100, (30), 12142-12153.
30. López, T.; Hernández, J.; Gómez, R.; Bokhimi, X.; Boldú, J. L.; Muñoz, E.; Novaro, O.; García-Ruiz, A., Synthesis and Characterization of TiO₂-MgO Mixed Oxides Prepared by the Sol-Gel Method†. *Langmuir* **1999**, 15, (18), 5689-5693.
31. Cho, W.-S.; Hamada, E., Synthesis of ultrafine BaTiO₃ particles from polymeric precursor: their structure and surface property. *Journal of Alloys and Compounds* **1998**, 266, (1-2), 118-122.
32. Demydov, D.; Klabunde, K. J., Characterization of mixed metal oxides (SrTiO₃ and BaTiO₃) synthesized by a modified aerogel procedure. *Journal of Non-Crystalline Solids* **2004**, 350, 165-172.
33. Utamapanya, S.; Klabunde, K. J.; Schlup, J. R., Nanoscale metal oxide particles/clusters as chemical reagents. Synthesis and properties of ultrahigh surface area magnesium hydroxide and magnesium oxide. *Chemistry of Materials* **1991**, 3, (1), 175-181.
34. Diao, Y.; Walawender, W. P.; Sorensen, C. M.; Klabunde, K. J.; Ricker, T., Hydrolysis of Magnesium Methoxide. Effects of Toluene on Gel Structure and Gel Chemistry. *Chemistry of Materials* **2002**, 14, (1), 362-368.
35. Schneider, M.; Baiker, A., Aerogels in Catalysis. *Catalysis Reviews: Science and Engineering* **1995**, 37, (4), 515 - 556.
36. Tewari, P. H.; Hunt, A. J.; Lofftus, K. D., Ambient-temperature supercritical drying of transparent silica aerogels. *Materials Letters* **1985**, 3, (9-10), 363-367.
37. Schubert, U.; Hüsing, N., *Synthesis of inorganic materials*. 2nd, rev. and updated ed.; Wiley-VCH: Weinheim ; [Great Britain], 2005; p xx, 409 p.
38. Kaneko, M.; Okura, I., *Photocatalysis : science and technology*. Kodansha ; Springer: Tokyo Berlin ; New York, 2002; p xvi, 356 p.
39. Wang, J.; Uma, S.; Klabunde, K. J., Visible light photocatalysis in transition metal incorporated titania-silica aerogels. *Applied Catalysis B: Environmental* **2004**, 48, (2), 151-154.

40. Uma, S.; Rodrigues, S.; Martyanov, I. N.; Klabunde, K. J., Exploration of photocatalytic activities of titanasilicate ETS-10 and transition metal incorporated ETS-10. *Microporous and Mesoporous Materials* **2004**, 67, (2-3), 181-187.
41. Martyanov, I. N.; Uma, S.; Rodrigues, S.; Klabunde, K. J., Decontamination of Gaseous Acetaldehyde over CoO_x-Loaded SiO₂ Xerogels under Ambient, Dark Conditions. *Langmuir* **2005**, 21, (6), 2273-2280.
42. Herrmann, J.-M.; Disdier, J.; Pichat, P., Effect of chromium doping on the electrical and catalytic properties of powder titania under UV and visible illumination. *Chemical Physics Letters* **1984**, 108, (6), 618-622.
43. Mackor, A.; Blasse, G., Visible-light induced photocurrents in SrTiO₃-LaCrO₃ single-crystalline electrodes. *Chemical Physics Letters* **1981**, 77, (1), 6-8.
44. Kato, H.; Kudo, A., Visible-Light-Response and Photocatalytic Activities of TiO₂ and SrTiO₃ Photocatalysts Codoped with Antimony and Chromium. *The Journal of Physical Chemistry B* **2002**, 106, (19), 5029-5034.
45. Ishii, T.; Kato, H.; Kudo, A., H₂ evolution from an aqueous methanol solution on SrTiO₃ photocatalysts codoped with chromium and tantalum ions under visible light irradiation. *Journal of Photochemistry and Photobiology A: Chemistry* **2004**, 163, (1-2), 181-186.
46. Choi, W.; Termin, A.; Hoffmann, M. R., The Role of Metal Ion Dopants in Quantum-Sized TiO₂: Correlation between Photoreactivity and Charge Carrier Recombination Dynamics. *The Journal of Physical Chemistry* **1994**, 98, (51), 13669-13679.
47. Asahi, R.; Morikawa, T.; Ohwaki, T.; Aoki, K.; Taga, Y., Visible-Light Photocatalysis in Nitrogen-Doped Titanium Oxides. *Science* **2001**, 293, (5528), 269-271.
48. Yu, J. C.; Yu; Ho; Jiang; Zhang, Effects of F- Doping on the Photocatalytic Activity and Microstructures of Nanocrystalline TiO₂ Powders. *Chemistry of Materials* **2002**, 14, (9), 3808-3816.
49. Umebayashi, T.; Yamaki, T.; Tanaka, S.; Asai, K., Visible Light-Induced Degradation of Methylene Blue on S-doped TiO₂. *Chemistry Letters* **2003**, 32, (4), 330-331.

Chapter 6 - Water Splitting under Visible Light using Aerogel Prepared Strontium Titanate (SrTiO₃) Nanomaterials Doped with Ruthenium and Rhodium Metals

In our laboratories, nanostructured strontium titanate visible-light-driven photocatalysts containing rhodium and ruthenium were synthesized by a modified aerogel synthesis using ruthenium chloride and rhodium nitrate as dopants precursors, and titanium isopropoxide and strontium metal for the metal sources. The well-defined crystalline SrTiO₃ structure was confirmed by X-ray diffraction (XRD). After calcination at 500 °C, diffuse reflectance spectroscopy showed an increase of light absorption at 370 nm due to the presence of Rh³⁺; however an increase of calcination temperature to 600 °C led to a decrease in intensity, probably due to loss of surface area. An increase in rhodium doping also led to an increase in absorption at 370 nm; however, these higher amounts of dopant lowered photocatalytic activity. The modified aerogel synthesis allows greatly enhanced H₂ production performance from an aqueous methanol solution under visible light irradiation, compared with lower surface area conventional materials. We believe this enhanced activity is due to higher surface areas while still yielding high quality nanocrystalline materials. Furthermore, the surface properties of these nanocrystalline aerogel materials are different, as exhibited by higher activities in alkaline solutions, while conventional materials (via high temperature solid-state synthesis methods) only exhibit reasonable hydrogen production in acidic solutions. Moreover, an aerogel synthesis approach gives the possibility of thin-film formation and ease of incorporation for practical solar devices.

6.1 Introduction

Many photocatalysts have been reported for water splitting under UV-Vis light. However, visible-light-driven photocatalysts are of more interest because sun-light possesses a larger portion of visible light. Fewer materials for water splitting under visible light have been reported. Domen and coworkers have reported GaN-ZnO and GeZnN₂-ZnO solid solutions for overall water splitting under visible light.¹⁻³ However, these oxy(nitride) photocatalysts need the assistance of co-catalysts such as Cr₂O₃-Rh₂O₃ to be active. On the other hand, two-step photocatalysis systems for overall water splitting mimicking photosynthesis in green plants have been broadly studied. These Z-scheme photocatalysis systems are composed of two photocatalysts, which generate H₂ and O₂ by different catalysts along with a reversible redox couple. The redox couple acts an electron mediator to transfer electrons from the O₂ production photocatalyst to the H₂ production photocatalyst. Fujihara et al. achieved overall water splitting using a system consisting of Pt/TiO₂-Br and TiO₂-Fe³⁺ components, but it only worked under UV light irradiation.⁴ Some other visible-light-driven systems also have been reported.⁵⁻⁷ Sayama et al. and Abe et al. reported Z-scheme photocatalysis systems using an IO³⁻/I⁻ redox couple as an electron mediator.^{5, 6} Moreover, Kudo et al and Mills et al. observed visible-light-driven Z-scheme photocatalysis systems using Pt/SrTiO₃:Rh for H₂ evolution,⁸ BiVO₄,⁹ Bi₂MoO₆,¹⁰ and WO₃¹¹ for O₂ evolution along with Fe³⁺/Fe²⁺ couple as a electron mediator.^{7, 12} However, a Pt co-catalyst not only assists water splitting reactions but also back-recombination reactions, such as water formation from evolved H₂ and O₂. In contrast to Pt, a Ru co-catalyst is an effective cocatalyst that does not enhance the back reaction.¹³ Therefore, Ru may be a better choice than Pt to be the reaction sites for H₂ generation on the surface of composites as a co-catalyst.

SrTiO₃:Rh is a proven photocatalyst with high activity for H₂ evolution in methanol-water solution under visible light.⁸ The unique character of doped Rh has reversible oxidation states (+3, +4, etc.) in SrTiO₃. Therefore, the SrTiO₃:Rh photocatalyst is activated by the help of reduction of Rh(IV) to Rh(III) during H₂ evolution in an aqueous methanol solution under visible light irradiation.⁸

In this study, we report that crystalline SrTiO₃:Rh can be prepared by a modified aerogel procedure.¹⁴ The synthesis of mixed metal oxides by sol-gel or aerogel methods can be achieved by the co-gelation of metal precursors to form single-phase nanosized strontium titanate. However, the product often consists of two separate oxide phases. In this research, the mixed alkoxide route through the mixing of two metal alkoxides results in a better gelation and higher purity of final product. The supercritical drying procedure allows higher surface areas and uniform pore structure, and helps to prevent strontium oxides from forming a carbonate phase by reacting with CO₂ in air during hydrolysis. The influence of solvent on the aerogel process also has been previously studied in our research group.¹⁴⁻¹⁶ It was found that two different polarities of a mixed solvent system can help to control the hydrolysis of the aerogel resulting in a higher surface area. The added hydrophobic solvent may reduce tension in gel pores and further prevent sintering.¹⁵ Therefore, we used mixed ethanol-toluene as a solvent to perform the aerogel synthesis.

6.2 Materials and methods

All procedures were performed under argon, because strontium metal is sensitive to water and oxygen. All autoclave treatments for supercritical drying were performed on a Parr 4843 instrument. SrCO (≥ 99.9% trace metals basis), TiO₂ (nanopowder, ~21 nm particle size, ≥

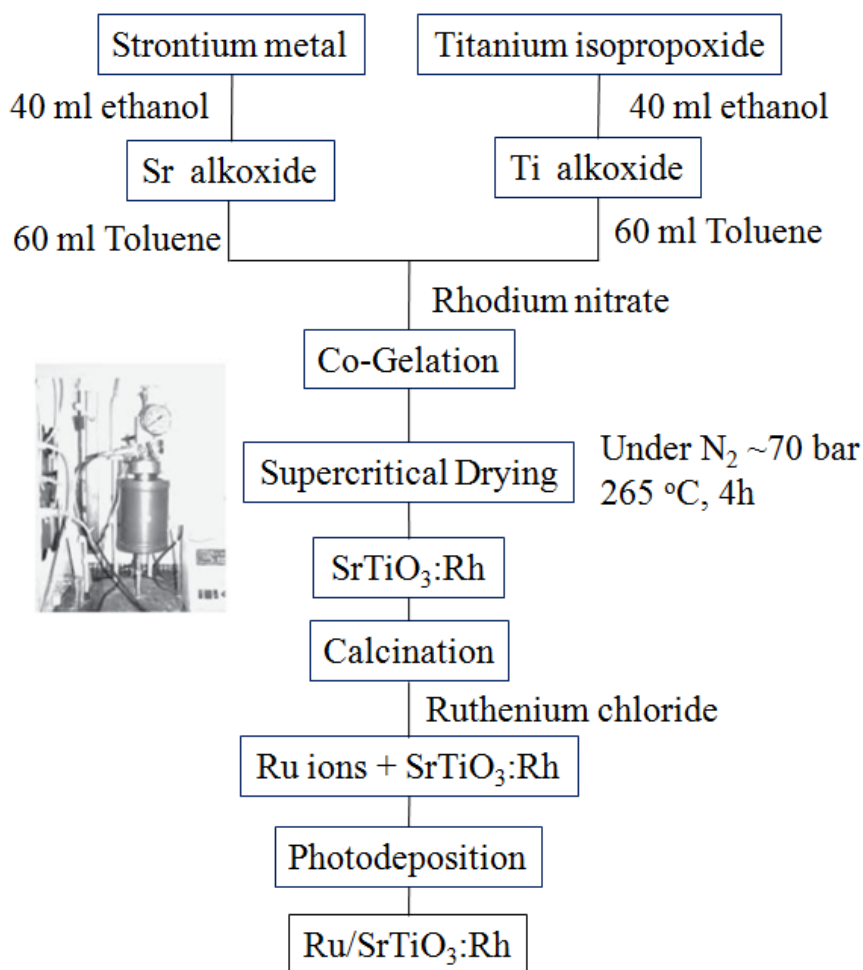
99.5% trace metals basis), Rh_2O_3 (powder, 99.8%), $\text{RuCl}_3 \cdot n\text{H}_2\text{O}$ (99.98% trace metals basis), Titanium (IV) isopropoxide (97%), absolute ethanol (200 proof), calcium hydrate (powder, 99.99% trace metals basis), toluene strontium metal (99% dendritic pieces), and Rhodium(III) nitrate solution ~10 % (w/w) (Rh in > 5 wt. % HNO_3) were used as received.

Synthesis of strontium titanium oxide doped with rhodium was carried out by a conventional solid-state reaction.^{8, 13} The starting materials, SrCO_3 , TiO_2 and Rh_2O_3 were mixed in a mortar according to the ratio Sr/Ti/Rh = 1.07:0.99:0.01. The mixture was calcined at 1273 K for 10 h in air. Ru (1.0 wt %) co-catalyst (working as active sites for H_2 evolution) were loaded on the photocatalysts by photodeposition from aqueous methanol solutions (10 vol%) containing $\text{RuCl}_3 \cdot n\text{H}_2\text{O}$.¹³ The cocatalyst-loaded photocatalysts were collected by filtration and washed with water.

The modified aerogel procedure for mixed metal oxides employs the preparation of metal alkoxide mixtures in an ethanol–toluene solvent, hydrolysis, cogelation of alkoxide mixture, and supercritical drying of the solvent. The scheme for aerogel-prepared $\text{SrTiO}_3\text{:Rh}$ by a modified aerogel procedure is presented in figure 6.1. $\text{SrTiO}_3\text{:Rh}$ aerogels were prepared in ethanol mixture with toluene in a toluene-to-ethanol volume ratio of 1.5. Ethanol was dried by boiling with CaH_2 overnight and collected by distillation before use. In a 250 ml flask, 0.02 mol (1.75 g) of Sr metal was allowed to react with 40 ml of ethanol under a flow of argon and constant stirring. In a separate 250 ml flask, 0.02 mol (5.9 mL) of titanium isopropoxide was added to 40 ml of ethanol with similar stirring under Ar, allowing a 1:1 stoichiometric ratio between Sr and Ti. After this, 60 ml of toluene was added into each flask forming clear solutions. The alkoxide solutions were mixed together and stirred and rhodium nitrate added in a different mole ratio (1 % ~). Then this mixture was hydrolyzed with a stoichiometric amount of doubly distilled water

by a slow, dropwise addition. The slow water hydrolysis transformed a solution of alkoxides into a slightly milky wet gel (gel in ethanol–toluene solution). The viscous solution was left for aging by vigorously stirring at room temperature for 1 h.

The wet gel was transferred to a 600 ml glass liner and placed in an autoclave. The autoclave was flushed with nitrogen, and then pressurized to 100 psi (6.9 bar, 6.9×10^5 Pa). The reactor was slowly heated to 265 °C. The pressure increased from 100 to 700 psi (48.3 bar, 48.3×10^5 Pa) upon heating. At 265 °C, the solvent vapors were removed by quick venting to the atmosphere, followed by flushing the reactor with nitrogen to remove any remaining solvent vapors. Finally the autoclave was cooled to room temperature. The residual solvent that was removed by calcination of the resulting SrTiO₃:Rh powders in air at different temperatures. Ru co-catalysts were loaded on photocatalysts by photodeposition from aqueous methanol solutions (10 vol%) containing RuCl₃ · nH₂O.¹³ The cocatalyst-loaded photocatalysts were collected by filtration and washed with water.



6.1 Modified aerogel procedure from alkoxides for Ru/SrTiO₃:Rh synthesis.

6.3 Results and discussion

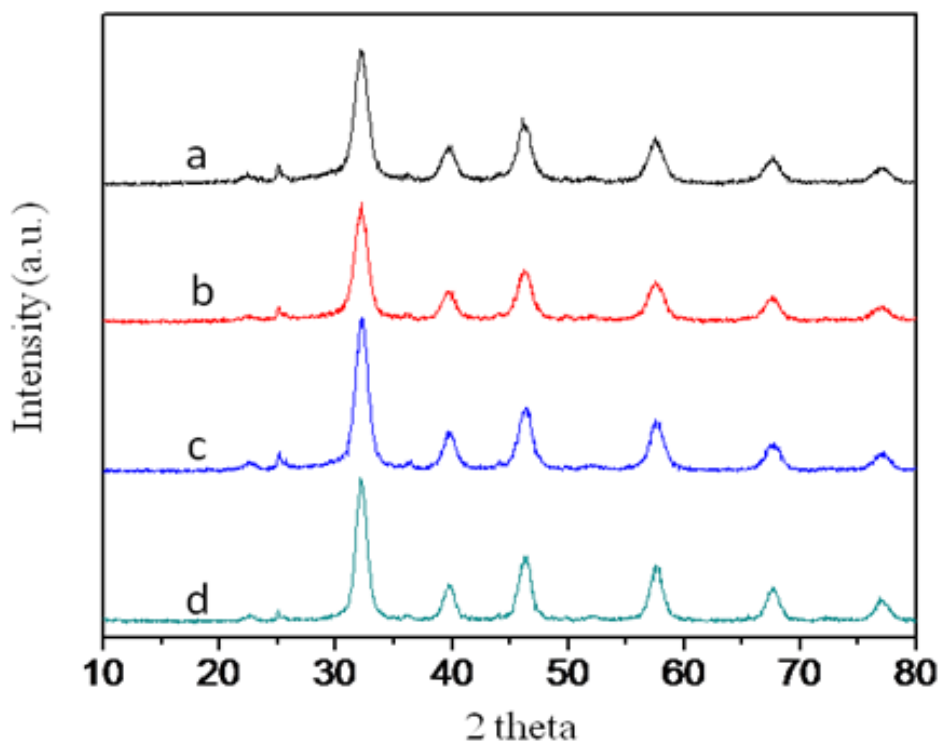
6.3.1 Strontium titanate calcination at different temperatures

SrTiO₃:Rh samples were synthesized by the aerogel method and calcined at different temperatures. Figure 6.2 shows the XRD patterns of SrTiO₃:Rh treated previously at different calcination temperatures. The XRD patterns confirm the well-defined crystalline SrTiO₃ structure. These samples do not require high-temperature treatments to initiate a phase transition from amorphous to crystalline. The Rhodium could not be observed in the XRD pattern, because it was loaded at only 1 mole %.

are shown in table 6.1. The highest surface area that we obtained is 130 m²/g, which is much higher than that achieved by solid-state or hydrothermal synthesis methods. Table 6.1 shows the higher calcination temperature, the larger the crystallite size obtained from the XRD pattern. This shows that the higher calcination temperature can improve the crystal structure and reduce the defects by atom rearrangement. The better crystalline nature may result in a higher water splitting activity. However, the surface area and the total pore volume decrease when a higher calcination temperature was applied. Surface area is also very important for a catalyst. A large surface can increase the water-catalyst interface resulting in a better activity. Therefore, the highest catalytic activity achievement must be balanced at a certain point between crystallinity and surface area. Moreover, calcination is a necessary treatment for most catalysts. It can remove the residues of solvent or other organic agents, which were used during the synthesis. The different calcination temperatures for the resulting samples also have been tested, which shows that 500 °C is the turning point of calcination temperature influence between crystallinity, surface area, and solvent residue removal (note the dramatic decrease of surface area, table 6.1). The water splitting reactions were conducted in a 10 vol % methanol solution after further doping with Ru as a co-catalyst. Ru is used as a co-catalyst for the hydrogen production. It can be homogeneously doped by the photodeposition method.⁸

6.1 Characteristic properties of SrTiO₃:Rh (1 mole %) calcined in air at different temperatures.

Calcination temperature (°C)	Average crystallite size (nm)	Surface Area (m ² /g)	Total pore volume (cm ³ /g)	Average pore size (nm)
n/a	5.0	130	0.76	15.7
300	5.8	106	0.54	15.7
400	6.0	111	0.57	15.7
500	6.8	78.4	0.52	15.7

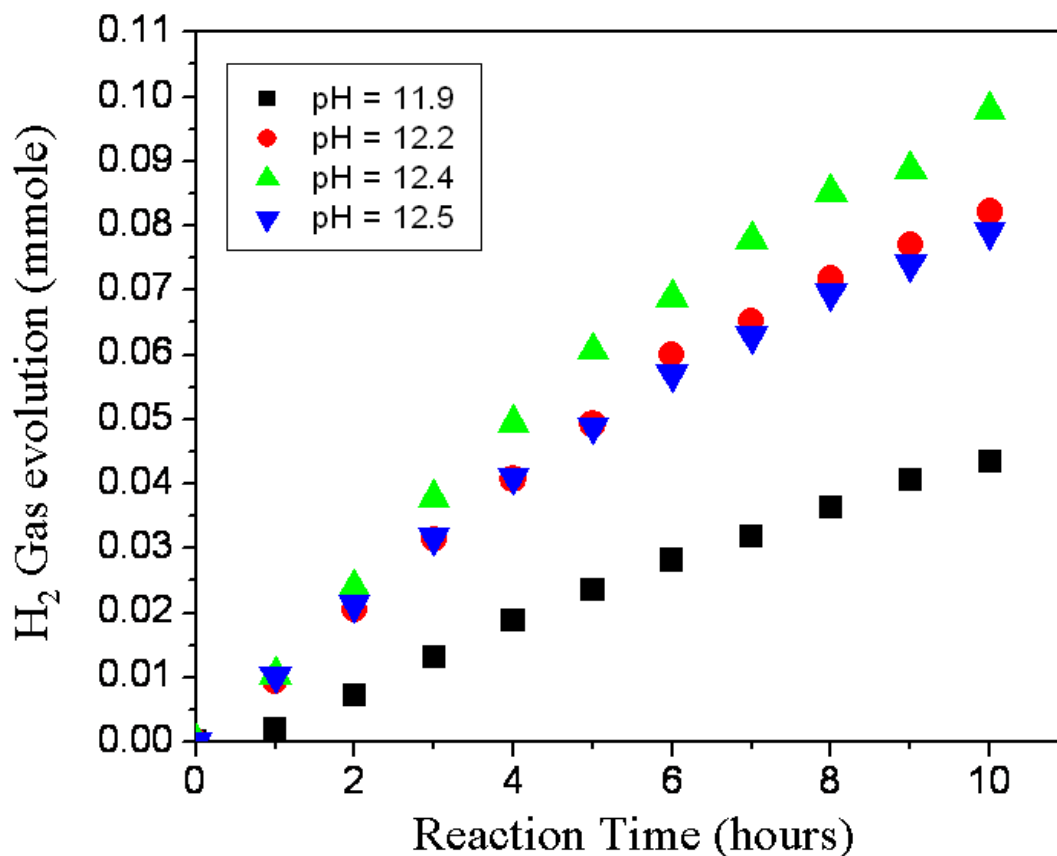


6.2 Powder XRD patterns of SrTiO₃:Rh calcined in air at different temperatures. (a) as synthesized (b) 300 °C (c) 400 °C (d) 500 °C.

6.3.2 H₂ generation of strontium titanate at different pHs

Aerogel synthesis SrTiO₃:Rh samples have a very different character than the solid-state synthesis samples. Aerogel synthesis samples have higher hydrogen production activities under basic (alkaline) conditions compared with solid-state synthesis samples, which have higher activity under acidic conditions. Figure 6.3 shows the relative activities of H₂ production of aerogel SrTiO₃:Rh (1.5 wt% Ru, 1mole % Rh, calcination temperature 550 °C) under visible light in 10 vol % methanol solution at different pHs. The result shows that the H₂ production is very sensitive to solution pH and pH = 12.4 is the best condition for the aerogel synthesis samples. The inorganic semiconductor electronic band structure strongly affects the photocatalytic properties. To facilitate photochemical water reduction to occur, the potential of the conduction band of the semiconductor must exceed the proton reduction potential of 0.0 V vs NHE at pH = 0 (-0.41 V at pH = 7).¹⁷ In other words, a higher pH of the solution environment requires a more negative conduction band position of the semiconductor to make the reaction happen. Based on these parameters, aerogel synthesis would produce much smaller particles (crystallites) than solid-state synthesis, resulting in an increase of band gap of SrTiO₃ and thereby require a higher pH to fit the conduction band better and help achieve a higher activity. Moreover, Rabuffetti et al. showed by chemisorption of atmospheric CO₂ and pyridine, as probes of acid and base sites, that the differences in surface acidity between samples of SrTiO₃ synthesized using different approaches are rather slight with a mixture of SrO-based and TiO₂-based terminations.¹⁸ On the other hand, their results showed that surface atomic structure of SrTiO₃ depends strongly on the synthetic method with regard to the reactive adsorption of atmospheric CO₂, which varied significantly between samples. These results suggest that these aerogel materials possess more nucleophilic O²⁻ surface centers. Perhaps the preferred higher pH

reaction conditions help preserve those reaction O^{2-} sites, that seem to be important in the overall water splitting mechanism.

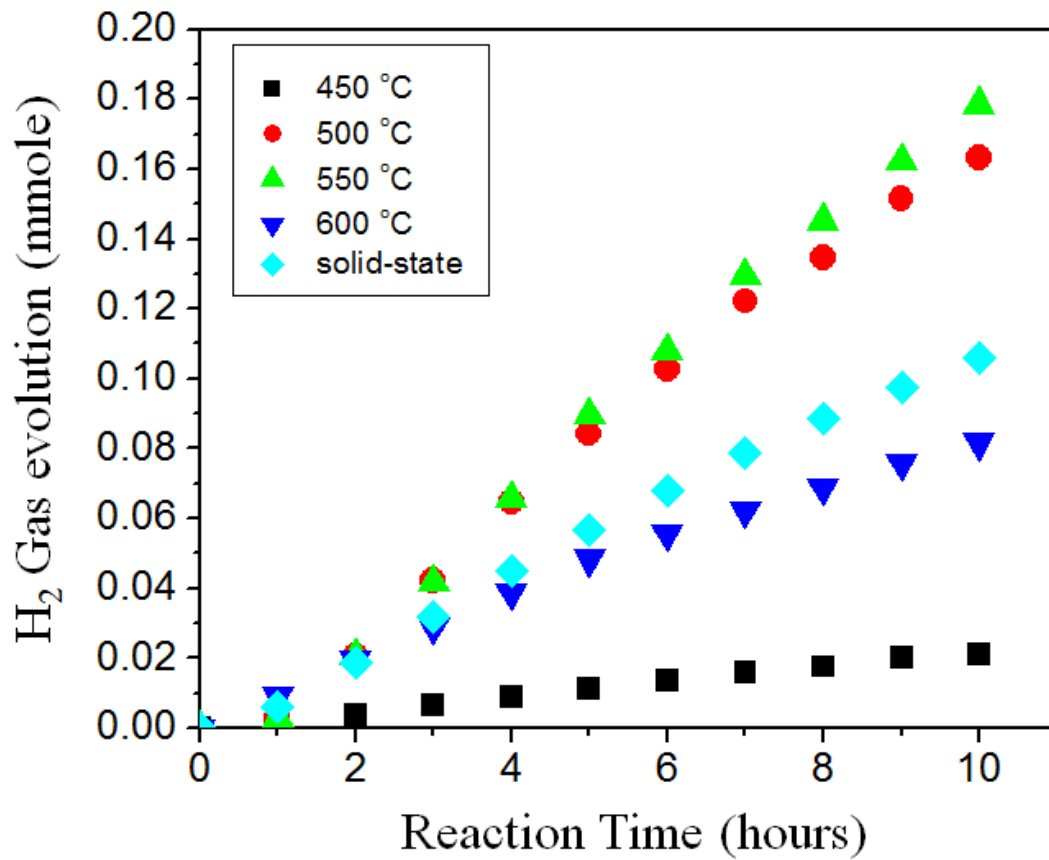


6.3 Dependence of H_2 evolution activity of $SrTiO_3:Rh$ (1.5 wt% Ru, 1 mole% Rh, cal. 550 °C) at different pHs under visible light in 10 vol% methanol-water solution.

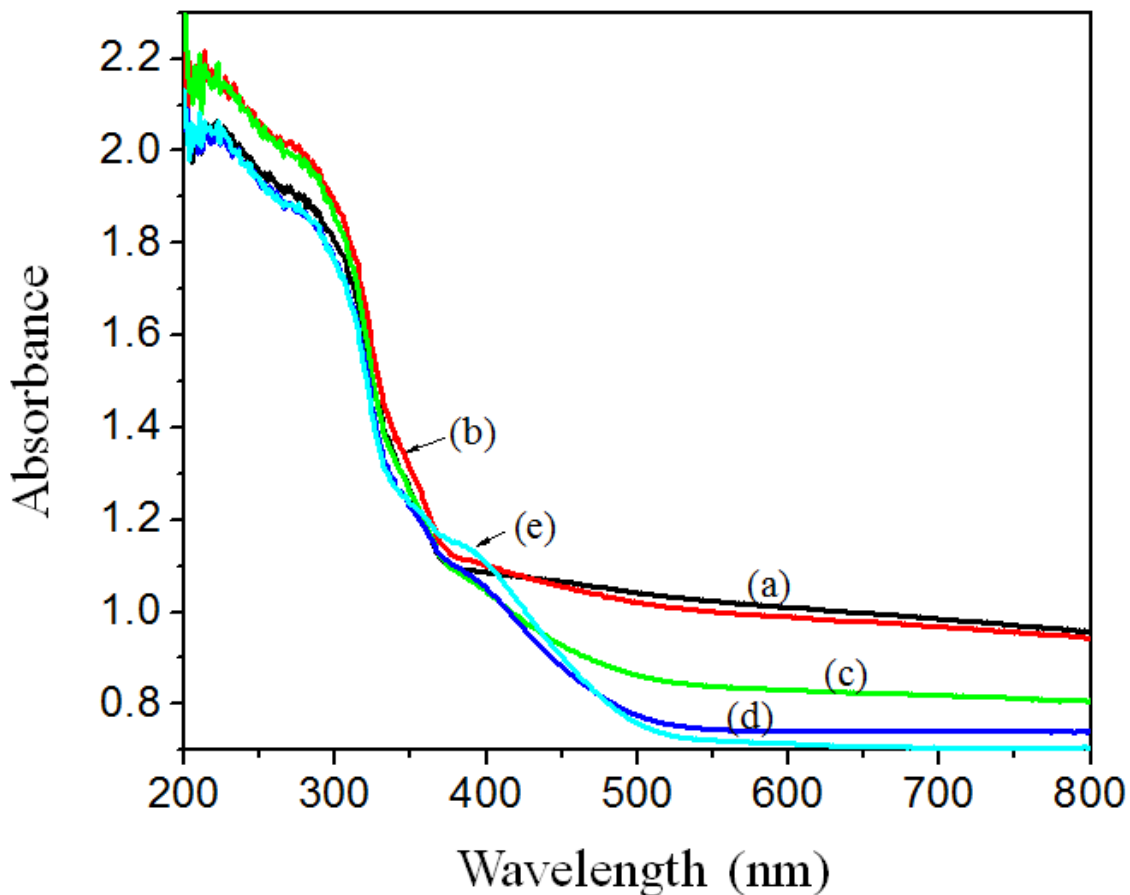
6.3.3 Dependence of H_2 evolution activity of aerogel $Ru/SrTiO_3:Rh$ on different calcination temperatures

$SrTiO_3:Rh$ samples with different calcination temperatures show a variation in H_2 evolution activity (figure 6.4) (pH = 12.4, adjusted by NaOH under visible light, with a conventional solid-state synthesized sample for comparison). The results show that a calcination temperature of 550 °C has the best activity. The calcination temperatures strongly affected the nanoparticle surface condition. Figure 6.5 shows the diffuse reflectance spectra of Rh-doped

aerogel SrTiO₃ (1.5 wt% Ru, 1.25 mole% Rh) with different calcination temperatures. The decrease of absorption between 500 nm to 800 nm when calcination temperatures were increased from 450 °C to 500 °C may be due to loss of organic contaminants. Indeed, figure 6.5c corresponds to the most active catalysts with calcination at 550 °C. The absorption band in the visible region at 420 nm is attributed to Rh³⁺.¹⁹ We believe that Rh³⁺ is an important visible light chromophore, and is present even up to 550 °C. Thus, it is likely that the Rh³⁺ sites are important for light induced exciton formation. However, except the 284.4 eV binding energy of C (figure 6.11a), which is normally used as an internal calibration, there are still existing other signals of carbons in the XPS spectrum indicating that even after treated with 500 °C, the residues from precursors could not be completely removed.



6.4 Dependence of H₂ evolution activity of SrTiO₃:Rh (1.5 wt% Ru, 1 mole% Rh) upon different calcination temperatures under visible light in 10 vol % methanol-water solution.

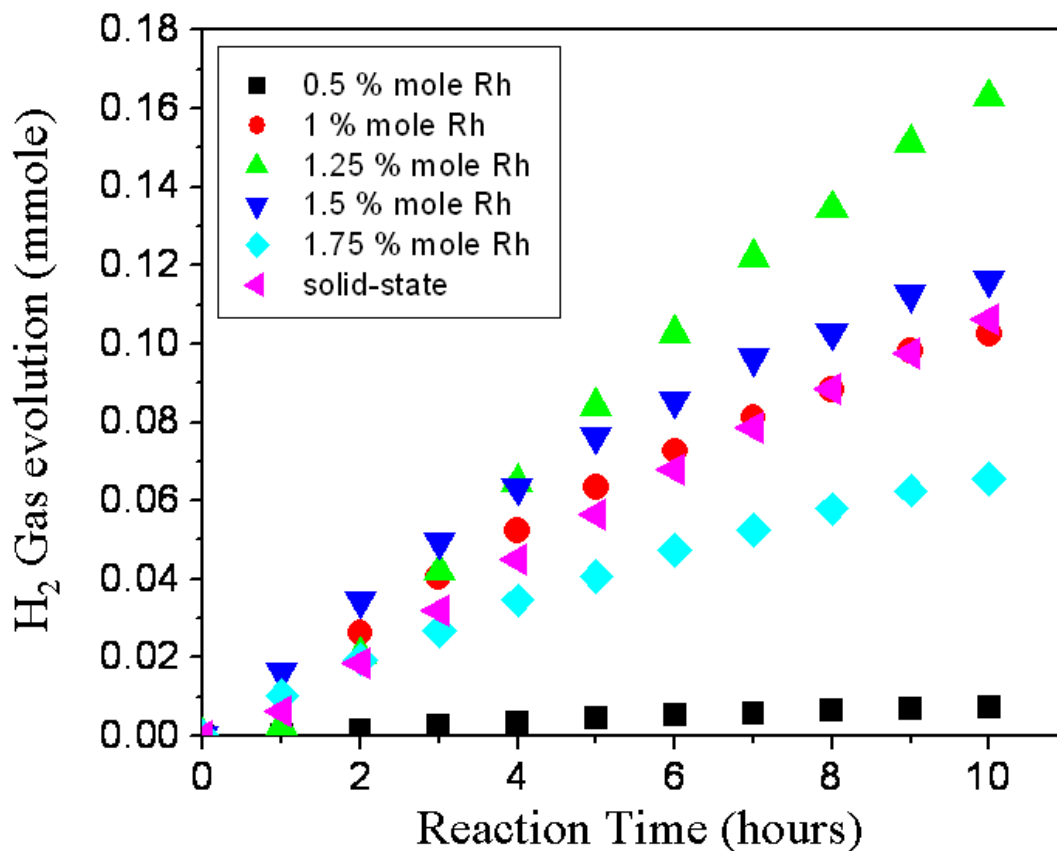


6.5 Diffuse reflectance spectra of Rh-doped aerogel SrTiO₃ (1.5 wt% Ru, 1.25 mole% Rh) from different calcination temperatures (a) 450 °C (b) 500 °C (c) 550 °C (d) 600 °C (e) 650 °C.

6.3.4 Dependence of H₂ evolution activity of aerogel Ru/SrTiO₃:Rh on different Rh doping amounts

SrTiO₃:Rh samples with different amounts of Rh have been synthesized by the modified aerogel method. Figure 6.6 shows dependence of H₂ evolution activity of Rh-doped aerogel SrTiO₃ (1.5 wt% Ru, cal. 500 °C) upon the different doping amount in 10 vol % methanol solution (pH = 12.4, adjusted by NaOH) under visible light along with a conventional solid-state synthesized sample for comparison. The optimal doping amount is Ru/SrTiO₃:Rh(1.25 mole % Rh) (figure 6.6). The highest hydrogen production can generate ~54 % more H₂ gas than a solid-

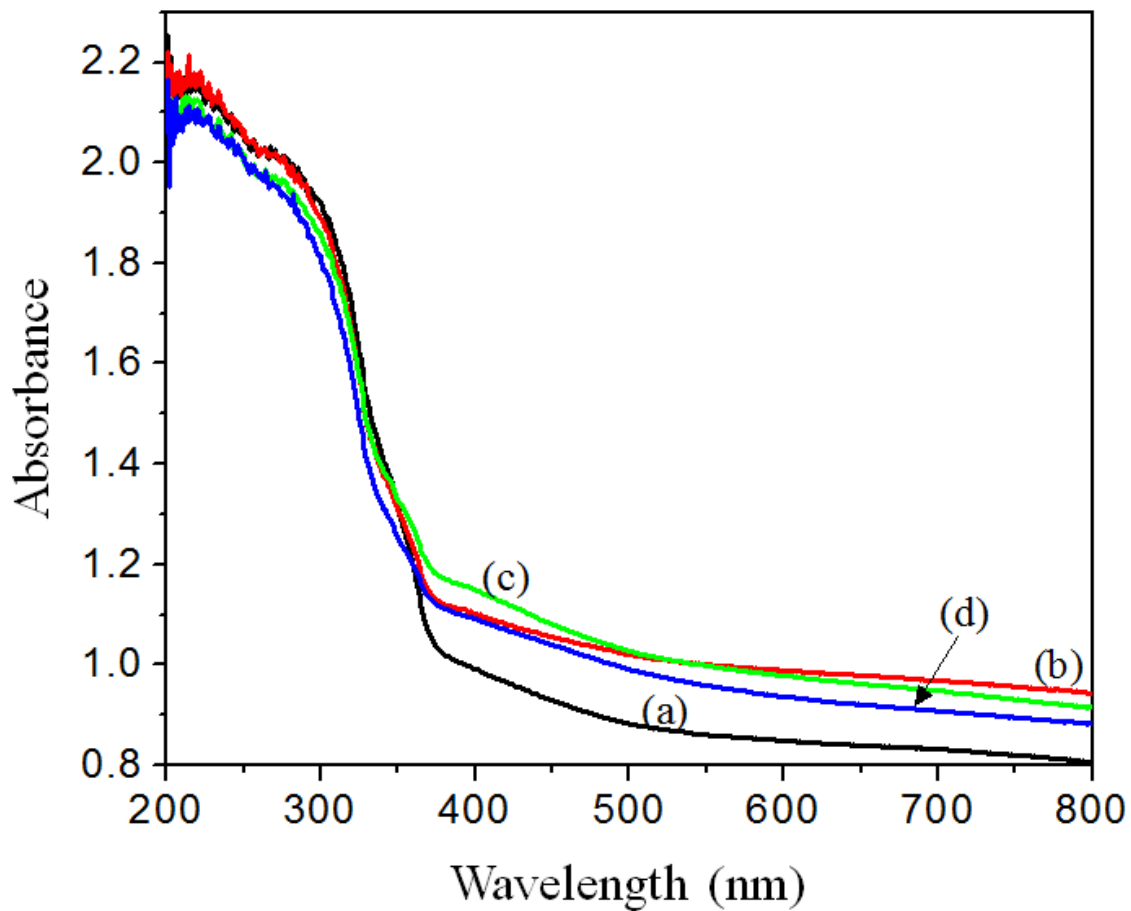
state synthesis sample in 10 hours. Figure 6.7 shows the diffuse reflectance spectra of Rh-doped aerogel SrTiO₃ (1.5 wt% Ru, cal. 500 °C) with different doping amounts. The highest visible light absorption starting from 520 nm was found for samples with higher loading than 1.0 mole% of Rh, and these loadings are optional for valence-conduction band electron promotion. This enhanced absorption corresponds to enhanced photocatalytic hydrogen evolution. Interestingly, with loading up to 1.75 mole%, the visible region absorption and H₂ production decreases (figure 6.6 and 6.7). Moreover, in the early stage, the 1.5 mole% Rh loading sample (figure 6.6) had a slightly higher activity than the 1.25 mole% Rh sample; however, the activity of the former system decreased gradually after 10 hours. This deactivation may imply the possibility of Rh acting as back-reaction sites. In order to reach the balance between recombination and generation of the electrons and holes, the distribution of Rh in the particles is very important. Indeed, aerogel synthesis can yield smaller particles than conventional solid-state synthesis methods. This smaller size can aid the electrons/holes to more rapidly reach the particle surface because of a shorter travel distance. In other words, the generated excitons from one Rh will have a lower possibility of contacting another Rh on the path to the particle surface. Thus, the Rh loading is critical, as is particle size. Moreover, figure 6.8 shows the TEM images of different SrTiO₃:Rh samples with different amounts of Rh. The aerogel samples can have a very homogeneous particle size, which is only around 10 nm when the Rh loading was 1.0 mole% (figure 6.8a). However, a higher loading of Rh may cause the increase of particle size and a larger range of size distribution (figure 6.8d).



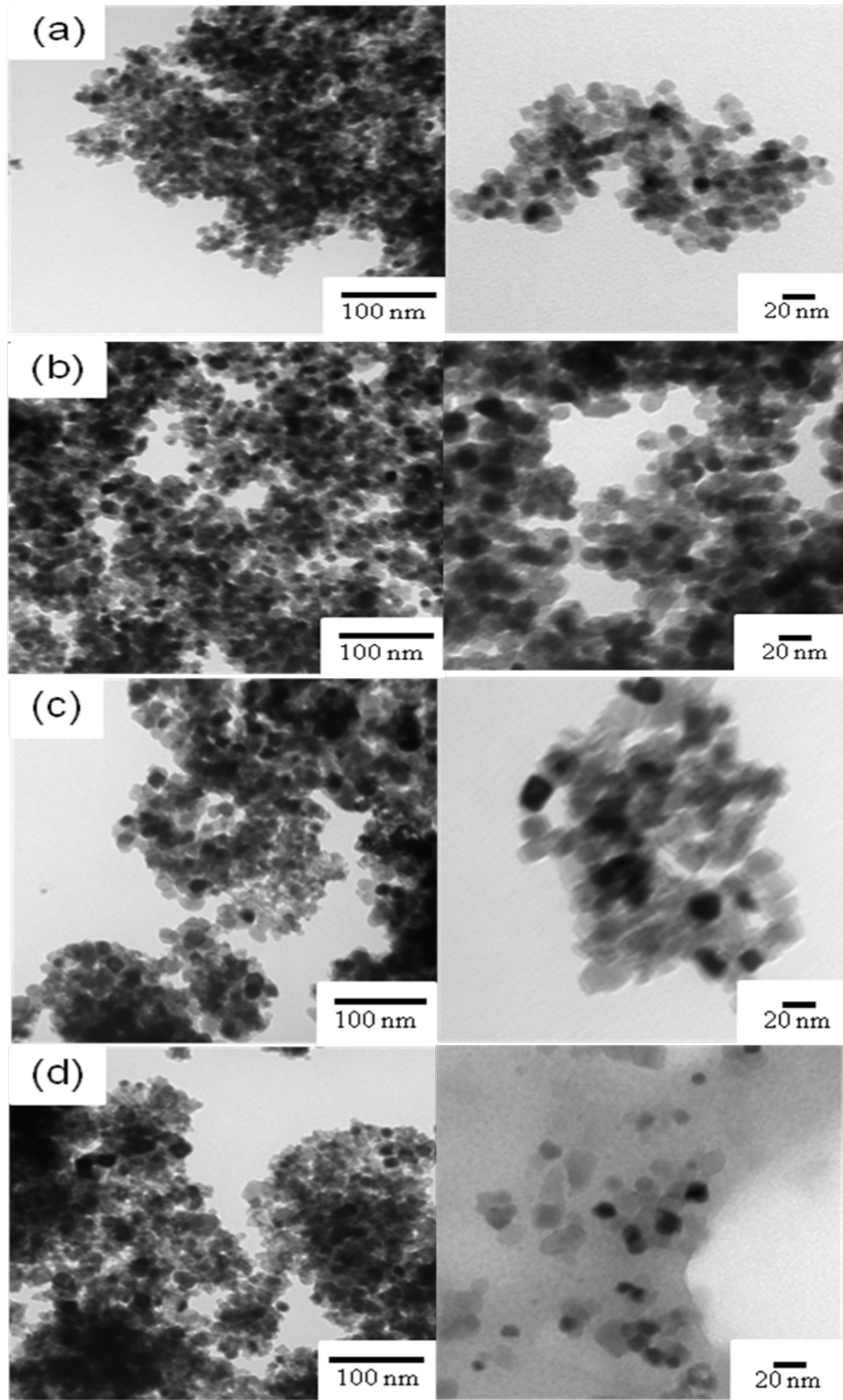
6.6 Dependence of H₂ evolution activity of Rh-doped aerogel SrTiO₃ (1.5 wt% Ru, cal. 500 °C) at different doping amounts in 10 vol % methanol-water solution (pH = 12.4, adjusted by NaOH) under visible light.

6.3.5 Dependence of H₂ evolution activity of aerogel Ru/SrTiO₃:Rh upon the different co-catalyst Ru amounts

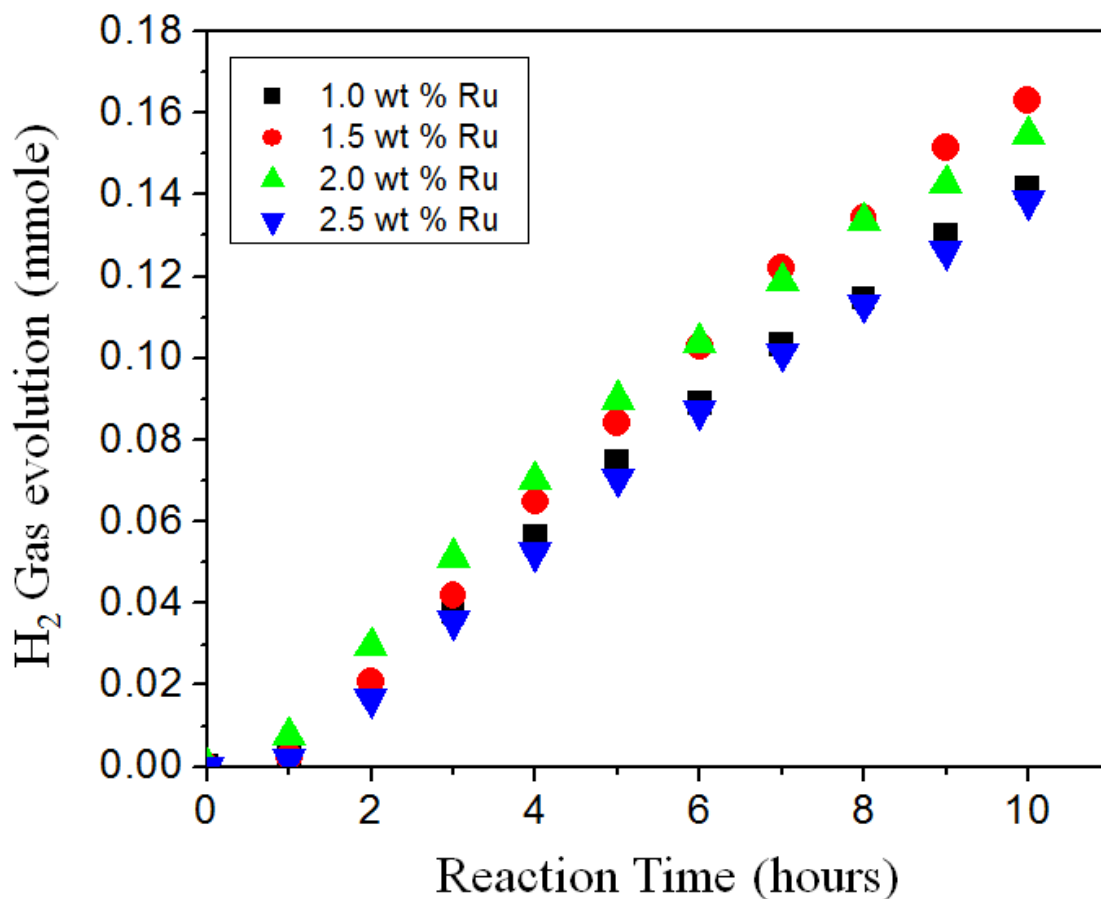
Figure 6.9 shows the dependence of H₂ evolution activity of aerogel SrTiO₃:Rh (1.25 mole %, cal. 500 °C) upon the different co-catalyst amounts. The optimal co-catalyst seems to be Ru/SrTiO₃:Rh(1.5 wt % Ru). Figure 6.9 shows that when the loading of Ru was more than 2.0 wt %, the photocatalyst had a high activity in the beginning but it changed to a lower rate after 5 hours. A possible explanation is similar to that discussed for Rh loading; too much Ru presence may lead to increased electron-hole pair recombination.



6.7 Diffuse reflectance spectra of Rh-doped aerogel SrTiO₃ (1.5 wt% Ru, cal. 500 °C) from different doping amounts (a) 1 mole% (b) 1.25 mole% (c) 1.5 mole% (d) 1.75 mole%.



6.8 TEM images of Rh-doped aerogel synthesis SrTiO_3 (1.5 wt% Ru, cal. 500 °C) upon the different Rh doping amount (a) 1 mole% (b) 1.25 mole% (c) 1.5 mole% (d) 1.75 mole%.

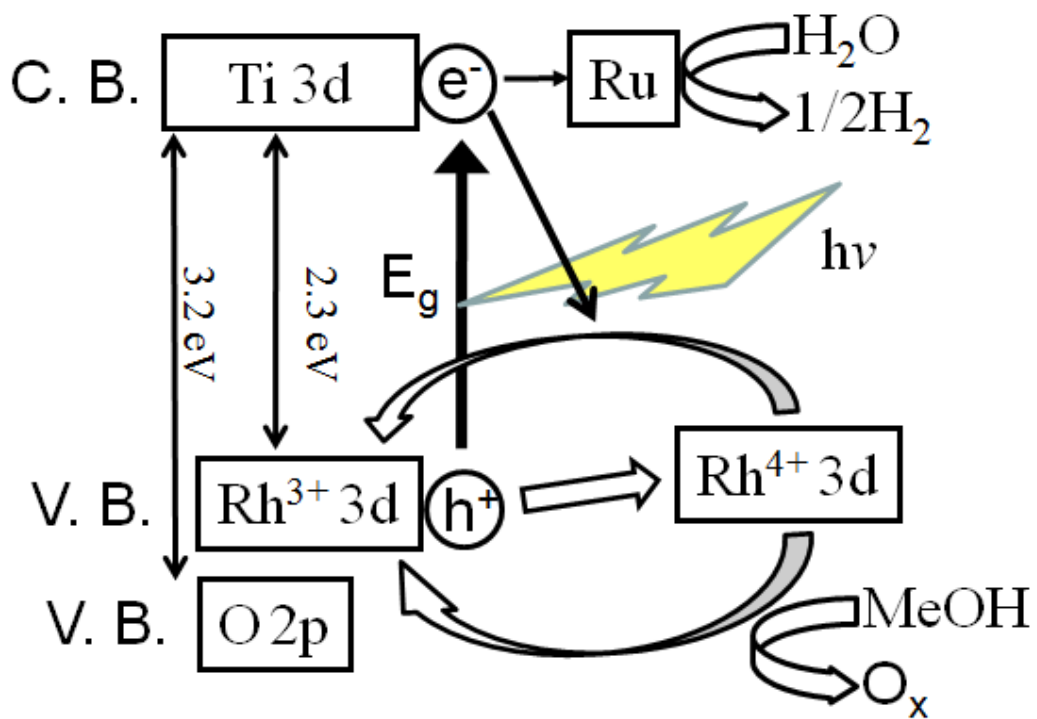


6.9 Dependence of H₂ evolution activity of aerogel SrTiO₃: Rh (1.25 mole % Rh, cal. 500 °C) upon different amounts of co-catalyst Ru in 10 vol % methanol solution (pH = 12.4, adjusted by NaOH) under visible light.

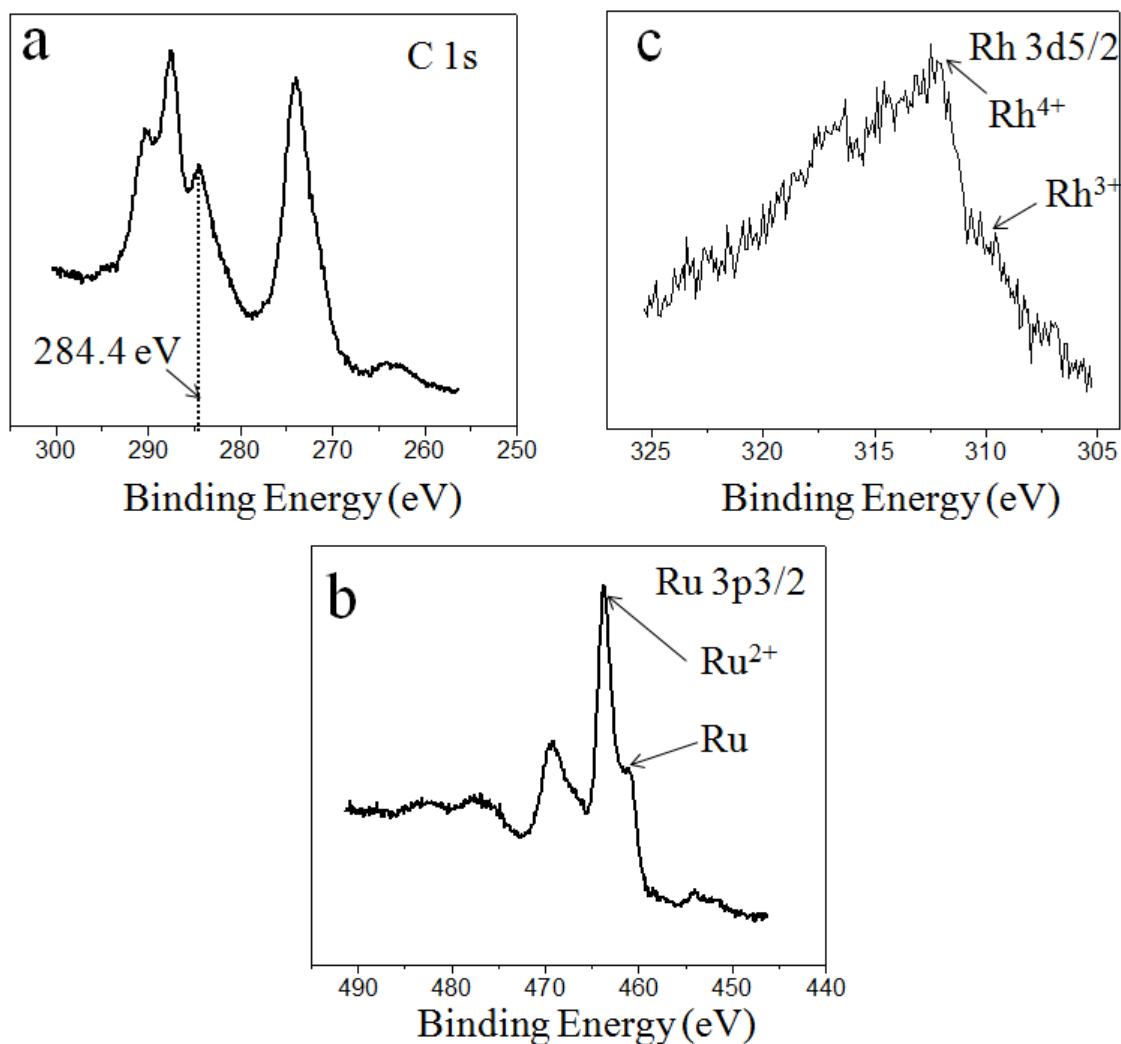
6.3.6 Mechanism

The proposed schematic mechanism for the photocatalytic H₂ evolution on Ru/SrTiO₃:Rh is illustrated in figure 6.10. The visible light absorption bands in the diffuse reflectance spectrum are very likely due to Rh³⁺. In figure 6.11c, The XPS data confirmed the presence of Rh³⁺ and Rh⁴⁺. These Rh ions could be isolated or have neighbors, depending on loading, and what is needed is a balance favoring electron/hole formation and separation, rather than facilitating recombination. The Rh with higher oxidation number, such as Rh⁴⁺, can be easily reduced back to Rh³⁺ by photogenerated electrons or by oxidizing methanol. The highly

efficient H₂ evolution on the SrTiO₃:Rh photocatalyst under visible light irradiation indicates that Rh³⁺ works as an electron donor to the conduction band. It is the major electron pump for photocatalytic H₂ evolution. The electrons photogenerated in the conduction band transfer to Ru and reduce water to form H₂, while holes formed in the electron donor level oxidize methanol. The Ru may be present in oxidation states of 0 and 2+, which were observed by XPS (figure 6.11b).^{19,20} This indicates that the doped Rh³⁺ formed the visible light absorption center and the surface reaction center. Because of higher surface area, the optimum doping amount was 1.25%, which is higher than conventional solid-state synthesis samples.²¹ During these experiments there was no O₂ evolution observed, even though the potential of generated holes might be thermodynamically high enough for oxidation of water to form O₂. However, there are no reaction centers for the four-electron oxidation for O₂ evolution. On the other hand, the standard redox potentials for HCHO/CH₃OH and H₂CO₃/CH₃OH are 0.232 and 0.044 V, so methanol oxidation is easy compared to O₂ evolution from water (1.23 V) from both thermodynamic and kinetic standpoints.²¹ Moreover, it is well-known that O₂ evolution has a large overpotential (> 0.5 V).²¹ Thus, it is clear that water oxidation is harder than methanol oxidation.



6.10 Proposed schematic diagram for visible light response of Ru/SrTiO₃:Rh photocatalyst.



6.11 XPS spectra of Ru/SrTiO₃:Rh (1.25 mole % Rh, 1.5 wt% Ru, Cal. 500 °C) (a) C 1s (b) Ru 3p3/2 (c) Rh 3d5/2.

6.4 Conclusions

We have used a modified aerogel synthesis method to prepare nanostructured high surface area Ru/SrTiO₃:Rh oxide photocatalysts that are active for H₂ evolution from an aqueous methanol solution under visible light irradiation. The aerogel method also provides for thin-film fabrication and increases possible applications. The visible light response was due to the transition from the electron donor level formed by Rh³⁺ ions to the conduction band composed of

Ti 3d orbitals of SrTiO₃.⁸ The absorption band in the visible light region from 400 nm to 520 nm directly corresponded to photocatalytic hydrogen evolution activity. The optimal synthesis condition is 1.25 mole % Rh, 1.5 wt % Ru, calcination temperature at 550 °C and pH = 12.4 aqueous methanol solution. The solution for hydrogen generation has to be basic (alkaline), which is unique from most other photocatalytic water splitting materials. The calcination temperature and dopant amount of Rh are two major factors that affect H₂ evolution.

References

1. Maeda, K.; Takata, T.; Hara, M.; Saito, N.; Inoue, Y.; Kobayashi, H.; Domen, K., GaN:ZnO Solid Solution as a Photocatalyst for Visible-Light-Driven Overall Water Splitting. *Journal of the American Chemical Society* **2005**, 127, (23), 8286-8287.
2. Maeda, K.; Teramura, K.; Lu, D.; Takata, T.; Saito, N.; Inoue, Y.; Domen, K., Photocatalyst releasing hydrogen from water. *Nature* **2006**, 440, (7082), 295-295.
3. Lee, Y.; Terashima, H.; Shimodaira, Y.; Teramura, K.; Hara, M.; Kobayashi, H.; Domen, K.; Yashima, M., Zinc Germanium Oxynitride as a Photocatalyst for Overall Water Splitting under Visible Light. *The Journal of Physical Chemistry C* **2007**, 111, (2), 1042-1048.
4. Fujihara, K.; Ohno, T.; Matsumura, M., Splitting of water by electrochemical combination of two photocatalytic reactions on TiO₂ particles. *Journal of the Chemical Society, Faraday Transactions* **1998**, 94, (24), 3705-3709.
5. Sayama, K.; Mukasa, K.; Abe, R.; Abe, Y.; Arakawa, H., Stoichiometric water splitting into H and O using a mixture of two different photocatalysts and an IO³⁻/I shuttle redox mediator under visible light irradiation. *Chemical Communications* **2001**, (23), 2416-2417.
6. Abe, R.; Takata, T.; Sugihara, H.; Domen, K., Photocatalytic overall water splitting under visible light by TaON and WO₃ with an IO³⁻/I shuttle redox mediator. *Chemical Communications* **2005**, (30), 3829-3831.
7. Kato, H.; Hori, M.; Kato, R.; Shimodaira, Y.; Kudo, A., Construction of Z-scheme type heterogeneous photocatalysis systems for water splitting into H₂ and O₂ under visible light irradiation. *Chemistry Letters* **2004**, 33, (10), 1348-1349.
8. Kato, R.; Ishii, T.; Kato, H.; Kudo, A., Photocatalytic Activities of Noble Metal Ion Doped SrTiO₃ under Visible Light Irradiation. In *The Journal of Physical Chemistry B*, American Chemical Society: 2004; Vol. 108, pp 8992-8995.
9. Kudo, A.; Omori, K.; Kato, H., A Novel Aqueous Process for Preparation of Crystal Form-Controlled and Highly Crystalline BiVO₄ Powder from Layered Vanadates at Room Temperature and Its Photocatalytic and Photophysical Properties. *Journal of the American Chemical Society* **1999**, 121, (49), 11459-11467.
10. Shimodaira, Y.; Kato, H.; Kobayashi, H.; Kudo, A., Photophysical Properties and Photocatalytic Activities of Bismuth Molybdates under Visible Light Irradiation. *The Journal of Physical Chemistry B* **2006**, 110, (36), 17790-17797.

11. Darwent, J. R.; Mills, A., Photo-oxidation of water sensitized by WO₃ powder. *Journal of the Chemical Society, Faraday Transactions 2: Molecular and Chemical Physics* **1982**, 78, (2), 359-367.
12. Kato, H.; Sasaki, Y.; Iwase, A.; Kudo, A., Role of Iron Ion Electron Mediator on Photocatalytic Overall Water Splitting under Visible Light Irradiation Using Z-Scheme Systems. *Bulletin of the Chemical Society of Japan* **2007**, 80, (12), 2457-2464.
13. Sasaki, Y.; Iwase, A.; Kato, H.; Kudo, A., The effect of co-catalyst for Z-scheme photocatalysis systems with an Fe³⁺/Fe²⁺ electron mediator on overall water splitting under visible light irradiation. *Journal of Catalysis* **2008**, 259, (1), 133-137.
14. Demydov, D.; Klabunde, K. J., Characterization of mixed metal oxides (SrTiO₃ and BaTiO₃) synthesized by a modified aerogel procedure. *Journal of Non-Crystalline Solids* **2004**, 350, 165-172.
15. Utamapanya, S.; Klabunde, K. J.; Schlup, J. R., Nanoscale metal oxide particles/clusters as chemical reagents. Synthesis and properties of ultrahigh surface area magnesium hydroxide and magnesium oxide. *Chemistry of Materials* **1991**, 3, (1), 175-181.
16. Diao, Y.; Walawender, W. P.; Sorensen, C. M.; Klabunde, K. J.; Ricker, T., Hydrolysis of Magnesium Methoxide. Effects of Toluene on Gel Structure and Gel Chemistry. *Chemistry of Materials* **2001**, 14, (1), 362-368.
17. Osterloh, F. E., Inorganic Materials as Catalysts for Photochemical Splitting of Water. *Chemistry of Materials* **2008**, 20, (1), 35-54.
18. Rabuffetti, F. A.; Stair, P. C.; Poepelmeier, K. R., Synthesis-Dependent Surface Acidity and Structure of SrTiO₃ Nanoparticles. *The Journal of Physical Chemistry C* **2010**, 114, (25), 11056-11067.
19. Salyn, Y. V.; Nefedov, V. I.; Maiorova, A. G.; Kuznetsova, G. N., X-RAY ELECTRON STUDY OF PLATINUM(III) COMPOUNDS WITH ACETAMIDE. *Zhurnal Neorganicheskoi Khimii* **1978**, 23, (3), 829-831.
20. McEvoy, A. J.; Gissler, W., ESCA SPECTRA AND ELECTRONIC-PROPERTIES OF SOME RUTHENIUM COMPOUNDS. *Physica Status Solidi a-Applied Research* **1982**, 69, (1), K91-K96.
21. Sasaki, Y.; Nemoto, H.; Saito, K.; Kudo, A., Solar Water Splitting Using Powdered Photocatalysts Driven by Z-Schematic Interparticle Electron Transfer without an Electron Mediator. *The Journal of Physical Chemistry C* **2009**, 113, (40), 17536-17542.